

# UC San Diego

## UC San Diego Electronic Theses and Dissertations

### Title

An improved event-driven model of presynaptic dynamics for large-scale simulations of biophysically realistic and diverse synapses

### Permalink

<https://escholarship.org/uc/item/1qj029m6>

### Author

Garcia, Jonathan

### Publication Date

2017

Peer reviewed|Thesis/dissertation

UNIVERSITY OF CALIFORNIA, SAN DIEGO

An improved event-driven model of presynaptic dynamics for large-scale  
simulations of biophysically realistic and diverse synapses

A dissertation submitted in partial satisfaction  
of the requirements for the degree Doctor of Philosophy

in

Neurosciences, with a specialization in Computational Neurosciences

by

Jonathan William Garcia

Committee in charge:

Professor Terrence Sejnowski, Chair  
Professor Gert Cauwenberghs  
Professor Jeffry Isaacson  
Professor Maryann Martone  
Professor Charles Stevens

2017

Copyright

Jonathan William Garcia, 2017

All rights reserved.

The Dissertation of Jonathan William Garcia is approved, and it is acceptable in quality and form for publication on microfilm and electronically:

---

---

---

---

---

Chair

University of California, San Diego

2017

## DEDICATION

For her longsuffering devotion, prayers, encouragement, and support, for the love and joy she has brought to my life these last couple of years as I finished my doctorate, and for the life we look forward to living out together from this point forward, I dedicate this dissertation to my extraordinary wife, Ellen.

## TABLE OF CONTENTS

SIGNATURE PAGE .....	iii
DEDICATION .....	iv
TABLE OF CONTENTS .....	v
LIST OF FIGURES .....	vii
LIST OF TABLES .....	x
ACKNOWLEDGEMENTS .....	xi
VITA .....	xii
ABSTRACT OF THE DISSERTATION .....	xiii
1 Introduction .....	1
2 Characterizing the Dynamics of Position- and Stimulus-Dependent Synaptic Release Rate at High Temporal Resolution from Molecular Simulations .....	6
2.1 Methods .....	7
2.1.1 MCell as Ground Truth .....	7
2.1.2 Deterministic Simulations of State Probabilities .....	17
2.1.3 Stimulus Protocols for Exploring Facilitation .....	19
2.1.4 Algorithms for Fitting Parameters and Metaparameters .....	20
2.2 Results .....	21
2.2.1 MCell and Deterministic Simulations .....	21
2.2.2 Baseline and Impulse-Response Release Rate Functions .....	29
2.2.3 Release Rate Functions from Ca <sup>2+</sup> Dynamics .....	34
2.2.4 Distance-Dependence of Ca <sup>2+</sup> Sensor .....	43
2.2.5 Facilitation in Release Probability .....	51
3 A Phenomenologically Accurate and Computationally Efficient Event-Driven Model of Presynaptic Dynamics .....	68
3.1 Methods .....	69

3.1.1	Model Overview .....	69
3.1.2	Computing Next Event Times .....	70
3.1.3	Model Dependencies.....	77
3.2	Results .....	83
3.2.1	Validation .....	83
3.2.2	Runtime Complexity .....	102
4	Discussion.....	105
4.1	Model Extensibility .....	105
4.2	Limiting Assumptions of MCell as Ground Truth.....	109
4.3	Room for Improvement in Scalability.....	112
4.4	Comparisons to Other Models.....	115
4.4.1	Tsodyks and Markram (1997) .....	117
4.4.2	Maass and Zador (1999) .....	119
4.4.3	Kandaswamy et al. (2010).....	121
4.5	Summary and Further Applications .....	123
	References.....	126

## LIST OF FIGURES

Figure 2.1: Voltage-Dependent $\text{Ca}^{2+}$ Channel Kinetics. ....	9
Figure 2.2: State Diagrams for PMCA and Calbindin. ....	10
Figure 2.3: SNARE Complex Structure and Dynamics. ....	14
Figure 2.4: Synaptotagmin-Mediated Neurotransmitter Release State Diagram.....	16
Figure 2.5: Action-Potential-Evoked $\text{Ca}^{2+}$ Current. ....	23
Figure 2.6: Effect of Calbindin Buffer on Spike-Evoked $\text{Ca}^{2+}$ Profile and Release Rates.....	24
Figure 2.7: Spatial Modeling Important for Capturing Fine-Grain Features of $\text{Ca}^{2+}$ Transients. ....	26
Figure 2.8: Synchronous and Asynchronous Release in MCell. ....	28
Figure 2.9: Synchronous and Asynchronous Release Rates in Response to $\text{Ca}^{2+}$ Impulse at Different Resting Concentrations. ....	31
Figure 2.10: Spontaneous Rates of Vesicle Fusion Increase with $[\text{Ca}^{2+}]_{i0}$ .....	32
Figure 2.11: Slow Un-buffering of Latent $\text{Ca}^{2+}$ Leads to Longer Time Constants for Synchronous and Asynchronous Release. ....	33
Figure 2.12: Multi-Exponential Shape of $\text{Ca}^{2+}$ -Driven Vesicle Release Rate. ....	35
Figure 2.13: Convolutional Filter Applied to a Component of a Release Rate Function. ....	39
Figure 2.14: Fitted Release Rate Histogram Profile Parameters. ....	42
Figure 2.15: Peak $[\text{Ca}^{2+}]_i$ Drops Off Exponentially with Distance from VDCC Cluster. ....	44
Figure 2.16: Spatial Modeling Important for Capturing Fine-Grain Features of $\text{Ca}^{2+}$ Transients. ....	46
Figure 2.17: Synchronous and Asynchronous Release Rates Decrease with Distance from the $\text{Ca}^{2+}$ Source.....	48
Figure 2.18: Parametric Fits to Release Histogram Profiles at Increasing Distance from the $\text{Ca}^{2+}$ Source.....	50

Figure 2.19: Change in the Balance of Binding Kinetics and Internal State Distribution of $\text{Ca}^{2+}$ Sensor with Spike History.....	52
Figure 2.20: Empirical Facilitation in Release Probability is a Nonlinear Function of Spike History and $\text{Ca}^{2+}$ Buildup.....	55
Figure 2.21: Empirical Facilitation in Synchronous and Asynchronous Release Rates. ....	57
Figure 2.22: Saturation of Facilitation Parameters. ....	61
Figure 2.23: Release Rate Parameters and Facilitation Metaparameters Fitted to Empirical Histogram Profiles. ....	65
Figure 3.1: Vesicle State-Transition Diagram.....	69
Figure 3.2: Histogram of Spontaneous and Spike-Evoked Processes. ....	74
Figure 3.3: Spike-Evoked Processes with Ex-Gaussian Delay Follow Analytical Predictions.....	76
Figure 3.4: Class Dependencies of the Event-Driven Model.....	78
Figure 3.5: Structure and Output of the Simple MCell-Analog Model. ....	86
Figure 3.6: Comparisons of Event-Driven Release to MCell Model, with and without Post-Release Refractory Period.....	88
Figure 3.7: Release-Dependent Depression Limits the Time Window for Synaptic Transmission under Sustained Stimulation. ....	92
Figure 3.8: Release-Independent Depression with Frequency-Dependent Recovery Equivalent to Competitive Model of Synaptic Inactivation and Reactivation. ....	95
Figure 3.9: Effect of Competitive RID-FDR Depression Model on Synaptic Dynamics. ....	97
Figure 3.10: $\text{Ca}^{2+}$ -Dependent Vesicle Recruitment Enables Sustained Facilitation to Overcome Depletion.....	99
Figure 3.11: Linear Runtime Complexity of Event-Driven Synaptic Model. ....	103
Figure 4.1: Example of Complex Synapse Made Possible with Event-Driven Framework.....	108
Figure 4.2: Comparison of My Model with That of Tsodyks and Markram (1997). ...	118

Figure 4.3: Comparison of My Model with That of Maass and Zador (1999)..... 120  
Figure 4.4: Comparison of My Model with That of Kandaswamy et al. (2010). ..... 122

## LIST OF TABLES

Table 2.1: Parameter Values for VDCC, PMCA, and Calbindin.....	11
Table 2.2: SNARE Release State Transition Parameters.....	16
Table 2.3: Spike-Evoked Release Rate Parameters.....	42
Table 2.4: Metaparameters for Facilitation of Release Fidelity.....	67

## ACKNOWLEDGEMENTS

I would like to acknowledge Professor Terrence Sejnowski for his support as chair of my committee. Working in his lab has been a pleasure, and the guidance he provided me was invaluable for allowing me to finish my dissertation in time for my wedding in May 2017.

I would also like to acknowledge Thomas Bartol for his many contributions in collaborating with me on this project. He helped me set up and run all the many MCell simulations off of which I based much of my work. For his technical assistance and for his friendship and encouragement, I have greatly enjoyed working with him.

Finally, I would like to acknowledge Donald Spencer, with whom I collaborated on many different projects since joining the lab. I deeply appreciate his friendship as well as all the ideas that came out of conversations I had with him.

Chapter 2, in part, is currently being prepared for submission for publication of the material. Bartol, Thomas M.; Sejnowski, Terrence J. The dissertation author was the primary investigator and author of this material.

Chapter 3, in part, is currently being prepared for submission for publication of the material. Bartol, Thomas M.; Sejnowski, Terrence J. The dissertation author was the primary investigator and author of this material.

## VITA

- 2008-2011    Calculus Peer Assistant, Department of Mathematics, Texas A&M University
- 2011         Bachelor of Science, Biomedical Engineering, Texas A&M University
- 2013-2017    Research Assistant, University of California, San Diego
- 2014         Teaching Assistant, Department of Neurosciences, University of California, San Diego
- 2017         Doctor of Philosophy, Neurosciences, with a specialization in Computational Neurosciences, University of California, San Diego

## FIELDS OF STUDY

Major Field: Biomedical Engineering

    Studies in Mathematics

    Studies in Computer Science

## ABSTRACT OF THE DISSERTATION

An improved event-driven model of presynaptic dynamics for large-scale simulations of biophysically realistic and diverse synapses

by

Jonathan William Garcia

Doctor of Philosophy in

Neurosciences, with a specialization in Computational Neurosciences

University of California, San Diego, 2017

Professor Terrence Sejnowski, Chair

Chemical synapses exhibit a diverse array of internal mechanisms that affect the dynamics of transmission efficacy. Many of these processes, such as release of neurotransmitter and vesicle recycling, depend strongly on activity-dependent influx and accumulation of  $\text{Ca}^{2+}$ . To model how each of these processes may affect the processing of information in neural circuits, and how their dysfunction may lead to disease states, requires

a computationally efficient modelling framework, capable of generating accurate phenomenology without incurring a heavy computational cost per synapse. In this dissertation, I derive physically grounded mathematical models of the instantaneous rate of  $\text{Ca}^{2+}$ -triggered neurotransmitter release. The  $\text{Ca}^{2+}$  traces that drive these dynamics come from simulations in MCell of spike-evoked  $\text{Ca}^{2+}$  influx and buffered diffusion through the presynaptic space, an approach that overcomes observational limitations of physiological experiments. With these  $\text{Ca}^{2+}$  traces, I drive a validated kinetic model of the SNARE complex, which mediates spike-triggered vesicle fusion for both synchronous and asynchronous release. The profiles of the resulting release rate histograms inform the parameters of the phenomenological release models, including the time scales and the facilitation of release probability. Based on these results, I construct an event-driven model of presynaptic dynamics, treating all  $\text{Ca}^{2+}$ -sensitive processes, not just vesicle release, as Poisson processes with decaying rate parameters that may undergo activity-dependent facilitation. This approach provides a unified framework for modelling both spontaneous and spike-evoked presynaptic vesicle dynamics, for an arbitrary number of processes that define interaction between an arbitrary number of vesicle pools and recycling pathways. I validate the model against MCell and demonstrate a runtime complexity that bridges the gap between full molecular simulations and abstract synaptic models. Furthermore, I verify that  $\text{Ca}^{2+}$ -dependent recycling mechanisms are essential for maintaining transmission fidelity during high-frequency stimuli. Finally, the versatility of the framework enables one both to model diverse types of synapses and to perform test and control modelling experiments by including different sets of features and controlling their rates and responsiveness. I present this model as a highly extensible tool for future investigations into the functional impact of different synaptic mechanisms on information processing and dysfunction in model networks.

# 1 Introduction

Chemical synapses constitute the primary means of direct communication between neurons throughout the nervous system, and throughout the brain in particular (Abbott & Regehr, 2004; Alabi & Tsien, 2012; Gross & von Gersdorff, 2016). When the action potential (AP) of the presynaptic neuron reaches the axon terminal, it triggers a sudden influx of  $\text{Ca}^{2+}$  that leads probabilistically to the fusion of synaptic vesicles with the plasma membrane and the release of neurotransmitter across the synaptic cleft (Branco & Staras, 2009; Edwards, 2007; Körber & Kuner, 2016). The neurotransmitter then binds to receptors on the membrane of the next neuron that initiate a post-synaptic current (PSC), which propagates the signal further (Dobrunz, Huang, & Stevens, 1997; K M Franks, Stevens, & Sejnowski, 2003; J. Y. Sun & Wu, 2001). How neurons integrate their inputs and generate signals in the context of larger neural circuits largely determines the sorts of computations that the network can perform (Scott, Cowan, & Stricker, 2012; M. Tsodyks, Pawelzik, & Markram, 1998).

Very often, discussion of the activity in a network tends to focus on the APs (spikes) and subthreshold fluctuations in membrane potential (Buzsáki, Anastassiou, & Koch, 2012; Hahnloser, Kozhevnikov, & Fee, 2002; Morrison, Straube, Plesser, & Diesmann, 2007). These features are readily measured, either directly or indirectly, through patch-clamp recordings, microelectrodes, local field potentials, fluorescent  $\text{Ca}^{2+}$  reporters, and other methods (Kitamura, Judkewitz, Kano, Denk, & Häusser, 2008; Knöpfel, 2012; Scanziani & Häusser, 2009; Shew, Bellay, & Plenz, 2010; Spira & Hai, 2013), which can be recorded in vivo, even in awake, behaving animals. Intracortical brain-computer interfaces (BCIs) that record live neural activity from the motor cortex of paralytics and amputees have even been used in recent years to train machine learning

models to control prosthetic limbs (Collinger et al., 2013; Hochberg et al., 2006; Klaes et al., 2014). The utility of these measurements, however, depends on the relevance of the spike code to neural information processing. Biological neural networks need to represent information in a way that confers behavioral utility, quite unlike computers, which store and process all the information they receive, regardless of its usefulness. Since so much of the information in the environment is irrelevant to survival, synapses may not be optimized to transmit all information faithfully, but rather selectively.

Significantly, neurons do not directly see the spiking activity of their neighbors at chemical synapses, but only detect presynaptic activation upon the release of neurotransmitter, which is a stochastic process (Branco & Staras, 2009). Synapses form the basis for learning and information processing, and short-term plasticity (STP) defines a transformation from a spiking code to a neurotransmitter release code. All spiking activity is filtered through the dynamics of probabilistic synaptic release before the rest of the network can see it. This implies that one must first have an accurate model of release dynamics in order to understand the true nature of information processing of brain circuits. Such a model could, for instance, provide a crucial preprocessing step of motor cortex for training BCI-based prosthetics, or it could enable more accurate computation of the information capacity of sensory cortex by studying the “language” that neurons actually receive rather than simply the output that they generate (Rosenbaum, Rubin, & Doiron, 2012; Rotman, Deng, & Klyachko, 2011; Salmasi, Stemmler, Glasauer, & Loebel, 2017; Scott et al., 2012; Veletić, Floor, Chahibi, & Balasingham, 2016).

Synaptic dysfunction has been implicated in numerous psychological disorders, including schizophrenia (Crabtree & Gogos, 2014; Vawter et al., 2002), bipolar disorder (Vawter et al., 2002), ASD (Giovedi, Corradi, Fassio, & Benfenati, 2014), and fragile X

syndrome (Deng, Soika, & Klyachko, 2011). To ascertain exactly what role synapses play and what specific mechanisms might be causing or exacerbating these diseases, controlled experiments would need to be performed on the brain circuits of interest, testing which changes to synaptic function might push the network into a pathological state. Doing this in humans would pose significant problems, both technical and ethical. However, with a computational model that exhibits sufficient realism and scalability, such experiments become possible in large simulated networks, which could provide important insight into what sorts of targeted therapies to explore for treating or curing these diseases.

Current synaptic models either lack the necessary complexity and flexibility to represent realistic release dynamics accurately or they have so high a computational cost that it severely limits scalability for simulating sizable networks. Simple multiplicative weights, which represent synaptic strength in many models (Chapeau-Blondeau & Chambet, 1995), have no short-term dynamics and cannot act as temporal filters of presynaptic activity. More complex models include features such as stochastic release, short-term facilitation, and short-term depression (Kandaswamy, Deng, Stevens, & Klyachko, 2010; Maass & Zador, 1999; M. V. Tsodyks & Markram, 1997), but their phenomenology is often too abstract for studying how internal synaptic mechanisms affect the network level (see Discussion 4.4 for more). On the other hand, highly detailed models like MCell, which tracks the kinetics and interactions of thousands of molecular and ionic species in a three-dimensional model of presynaptic space (R. A. Kerr et al., 2008; Nadkarni, Bartol, Sejnowski, & Levine, 2010; Stiles & Bartol, 2001; Stiles, van Helden, Bartol, Salpeter, & Salpeter, 1996), can achieve a high degree of realism and provide useful insights into how biomolecular systems function in the absence of scientific interventions (Bartol et al., 2015). Such models, when properly constrained by

experimental data, automatically reproduce observed features such as the facilitation and depression of probabilistic release and the release that occurs asynchronously relative to spike times (Nadkarni et al., 2010). However, it quickly becomes too computationally expensive, in terms of both memory requirements and number of processing steps, to scale up to the many synapses that exist even in relatively simple neural circuits. As mentioned previously, several psychological disorders may be due to dysfunction in mechanisms of short-term plasticity (Crabtree & Gogos, 2014; Deng et al., 2011; Giovedi et al., 2014; Vawter et al., 2002), but modeling is necessary to understand the nature of the effect. Efficient, simple models are unable to capture realistic dynamics and cannot be easily applied to study disease states in networks. On the other end, realistic molecular models like MCell may require hours to simulate a few hundred milliseconds of a single synapse and are thus unsuitable for network simulations.

The goal of this dissertation, therefore, is to develop a presynaptic model that captures realistic phenomenology while maintaining computational scalability. To that end, I first uncover a mathematical model that describes the phenomenology of presynaptic dynamics, using MCell as ground truth. Second, I build an asynchronous, event-driven model that captures this same phenomenology at a small fraction of the computational cost. The model fills a gap in the spectrum between highly efficient but unrealistic synaptic models on the one hand and highly realistic but non-scalable models on the other. Additionally, the structure of the model presented here permits a high degree of flexibility, allowing one to add or remove synaptic components and processes with ease. This can be useful both for representing numerous synaptic types with a single framework and for uncovering the synaptic processes important in information processing and in disease states through controlled manipulation of synaptic features. I produced the model using object-oriented programming in MATLAB (see

[github.com/soiens24/Presynaptic\\_Framework](https://github.com/soiens24/Presynaptic_Framework) for source code), but it can easily be adapted to any programming language. The various classes comprise a software package that gives computational neuroscientists a tool to model virtually any kind of synapse with an almost arbitrary degree of abstraction.

## 2 Characterizing the Dynamics of Position- and Stimulus-Dependent Synaptic Release Rate at High Temporal Resolution from Molecular Simulations

Constructing a phenomenologically realistic model requires the precise characterization of the timing and probability of neurotransmitter release. Difficulties arise in that functional forms of instantaneous release rate can be difficult to extract from noisy data without running many thousands of trials, and in biophysical synapses, facilitation of per-vesicle release probability is confounded by depletion. To overcome this, we obtained traces of free  $\text{Ca}^{2+}$  concentration in response to various action potential stimulus trains from an MCell model of a hippocampal mossy fiber axon.  $\text{Ca}^{2+}$  sensors were placed at varying distance from a voltage-dependent calcium channel (VDCC) cluster, and  $\text{Ca}^{2+}$  was buffered by calbindin. Then, using the calcium traces to drive deterministic state vector models of synaptotagmin 1 and 7 (Syt-1/7), which respectively mediate synchronous and asynchronous release in excitatory hippocampal synapses, I obtained high-resolution profiles of instantaneous release rate, to which I applied functional fits. Synchronous vesicle release occurred predominantly within half a micron of the source of spike-evoked  $\text{Ca}^{2+}$  influx, while asynchronous release occurred more consistently at all distances. Both fast and slow mechanisms exhibited multi-exponential release rate curves, whose magnitudes decayed exponentially with distance from the  $\text{Ca}^{2+}$  source. Profile parameters facilitate on different time scales according to a single, general facilitation function. These functional descriptions lay the groundwork for efficient modelling of vesicular release dynamics.

## 2.1 Methods

### 2.1.1 MCell as Ground Truth

Basing the new model on MCell has distinct advantages over biological experiments in terms of both flexibility and precision when it comes to model validation. As an example, estimates of  $[Ca^{2+}]_i$  in neurons obtained from fluorescent reporters in physiological experiments may provide accurate estimates of slow (tens of milliseconds)  $Ca^{2+}$  transients (Grewe & Helmchen, 2014; Grienberger & Konnerth, 2012), but the buffering kinetics of the calcium reporters can act as a low-pass filter, obscuring the faster (0-5 milliseconds) components of  $Ca^{2+}$  dynamics (Bartol et al., 2015). Molecular simulations like MCell, on the other hand, can capture these fast transients, since they track every particle, which may be crucial for correctly modeling fast,  $Ca^{2+}$ -dependent synaptic processes like synchronous vesicular release of neurotransmitter (Kaesler & Regehr, 2014) (see Figure 6 from (Bartol et al., 2015)).

Furthermore, neurotransmitter release may occur asynchronously with respect to the arrival time of action potentials, following some time-dependent distribution (Kaesler & Regehr, 2014). Experimental methods for determining release rate would offer far less control of presynaptic conditions over the number of trials that would be required to tease out the same resolution of detail as is possible with controlled simulations. Therefore, we choose to constrain ourselves to validating the current model of presynaptic release to MCell, which has itself been validated already against hippocampal Schaffer collateral synapses (Nadkarni et al., 2010).

#### 2.1.1.1 Spike-Evoked $Ca^{2+}$ Kinetics

The MCell model used as a basis for the current model's design and validation comes from Nadkarni et al. (2010). It includes mechanisms for voltage-sensitive  $Ca^{2+}$  influx and

for  $\text{Ca}^{2+}$  buffering in the presynaptic space, with pumps and channels in the membranes to maintain a steady-state average free  $\text{Ca}^{2+}$  concentration of 100 nM (Simons, 1988).

When an action potential arrives at the presynaptic membrane, voltage-dependent  $\text{Ca}^{2+}$  channels (VDCCs) open stochastically, traversing through four unopened states via voltage-dependent state transition rates (Bischofberger, Geiger, & Jonas, 2002) (see Figure 2.1A), producing a huge  $\text{Ca}^{2+}$  influx due to the sharp electrochemical gradient (Figure 2.1C) (Simons, 1988). The VDCCs very quickly shut off after the membrane potential returns to baseline (see Figure 2.5B in Results 2.2.1), and the newly introduced  $\text{Ca}^{2+}$  ions diffuse randomly in the presynaptic space. Vesicle fusion occurs when a sufficient number of  $\text{Ca}^{2+}$  ions have diffused over and bound to the release machinery associated with the SNARE complex of a docked vesicle (Nadkarni et al., 2010; J. Sun et al., 2007; Südhof, 2013a) (see Methods 2.2.1.3). A 45- $\mu\text{M}$  buffer of calbindin (CB; Figure 2.2B) controls the magnitude and duration of the free  $\text{Ca}^{2+}$  (Nägerl, Novo, Mody, & Vergara, 2000), and plasma membrane  $\text{Ca}^{2+}$ -ATPase (PMCA; Figure 2.2A) pumps actively remove  $\text{Ca}^{2+}$  ions over a time course of seconds (Sneyd et al., 2003) to the baseline  $[\text{Ca}^{2+}]_i$  of 100 nM (Nadkarni et al., 2010; Simons, 1988). Parameter values are given in Table 2.1.

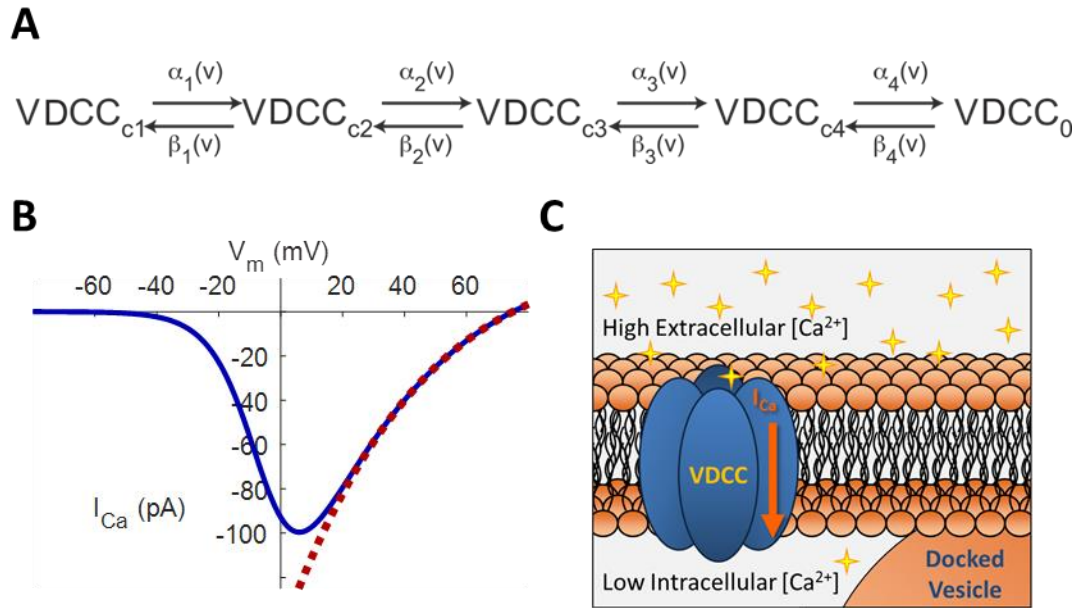


**Figure 2.1: Voltage-Dependent  $\text{Ca}^{2+}$  Channel Kinetics.**

VDCC model adapted from Bischofberger et al.(2002). (A) State transition diagram for VDCCs, reused with permission from Nadkarni et al. (2010); transition rates  $\alpha_{ij}$  and  $\beta_{ji}$  depend on membrane potential  $v$ . (B) Tail current of  $\text{Ca}^{2+}$  ions through VDCCs as a function of membrane potential. (C) VDCCs mediate  $\text{Ca}^{2+}$  influx down a sharp electrochemical gradient from a relatively high extracellular concentration to a very low intracellular concentration.

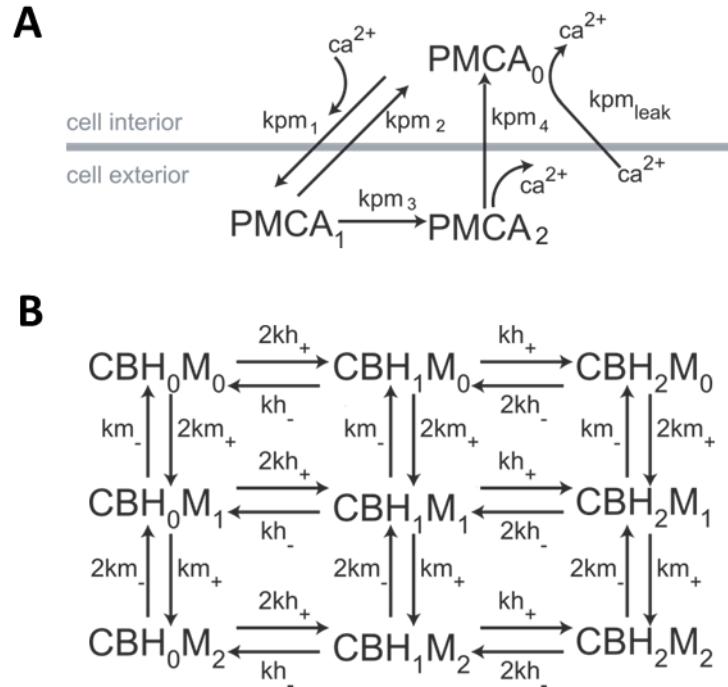


**Figure 2.2: State Diagrams for PMCA and Calbindin.**

Reproduced with permission from Nadkarni et al. (2010). (A) PMCA pump state diagram with  $\text{Ca}^{2+}$  interactions depicted on the relative side of the membrane.  $\text{Ca}^{2+}$  leakage occurs only in state  $\text{PMCA}_0$ . Association rate  $k_{pm_1}$  is proportional to  $[\text{Ca}^{2+}]_i$ . (B) State transitions for calbindin (CB) at high-affinity (H) and medium-affinity (M)  $\text{Ca}^{2+}$ -binding sites. On rates ( $k_{h_+}$  and  $k_{m_+}$ ) are proportional to  $[\text{Ca}^{2+}]_i$ .

**Table 2.1: Parameter Values for VDCC, PMCA, and Calbindin.**

Table adapted from (Nadkarni et al., 2010). VDCC rates follow  $\alpha_i(v) = \alpha_{i0} \exp(v/v_i)$  and  $\beta_i(v) = \beta_{i0} \exp(-v/v_i)$ . VDCC parameters values adapted from (Bischofberger et al., 2002). PMCA parameter values adapted from (Sneyd et al., 2003). Calbindin parameter values adapted from (Nägerl et al., 2000).

Parameter	Value
<b>VDCC - (Bischofberger et al., 2002)</b>	
$\alpha_{10}, \alpha_{20}, \alpha_{30}, \alpha_{40}$	4.04, 6.70, 4.39, 17.33 ms <sup>-1</sup>
$\beta_{10}, \beta_{20}, \beta_{30}, \beta_{40}$	2.88, 6.30, 8.16, 1.84 ms <sup>-1</sup>
$v_1, v_2, v_3, v_4$	49.14, 42.08, 55.31, 26.55 mV
<b>PMCA - (Sneyd et al., 2003)</b>	
$kpm_1$	$1.5 \times 10^8 \text{ M}^{-1}\text{s}^{-1}$
$kpm_2$	$20 \text{ s}^{-1}$
$kpm_3$	$100 \text{ s}^{-1}$
$kpm_4$	$1.0 \times 10^5 \text{ s}^{-1}$
$kpm_{leak}$	$12.264 \text{ s}^{-1}$
<b>Calbindin-D28k - (Nägerl et al., 2000)</b>	
$kh_+$	$5.5 \times 10^6 \text{ M}^{-1}\text{s}^{-1}$
$kh_-$	$2.6 \text{ s}^{-1}$
$km_+$	$4.35 \times 10^7 \text{ M}^{-1}\text{s}^{-1}$
$km_-$	$35.8 \text{ s}^{-1}$

### 2.1.1.2 Estimating $[Ca^{2+}]_i$ from Collision Events

Because of the quantized nature and low concentration of  $Ca^{2+}$  ions in the presynaptic space, calculating the instantaneous local calcium concentration just around the SNARE complex of a single docked vesicle is nontrivial in MCell. Instead, we use effector tiles, small virtual surfaces in the presynaptic space of the MCell environment, to estimate local concentration from the frequency of calcium ions passing through them. This section provides a derivation of average  $[Ca^{2+}]_i$  from the number of “hits”,  $N_H$ , of calcium ions through the effector tile surface.

For a particle diffusing by Brownian motion in  $d$  dimensions, the probability density function  $\rho$  of the particle’s displacement  $r$  from its initial position after a time  $\Delta t$  is equal to

$$\rho(r, \Delta t) = \frac{1}{\pi^{d/2} \lambda^d} e^{-r^2/\lambda^2}, \quad (2.1)$$

where  $\lambda$  is a diffusion length parameter that depends on the diffusion constant and time step. Since we are dealing with calcium, we use

$$\lambda_{Ca} = \sqrt{4D_{Ca}\Delta t}, \quad (2.2)$$

where  $D_{Ca} = 220 \mu m^2/sec$  is the calcium diffusion constant (Nadkarni et al., 2010). More directly useful, though, is the average step length along any given axis, in particular, along the component perpendicular to the calcium-detecting surface:

$$\bar{l}_\perp = \frac{\lambda_{Ca}}{\sqrt{\pi}} = \sqrt{\frac{4D_{Ca}\Delta t}{\pi}}. \quad (2.3)$$

Thinking about the effective volume near the effector tile, the expected number of hits of particles through the surface from either side during the interval  $\Delta t$  becomes

$$N_H = N_A \bar{l}_\perp A_{ET} [Ca^{2+}]_i, \quad (2.4)$$

where  $N_A$  is Avogadro's number and  $A_{ET}$  is the area of the effector tile. Solving for concentration,

$$[Ca^{2+}]_i = \frac{N_H}{N_A \bar{l}_\perp A_{ET}}. \quad (2.5)$$

Now, the average concentration from the start of the simulation until time  $t$  becomes

$$c(t) = \frac{N_H(t)}{N_A \bar{l}_\perp A_{ET}} \cdot \frac{\Delta t}{t}, \quad (2.6)$$

where  $N_H(t)$  is the running total number of hits. To find the average  $Ca^{2+}$  concentration over an arbitrary interval  $[t_i, t_j]$ :

$$\langle [Ca^{2+}]_i([t_i, t_j]) \rangle = \frac{t_j c(t_j) - t_i c(t_i)}{t_j - t_i} \quad (2.7)$$

For each spike train used as input to the simulation, we averaged the instantaneous local active zone calcium concentration over 2000 trials in time steps of 0.1 ms.

### 2.1.1.3 State Transitions of $Ca^{2+}$ -Sensitive Release Mechanism

Most directly relevant to the characterization of the phenomenological model, though, are the  $Ca^{2+}$ -dependent dynamics of vesicle fusion mediated by the SNARE complex. Soluble N-ethylmaleimide-sensitive factor attachment protein receptors (SNAREs), including the vesicle-membrane-bound synaptobrevin (v-SNARE) and the target-membrane-bound syntaxin and SNAP-25 (t-SNAREs), bind synaptic vesicles to the plasma membrane, forming energetic SNAREpin complexes where the  $\alpha$ -helices of the v-SNAREs entwine with those of the t-SNAREs (F. Li et al., 2007; Pobbati, Stein, & Fasshauer, 2006; Sutton, Fasshauer, Jahn, & Brunger, 1998). Synaptotagmin (Syt) proteins embedded in the membrane associate with the SNARE complex and act as  $Ca^{2+}$ -sensitive triggers for vesicle fusion. When a sufficient number  $Ca^{2+}$  ions binds to the  $C_2$  domains of synaptotagmin, it undergoes a conformational change that triggers the

associated SNAREpin to zipper completely, causing the vesicle to fuse with the membrane and to release its neurotransmitter through the newly opened fusion pore (Fernandez et al., 2001; F. Li et al., 2014; Ubach et al., 2001; Ubach, Zhang, Shao, Südhof, & Rizo, 1998; Zhu & Stevens, 2008) (see Figure 2.3).

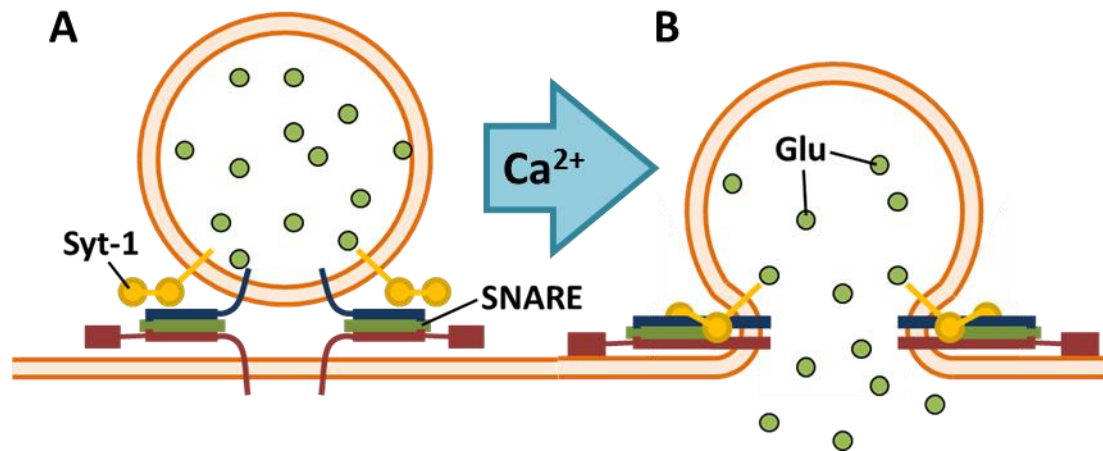


**Figure 2.3: SNARE Complex Structure and Dynamics.**

(A) SNAREpins prior to vesicle fusion. (B) Binding of  $Ca^{2+}$  to synaptotagmin (Syt-1 here, Syt-7 attaches to target membrane (Schiavo, Stenbeck, Rothman, & Söllner, 1997; Sugita et al., 2001)) triggers full zippering of SNARE complex and, in turn, vesicle fusion (Südhof, 2013a, 2013b).

Although many more proteins are involved in coordinating release kinetics at active zones (Imig et al., 2014; J. S. Lee, Ho, Neher, & Lee, 2013; Südhof, 2004; Südhof, 2013a, 2013b; Südhof & Rothman, 2009; Tang et al., 2006; Varoqueaux et al., 2002), for validation purposes we restrict the scope of this chapter to the function of synaptotagmins. The model of release used by MCell follows the dual  $Ca^{2+}$ -sensor model of Sun et al. (2007), which includes mechanisms for both fast/synchronous and slow/asynchronous release. In excitatory hippocampal synapses, these synchronous and asynchronous modes of release may correspond to the roles of synaptotagmin-1

(Syt-1) and synaptotagmin-7 (Syt-7), respectively (Bacaj et al., 2015; Bacaj et al., 2013; Kochubey, Lou, & Schneggenburger, 2011; Luo, Bacaj, & Südhof, 2015; Maximov et al., 2008; Schonm, Maximov, Lao, Südhof, & Sørensen, 2008). The model incorporates cooperative binding of  $\text{Ca}^{2+}$  to multiple sites on the sensor, requiring five  $\text{Ca}^{2+}$  ions before triggering synchronous release and two  $\text{Ca}^{2+}$  ions for asynchronous release (see Figure 2.4). Because both binding and unbinding rates for the synchronous mechanism are substantially higher than those for the asynchronous mechanism, Syt-1 produces rapid release over a very narrow window relative to spike arrival time, while Syt-7 produces slow release over a much more extended window (see Results 2.2.3). Table 2.2 contains the values used in this model for  $\text{Ca}^{2+}$ -binding and unbinding rates with each release mechanism, along with the rates of vesicle fusion from the fully bound states ( $\gamma_S$  and  $\gamma_A$ ) and the time constant for the post-release refractory period ( $\varepsilon$ ) (Dobrunz et al., 1997; Stevens & Wang, 1995), which features in the Nadkarni et al. (2010) MCell model.

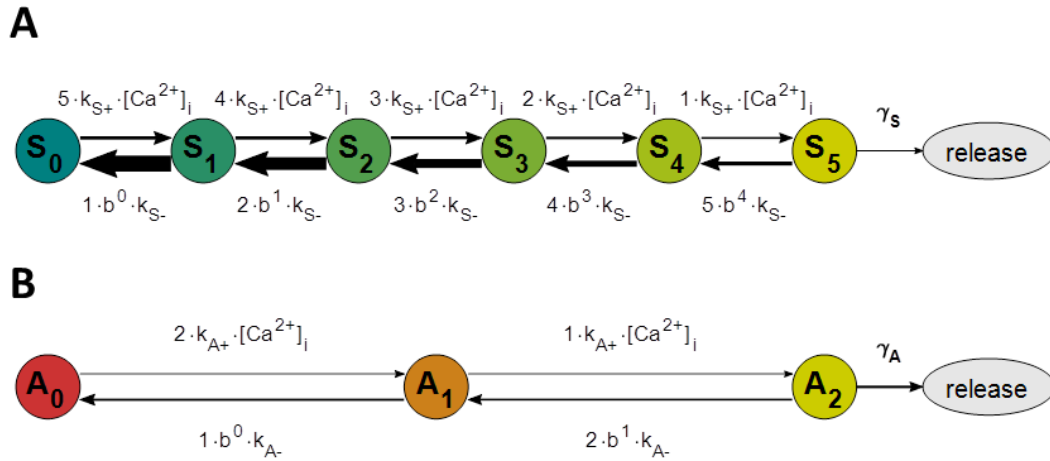


**Figure 2.4: Synaptotagmin-Mediated Neurotransmitter Release State Diagram.**

Model adapted from Sun et al. (2007). (A)  $\text{Ca}^{2+}$ -bound states for Syt-1 (synchronous release);  $S_n$  indicates  $n$   $\text{Ca}^{2+}$  ions bound to the synchronous release mechanism. (B)  $\text{Ca}^{2+}$ -bound states for Syt-7 (asynchronous release);  $A_n$  indicates  $n$   $\text{Ca}^{2+}$  ions bound to the asynchronous release mechanism. (A, B)  $\gamma_S$  and  $\gamma_A$  represent rates of vesicle fusion from the releasable states of the synchronous and asynchronous mechanisms, respectively.

**Table 2.2: SNARE Release State Transition Parameters.**

Values taken from Nadkarni et al. (2010), adapted from Sun et al. (2007).

synchronous	asynchronous	other parameters
$k_{S+}$ $6.12 \times 10^7 \text{ M}^{-1}\text{s}^{-1}$	$k_{A+}$ $3.82 \times 10^6 \text{ M}^{-1}\text{s}^{-1}$	$b$ 0.25
$k_{S-}$ $2.32 \times 10^3 \text{ s}^{-1}$	$k_{A-}$ $13 \text{ s}^{-1}$	$\epsilon$ 6.34 ms
$\gamma_S$ $6.0 \times 10^3 \text{ s}^{-1}$	$\gamma_A$ $50 \text{ s}^{-1}$	

## 2.1.2 Deterministic Simulations of State Probabilities

With the  $\text{Ca}^{2+}$  profiles obtained for each spike-evoked simulation in MCell and with the state transitions for the release mechanisms defined above, the corresponding vesicle release-rate profiles become computable. While MCell does generate its own set of release times, they lack the desired level of precision for fitting phenomenological functions to the release histograms without running an infeasibly large number of simulations. Furthermore, vesicle depletion following release events confounds the representation of release rate, its functional form, and its facilitation dynamics. Therefore, instead of running millions of trials of MCell (or more) to produce temporally precise single-vesicle release rate histograms, we used the averaged calcium profiles from 2000 trials to drive a deterministic simulation of the SNARE complex, in particular, of the probabilities of being in each state as functions of time. This approach, in effect, produced the average release histograms equivalent to an infinite number of trials acting on the averaged calcium traces.

This simulation tracked the probabilities of a particular release mechanism being in each possible state at every time step. That is, each state represents the number of  $\text{Ca}^{2+}$  ions bound to the release molecule (0 through 5 for Syt-1 (synchronous) and 0 through 2 for Syt-7 (asynchronous)). State probabilities add to unity, and they update on each time step according to a  $\text{Ca}^{2+}$ -dependent state transition matrix. Specifically, for mechanism  $X$  with  $N_X$  calcium ions needed for release to occur, the binding rate is

$$T_{n+1,n} = (N_X - n) \cdot k_{X+} \cdot [\text{Ca}^{2+}]_i, \quad (2.8)$$

and the unbinding rate is

$$T_{n-1,n} = n \cdot b^{n-1} \cdot k_{X-} \quad (2.9)$$

for  $n \in \{0 \dots N_X\}$  ions currently bound, where  $b = 0.25$  acts as a binding cooperativity factor (see Figure 2.4 for state diagram and Table 2.2 for values).

The state transition matrix is thus a tridiagonal  $(N_X + 1) \times (N_X + 1)$  matrix  $\mathbf{T}$  whose superdiagonal terms are the unbinding rates, moving from a higher to a lower state, and whose subdiagonal terms are the binding rates, moving from a lower to a higher state. To maintain a constant sum for the state probability vector  $\mathbf{s}(t)$  (an  $(N_X + 1) \times 1$  column vector), the diagonal terms must follow the combined rate of leaving the current state (through binding or unbinding):

$$\begin{aligned} T_{n,n} &= -(T_{n+1,n} + T_{n-1,n}) \\ &= -((N_X - n) \cdot k_{X+} \cdot [\text{Ca}^{2+}]_i + n \cdot b^{n-1} \cdot k_{X-}). \end{aligned} \quad (2.10)$$

With a time step of  $\Delta t$ , the state vector on the next time step will be

$$\mathbf{s}(t + \Delta t) = [\mathbf{I} + \Delta t \cdot \mathbf{T}([\text{Ca}^{2+}]_i(t))] \mathbf{s}(t). \quad (2.11)$$

The above description, however, does not take into account vesicle fusion. Each mechanism  $X$  induces neurotransmitter release at a certain rate  $\gamma_X$  (see Table 2.2) from its releasable state (all  $\text{Ca}^{2+}$  ions bound). When release occurs, the vesicle can no longer participate in further activity. Therefore, before applying the transition matrix, the occupancy of the releasable state decreases by the probability of a release occurring during the time step:

$$s_{N_X} \leftarrow s_{N_X} \cdot (1 - \gamma_X \Delta t). \quad (2.12)$$

However, this still leaves the same problem as before, where depletion obscures the single-vesicle probabilistic release rate. To account for this, we then normalize the state vector at each time step by the probability of no release event having occurred, such that the occupancies in each state again add to one:

$$\mathbf{s}(t) \leftarrow \frac{\mathbf{s}(t)}{\|\mathbf{s}(t)\|}. \quad (2.13)$$

If one considers the deterministic simulation to represent a state histogram averaged over an infinite number of trials, this normalization step effectively “zooms in”

on the fraction of trials at each time step for which no release occurred. Thus, the model tracks the instantaneous  $\text{Ca}^{2+}$ -dependent rate of release for each mechanism, given that no release has yet occurred since the start of the simulation. This permits the calculation, for example, of the equilibrium probabilistic state vector for a docked vesicle, which is necessary for initializing all other simulations, using the steady-state  $\text{Ca}^{2+}$  concentration (100 nM in MCell: (Nadkarni et al., 2010)) as input to the simulation. From these, it is possible to determine the steady-state release rates for each mechanism, even though they are very small (see Table 2.2 in Methods 2.1.1.3).

A similar approach was used for calculating the states of the well-mixed models, and the resulting  $\text{Ca}^{2+}$  traces, as functions of time. For these simulations, diffusion was assumed to occur instantaneously, effectively eliminating space from consideration, but all other mechanisms from the original MCell model were included (see Figures 2.1, 2.2, 2.4 and Tables 2.1, 2.2 in Methods 2.1.1).

### **2.1.3 Stimulus Protocols for Exploring Facilitation**

Whereas simulations with single action potentials (APs) can elucidate the functional form of synchronous and asynchronous release, stimulus trains of multiple spikes can reveal the dynamics of facilitation in release probability, which is well documented experimentally (Neher & Sakaba, 2008; Rosahl et al., 1993; Stevens & Wang, 1995; Thomson & Bannister, 1999; M. Tsodyks et al., 1998; Varela et al., 1997; Zucker & Regehr, 2002). Short-term facilitation in release probability is more pronounced for spikes closer together in time than for those separated by long intervals. To investigate how delay affects probability of release, we studied paired-pulse facilitation (PPF) for interspike intervals (ISIs) of exponentially increasing delay. Specifically, we stimulated the MCell model with paired pulses of AP-like waveforms separated by 2, 5, 10, 20, 50,

100, and 200 ms and measured the local  $[Ca^{2+}]_i$  at a point within the axon, as described in Methods 2.1.1.2. These  $Ca^{2+}$  traces then drove deterministic simulations of synchronous and asynchronous release rate, as described in Methods 2.1.2. This permitted me to determine a functional form to describe PPF (see Results 2.2.5).

Realistic spike trains, however, involve patterns much more complex than paired pulses, and the recent history of presynaptic activity can have a strong effect on future changes in release probability. To see how facilitation evolves in more complex trains of APs, we designed a protocol to explore the full space of possible facilitated states, assuming that the level of facilitation experienced on one spike depends exclusively on the delay since the previous spike (the interspike interval, or ISI) and on the state of some internal facilitation parameter from the previous spike. The spike trains generally consist of two phases: a spiking ramp and a probe spike. The ramp phase explores how facilitation develops with multiple spikes at fixed ISIs and having anywhere from one to five spikes with an ISI of 2, 5, 10, or 20 ms (time prevented the exploration of ramps with more spikes). The probe phase explores how facilitation wears off with increasing delay between spikes and consists of a single spike at 2, 5, 10, 20, 50, 100, or 200 ms after the end of the ramp, as in the PPF protocol above. All these combinations of ramps and probes add up to  $5 \times 4 \times (7 + 1) = 160$  cases (including those cases without a probe spike) or 136 unique spike trains (discounting the repeats with one spike in the ramp at different ISIs).

#### **2.1.4 Algorithms for Fitting Parameters and Metaparameters**

Fitting parameter values to the shapes of the release-rate histograms involved two steps: first, obtaining an initial guess, and second, optimizing the parameter values to a best-fit set. For the first step, the time constants for rate decay (see Equations 2.17,

2.18, etc. in Results 2.2.3) were found from the slopes of the logarithms of the profiles (see Equation 2.16 and Figure 2.9 in Results 2.2.2) in response to both  $\text{Ca}^{2+}$  impulse and the  $\text{Ca}^{2+}$  traces derived from MCell (see Results 2.2.1, 2.2.2). Other parameters were initialized through trial and error. For the second step, I applied the Nelder-Mead simplex method of function optimization (McKinnon, 1998; Nelder & Mead, 1965) to minimize the error function over the parameters. This method does not require a measure of the error gradient, which was not exactly computable. The error function was computed as the fraction of the variance unexplained (FVU) by the model, as in

$$\text{FVU}(y(t), f(t)) = \frac{\sum_{n=1}^{N_t} (y(t_n) - f(t_n))^2}{\sum_{n=1}^{N_t} (y(t_n) - \bar{y})^2}, \quad (2.14)$$

where  $\bar{y}$  is the mean release rate,  $y(t)$  is the true release histogram shape, and  $f(t)$  is the model profile at the same  $N_t$  time points. More precisely, the error function  $\epsilon$  is a linear combination of the FVU for the function and for the logarithm of the function:

$$\epsilon(y(t), f(t)) = \alpha \cdot \text{FVU}(y(t), f(t)) + \beta \cdot \text{FVU}(\log(y(t)), \log(f(t))), \quad (2.15)$$

where  $\alpha$  and  $\beta$  are constants. The metaparameters of the facilitation functions (see Results 2.2.5.1) were fitted after the parameters were fitted to the release profiles in response to each spike of the trains described in Methods 2.1.3. The fitted parameters were taken as true, and the space of the logarithms of the metaparameters  $\tau$ ,  $N$ , and  $L = N^\xi$  (see Results 2.2.5.1) was explored, using the same error function and optimization as above.

## 2.2 Results

### 2.2.1 MCell and Deterministic Simulations

In response to an action potential (AP) stimulus, voltage-dependent  $\text{Ca}^{2+}$  channels (VDCCs) transition stochastically to an open state, through which  $\text{Ca}^{2+}$  ions may enter

the axon down a sharp electrochemical gradient (Bischofberger et al., 2002; Körber & Kuner, 2016). Because this process does not depend on diffusion, a deterministic simulation of state probabilities can perfectly capture the shape of the histogram of  $\text{Ca}^{2+}$  influx rate averaged over infinite trials, as in Figure 2.5. Notice that the rate of influx rises to a peak and returns completely to baseline within a span of about 2 ms, so any spike-evoked vesicle fusion after this initial influx is due entirely to internal dynamics as  $\text{Ca}^{2+}$  diffuses, interacts with the buffer and  $\text{Ca}^{2+}$  sensors, and vacates through the pumps.

Most neurotransmitter release occurs within a sharp window after an AP stimulus (Sakaba, 2006; Schneggenburger & Neher, 2000; Wölfel, Lou, & Schneggenburger, 2007; Xu, Pang, Shin, & Südhof, 2009). The presence of the  $\text{Ca}^{2+}$  buffer calbindin plays an instrumental role in this by rapidly removing most of the free  $\text{Ca}^{2+}$  and then slowly releasing it over an extended period at a rate that the active PMCA pumps can handle. This action significantly tightens the window for Syt-1-mediated synchronous release (Delvendahl et al., 2015; Fioravante & Regehr, 2011) while also extending the time window for Syt-7-mediated asynchronous release. Without a buffer, however, the free  $[\text{Ca}^{2+}]_i$  does not drop off immediately but decays linearly toward baseline over a few tens of milliseconds, saturating the capacity of the PMCA pumps to remove the ions (Figure 2.6A,B). Thus, removing calbindin from the simulations both amplifies synchronous release in a time window near the spike and suppresses asynchronous release long after the stimulus (Figure 2.6C,D). This agrees with experimental evidence that endogenous  $\text{Ca}^{2+}$  buffers limit the rate of synchronous synaptic release (Delvendahl et al., 2015).

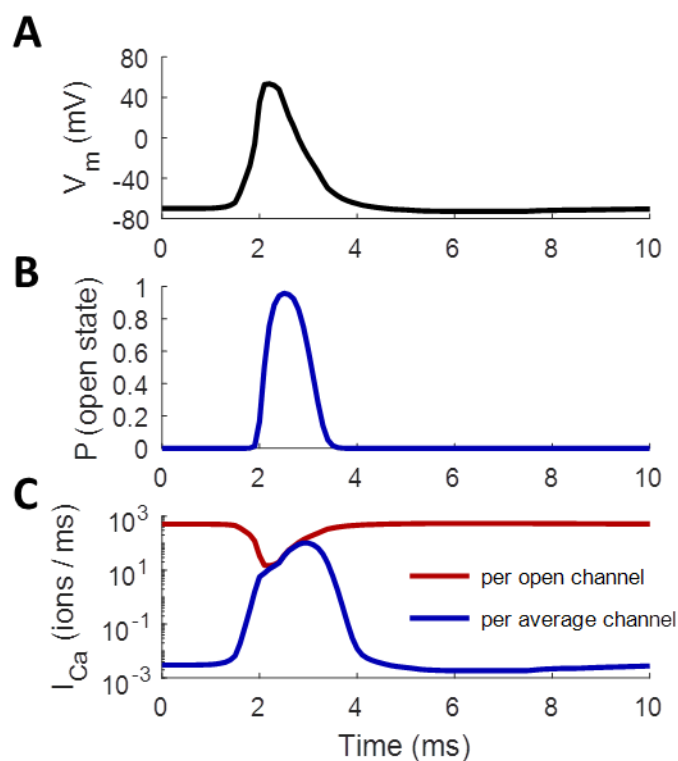


**Figure 2.5: Action-Potential-Evoked  $\text{Ca}^{2+}$  Current.**

(A) AP-like waveform applied to axon. (B) Probability of a single VDCC being in the open state in response to the AP in (A) increases from about  $10^{-5}$  to around 96% during the spike before quickly shutting off; computed from deterministic simulation of state probabilities (see Methods 2.1.1.1, 2.1.2). (C) Rate of  $\text{Ca}^{2+}$  influx through a single, pathologically open channel (red) and through a typical channel (blue), whose probability of being open follows (B).

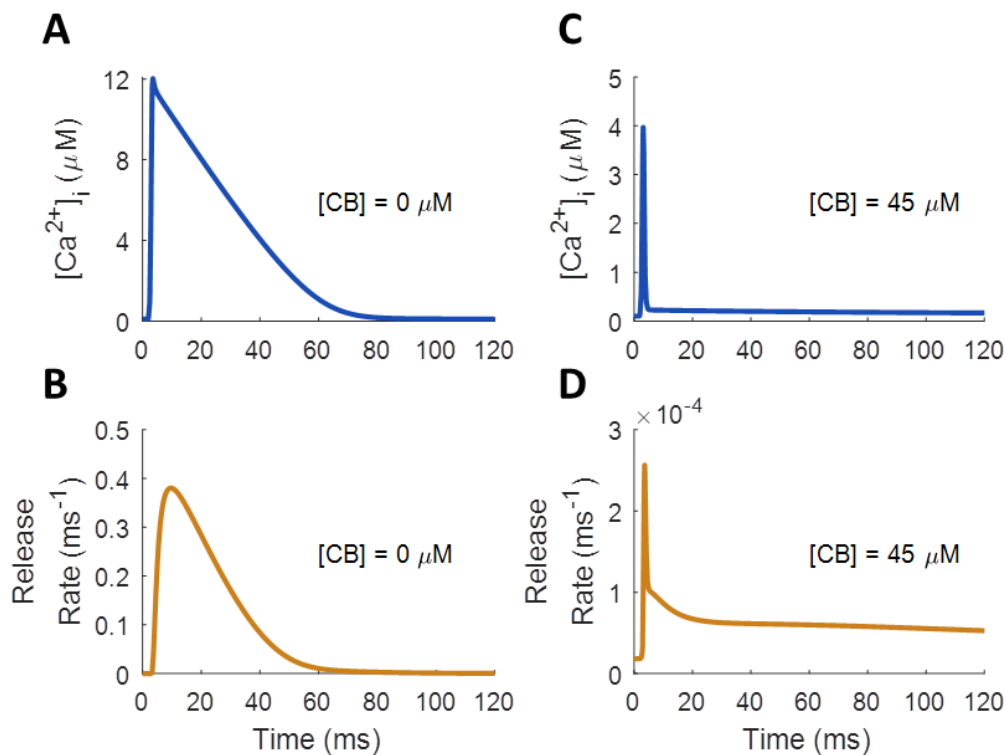


**Figure 2.6: Effect of Calbindin Buffer on Spike-Evoked  $Ca^{2+}$  Profile and Release Rates.**

AP-like stimulus delivered to model axon starting at 0 ms. Diffusion is assumed to be instantaneous, and molecular state probabilities are tracked deterministically over time (see Methods 2.1.1.3, 2.1.2). (A) Free  $[Ca^{2+}]_i$  with no calbindin buffer decays linearly with time due to saturation of PMCA pumps. (B) Syt-1/7-mediated release rates are large but short-lived in response to unbuffered  $Ca^{2+}$ . (C) Free  $[Ca^{2+}]_i$  with calbindin added to the axon has much smaller magnitude and much narrower peak but has much longer tail. (D) Vesicle release in response to buffered  $Ca^{2+}$  is much less pronounced. The calbindin buffer reduces the rate of synchronous transmission but extends the window for pronounced asynchronous transmission.

Diffusion plays a key role in all of these processes. Simplified models of  $\text{Ca}^{2+}$ -dependent presynaptic dynamics may assume that the synapse is locally well mixed, equivalent to saying that diffusion happens infinitely fast, at least relative to the spatial and temporal scales being studied. However, MCell allows one to add a spatial component to molecular simulations, which can account for certain phenomena that well mixed molecular kinetics models cannot capture (Rex A Kerr et al., 2008; Stiles & Bartol, 2001; Stiles et al., 1996). In this case, diffusion of the  $\text{Ca}^{2+}$  and calbindin through the axonal volume reveals how distance from the  $\text{Ca}^{2+}$  source affects both the timing and the probability of spike-evoked vesicle release. Figure 2.7 compares the deterministic simulation without diffusion to the equivalent MCell simulations performed at multiple distances from the VDCC  $\text{Ca}^{2+}$  source. The shape of the  $\text{Ca}^{2+}$  transient measured in MCell displays marked qualitative differences from that obtained without diffusion:  $\text{Ca}^{2+}$  sensors near the VDCC source see a much higher peak concentration with an extra component of decay immediately following the peak; those farther away progressively lose the fast peak until nothing is left but an extremely small distance-independent component. The extra component of the proximal  $\text{Ca}^{2+}$  curve, which does not appear in the well-mixed model, likely arises from local saturation in the nanodomains near the VDCC cluster, where the very high free  $[\text{Ca}^{2+}]_i$  temporarily saturates both the calbindin buffer and the PMCA pumps (Fioravante & Regehr, 2011). Farther out, the MCell model qualitatively matches the well-mixed model more closely, until at very large distances, the fast components almost completely disappear. The distance-independent components represent a sustained global elevation in  $[\text{Ca}^{2+}]_i$  that persists due to the excess  $\text{Ca}^{2+}$  that has yet to unbind from the calbindin buffer. The slowest component has a magnitude comparable to resting  $[\text{Ca}^{2+}]_i$  and a time constant of around 1 second.

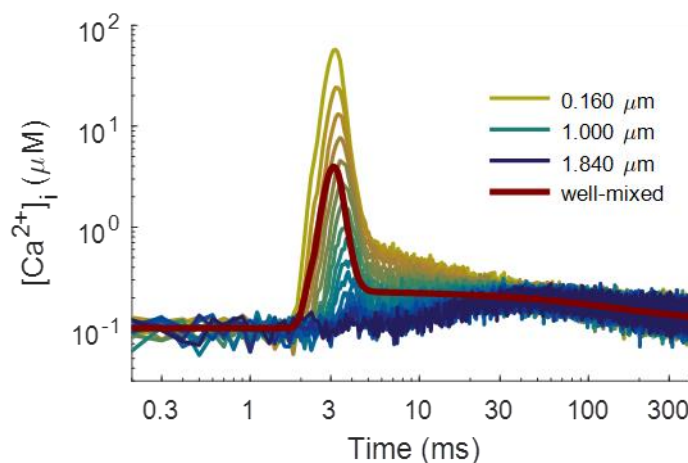


**Figure 2.7: Spatial Modeling Important for Capturing Fine-Grain Features of  $\text{Ca}^{2+}$  Transients.**

$[\text{Ca}^{2+}]_i$  measured over time in MCell (colored) and in the deterministic well-mixed model (maroon). Color transitions from yellow for vesicles proximal to the VDCC  $\text{Ca}^{2+}$  source to blue for vesicles far away (see Figure 2.15 in Results 2.2.4). Proximally (distally) measured  $[\text{Ca}^{2+}]_i$  displays more (fewer) components of decay than are evident in the deterministic model.

The MCell model, because it tracks thousands of individual particles through Markov chain Monte Carlo simulations (Rex A Kerr et al., 2008; Stiles & Bartol, 2001; Stiles et al., 1996), can both capture very realistic synaptic dynamics and uncover their underlying molecular causes, which would be difficult to obtain through other methods. Unfortunately, this realism can also obscure the patterns necessary for building simplified models. First, many processes, such as asynchronous or “mini” release events (Kato, Sekino, Takahashi, Yasuda, & Shirao, 2007; Malgaroli & Tsien, 1992; Nanou, Sullivan, Scheuer, & Catterall, 2016), occur slowly enough that many thousands or millions of simulated trials would be required to uncover precise functional descriptions, which could become computationally prohibitive. For instance, the histograms of synchronous release obtained from 2000 trials of MCell in Figure 2.8 offer little information on spontaneous release from the Syt-1 mechanism between APs, and

synchronous release far from the VDCC cluster (blue) hardly occurs at all. Second, the fact that vesicles deplete upon release hides how the instantaneous single-vesicle release rate actually changes with time. The tails of the release distributions fall off too quickly as vesicles are removed from the simulation over time, and any paired-pulse facilitation (PPF) in single-vesicle release probability is countered by the release-dependent depletion in the model (Figure 2.8). The only way to avoid these depletion effects in MCell would be to run many millions of trials with a single vesicle to track how the vesicle's alacrity for release fluctuates with the  $\text{Ca}^{2+}$  history detected at its position. For these reasons, I decided not to depend on the release histograms generated by many trials of MCell for building a phenomenological model. Instead, I used the  $\text{Ca}^{2+}$  traces generated by MCell, which do not suffer from the aforementioned problems, to drive deterministic simulations of the SNARE dynamics (as described in Methods 2.1.2), effectively producing what an infinite number of trials would produce in MCell with the name  $\text{Ca}^{2+}$  data. Thus, using the deterministic release rates driven by the stochastic MCell  $\text{Ca}^{2+}$  data balances the necessary realism of MCell with the smoothness and insights required for designing a versatile phenomenological model.

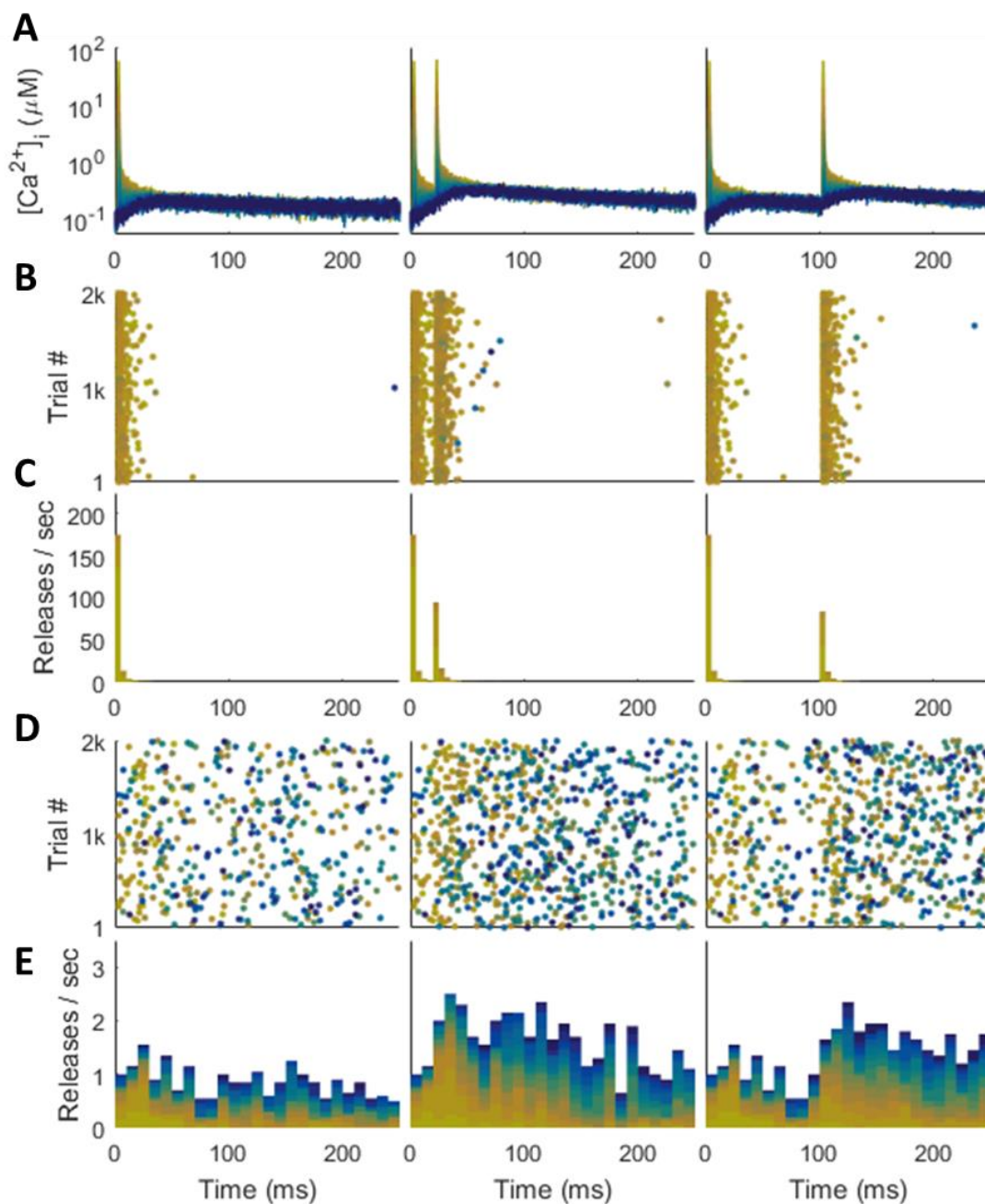


**Figure 2.8: Synchronous and Asynchronous Release in MCell.**

Color indicates distance from VDCC source, with yellow representing a nearby  $\text{Ca}^{2+}$  sensor and dark blue a distant one. AP-like stimulus delivered at 0 ms (left), followed by another at 20 ms (center) and 100 ms (right). (A) AP-evoked  $\text{Ca}^{2+}$  traces that drive release. (B) Synchronous release raster. (C) Synchronous release stacked histogram; most releases happen close to the  $\text{Ca}^{2+}$  source. (D) Asynchronous release raster. (E) Asynchronous release stacked histogram; releases distributed across all distances.

## 2.2.2 Baseline and Impulse-Response Release Rate Functions

Most of the  $\text{Ca}^{2+}$  that enters the axon following an AP quickly binds with the calbindin buffer, causing a narrow spike in the free  $[\text{Ca}^{2+}]_i$ . Therefore, most of the spike-evoked release occurs in response to this narrow window of influx. To test how each release mechanism responds to transient  $\text{Ca}^{2+}$  spikes, I supplied an instantaneous burst of  $\text{Ca}^{2+}$  to a single time step of the deterministic model, allowing me to measure the impulse-response function. These simulations were repeated for various resting  $\text{Ca}^{2+}$  levels ( $[\text{Ca}^{2+}]_{i0}$ ), ranging from 0 to 100  $\mu\text{M}$  to see how the presence of  $\text{Ca}^{2+}$  at rest affects the response to spike-evoked transients. As Figure 2.9 shows, when there is no resting  $[\text{Ca}^{2+}]_i$ , the rate of release for both synchronous and asynchronous mechanisms rises quickly in response to a sudden influx before dropping exponentially with a single exponential component (black). However, when the  $[\text{Ca}^{2+}]_{i0}$  settles at some level greater than zero, an extra exponential component emerges for both mechanisms (blue and red lines). The exponential decay time constants seem to be mostly independent of resting  $[\text{Ca}^{2+}]_{i0}$  at low levels, but they drop off more quickly as spontaneous release rates begin to overtake the spike-evoked rates at high concentrations. The extra component emerges as a result of the back-and-forth  $\text{Ca}^{2+}$ -binding and unbinding processes, where finite baseline  $[\text{Ca}^{2+}]_{i0}$  likely provides a “floor” to “bounce off of” in terms of the number of  $\text{Ca}^{2+}$  ions bound to the release mechanism. Note, however, that even though it depends on equilibrium  $[\text{Ca}^{2+}]_{i0}$ , this secondary release component is still purely spike-evoked and arises due to the nonlinearity of the system. To calculate the time constants of exponential decay, I used the slope of the logarithm of the release rate curve according to

$$\tau(t) = - \left( \frac{d}{dt} [\ln(r(t) - r(0))] \right)^{-1}, \quad (2.16)$$

where  $\tau(t)$  is the instantaneous time constant and  $r(t)$  is the instantaneous release rate. The baseline rate  $r(0)$  was subtracted off to ensure that the function approached zero prior to taking the logarithm.

Of course, the existence of a nonzero  $[\text{Ca}^{2+}]_{i0}$  implies that the  $\text{Ca}^{2+}$ -sensors of the SNARE complex will induce vesicle fusion at some finite, if extremely slow, rate. At very low concentrations, this would require anywhere from many thousands to many trillions of trials to build up sufficiently informative release histograms. Instead, I reran the deterministic model at constant values of  $[\text{Ca}^{2+}]_i$  with no  $\text{Ca}^{2+}$  spike and measured the steady-state release rates after 10 seconds of simulated time (Figure 2.10). Perhaps unsurprisingly, the spontaneous release rates grow in proportion to the 5<sup>th</sup> (2<sup>nd</sup>) power of  $[\text{Ca}^{2+}]_{i0}$  for synchronous (asynchronous) release, according to the number of  $\text{Ca}^{2+}$  ions needed to bind before the synaptotagmin can initiate fusion. At very high  $[\text{Ca}^{2+}]_{i0}$ , though, the release rates saturate to  $\gamma_S$  and  $\gamma_A$  (see Table 2.2 in Methods 2.1.1.3) as the probability of being in the releasable state approaches one.

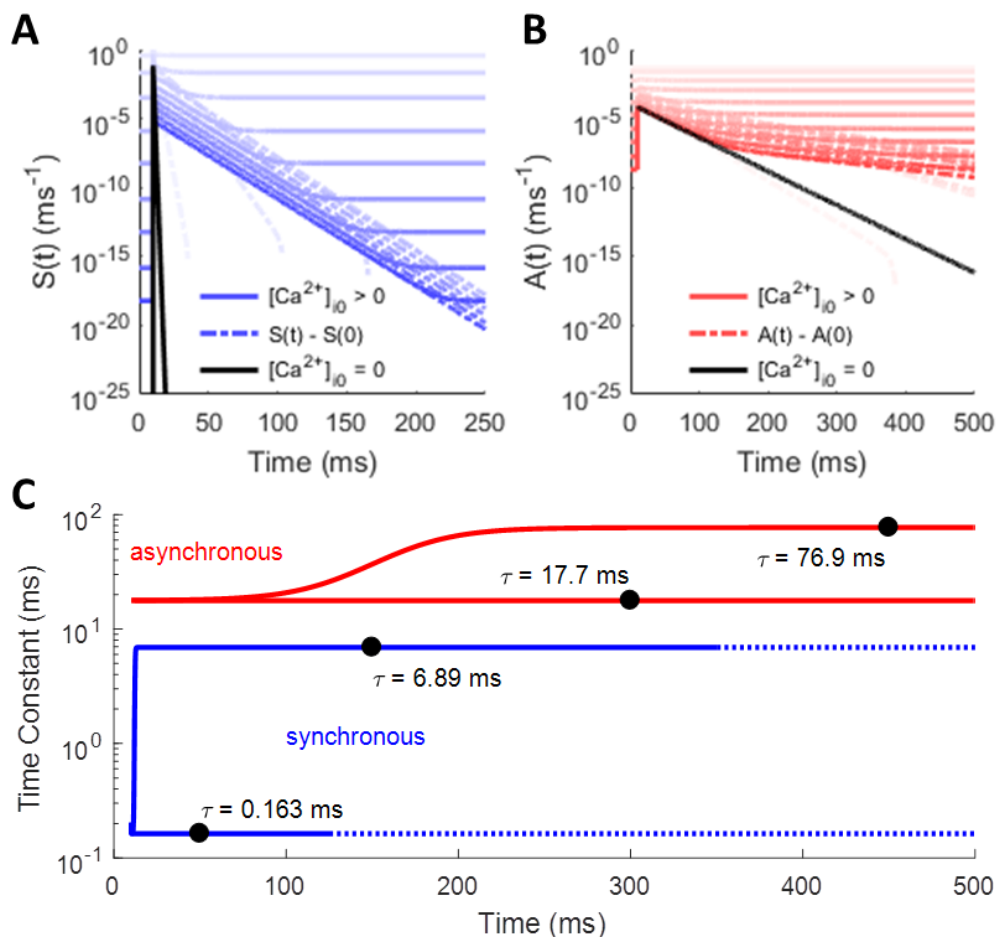


**Figure 2.9: Synchronous and Asynchronous Release Rates in Response to  $\text{Ca}^{2+}$  Impulse at Different Resting Concentrations.**

Instantaneous impulse of  $\text{Ca}^{2+}$  delivered at 10 ms. Solid lines represent true release rate; dotted lines have spontaneous rates subtracted off to show secondary exponential components. Black lines show release rate decaying with a single exponential component with no baseline  $[\text{Ca}^{2+}]_i$ . For other curves,  $[\text{Ca}^{2+}]_{i0}$  ranges from 0.001  $\mu\text{M}$  to 100  $\mu\text{M}$ . (A) Synchronous release rate over time:  $S(t)$ . (B) Asynchronous release rate over time:  $A(t)$ . (C) Instantaneous release rate decay time constants for synchronous and asynchronous mechanisms. Fast components (lower blue and red lines) determined from profiles with  $[\text{Ca}^{2+}]_{i0} = 0$  (black lines in A and B). Slower components (upper blue and red curves) determined from cases with small  $[\text{Ca}^{2+}]_{i0}$ .

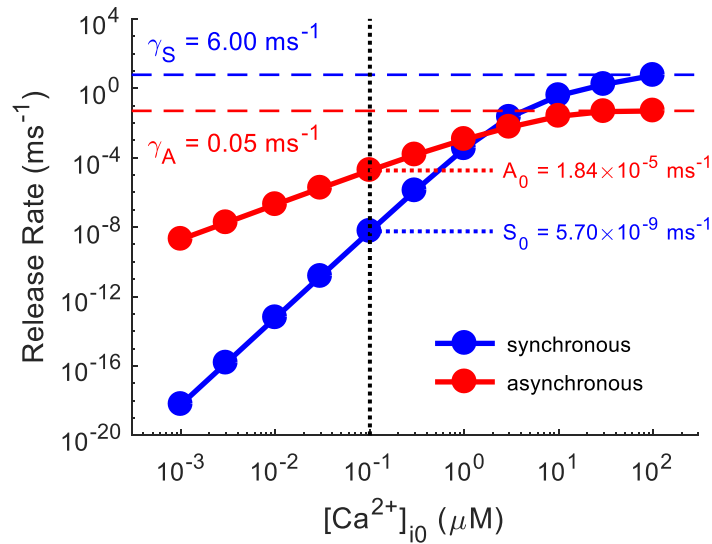


**Figure 2.10: Spontaneous Rates of Vesicle Fusion Increase with  $[Ca^{2+}]_{i0}$ .**

For small  $[Ca^{2+}]_{i0}$ ,  $S_0 = k_S \cdot ([Ca^{2+}]_{i0})^5$  and  $A_0 = k_A \cdot ([Ca^{2+}]_{i0})^2$ , where  $k_S \approx 6 \times 10^{-4} \text{ ms}^{-1} \cdot \mu\text{M}^{-5}$  and  $k_A \approx 2 \times 10^{-3} \text{ ms}^{-1} \cdot \mu\text{M}^{-2}$ . As  $[Ca^{2+}]_{i0} \rightarrow \infty$ ,  $S_0 \rightarrow \gamma_S$  and  $A_0 \rightarrow \gamma_A$ . Values for  $S_0$  and  $A_0$  at  $[Ca^{2+}]_{i0} = 100 \text{ nM}$ , which is used throughout most of the chapter, are pointed out for reference.

From the above, it would seem that each mechanism should have three components to its release histogram: a constant spontaneous rate that increases with  $[Ca^{2+}]_i$ , a fast exponential component that acts in response to an impulse of spike-evoked  $Ca^{2+}$ , and a slower spike-evoked component that results from a “rebound” interaction with the  $Ca^{2+}$  floor. However, the profiles of the release rate histograms display more complexity than this, which will be discussed in more detail in the following section. Significantly,  $[Ca^{2+}]_i$  does not drop instantly to baseline after the initial influx, but some leftover  $Ca^{2+}$  continues to have a small effect over a long time window as it slowly unbinds from the calbindin buffer (see Figure 2.6 in Results 2.2.1). This allows a small but noticeably enhanced rate of release efficacy to continue out to hundreds or thousands of milliseconds before returning fully to baseline (within noise). Figure 2.11

shows the effect that this latent  $\text{Ca}^{2+}$  has on the producing longer time constants in the decay of the release rate profiles, using the smooth curves obtained from the well-mixed model.

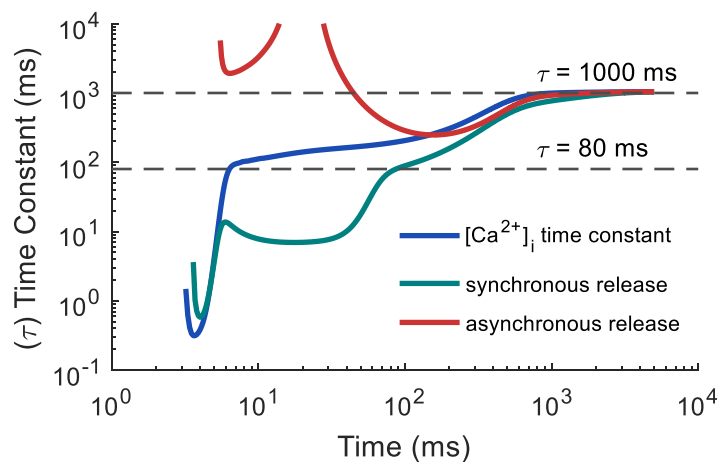


**Figure 2.11: Slow Un-buffering of Latent  $\text{Ca}^{2+}$  Leads to Longer Time Constants for Synchronous and Asynchronous Release.**

Instantaneous time constants for  $\text{Ca}^{2+}$ , synchronous, and asynchronous curves. Long release rate time constants (around 80 ms and 1000 ms; dashed lines) follow  $\text{Ca}^{2+}$  curve. Asynchronous starts high because fast and slow components have comparable magnitude and become conflated; it goes up to infinity where additive effects cause the curve to flatten.

### 2.2.3 Release Rate Functions from $\text{Ca}^{2+}$ Dynamics

By driving a deterministic simulation of SNARE dynamics (see Methods 2.1.2) with the  $[\text{Ca}^{2+}]_i$  waveform obtained from MCell (see Methods 2.1.1), one can see that each release mechanism induces vesicle fusion with a histogram (Figure 2.12) that essentially follows a multi-exponential form. The release rate profiles ( $r(t)$ , where  $r \in \{S, A\}$  may refer to synchronous or asynchronous release rate) rise quickly from baseline after the AP and decay with several exponential components, approximated as

$$r(t) = r_0 + \sum_{j=1}^n \frac{P_j}{\tau_j} \left( e^{-t/\tau_j} u(t) \right), \quad (2.17)$$

where  $r_0$  is the spontaneous release rate (related to “mini”-EPSCs (Kaesler & Regehr, 2014; Kato et al., 2007; Malgaroli & Tsien, 1992)),  $t$  is the time since the last spike,  $u(t)$  is the Heaviside step function (so that release occurs only for  $t \geq 0$ ),  $\tau_j$  are the time constants of exponential decay, and  $P_j$  are the expected number of releases from each component for a single vesicle. Note that because the release rate profile is not a probability distribution, but rather it represents the instantaneous rate of release conditioned on having not released yet (see Methods 2.1.2), its integral  $P_j$  can potentially exceed one. The probability that the exponential component causes release at any point in time is  $p_{rj} = 1 - \exp(-P_j)$

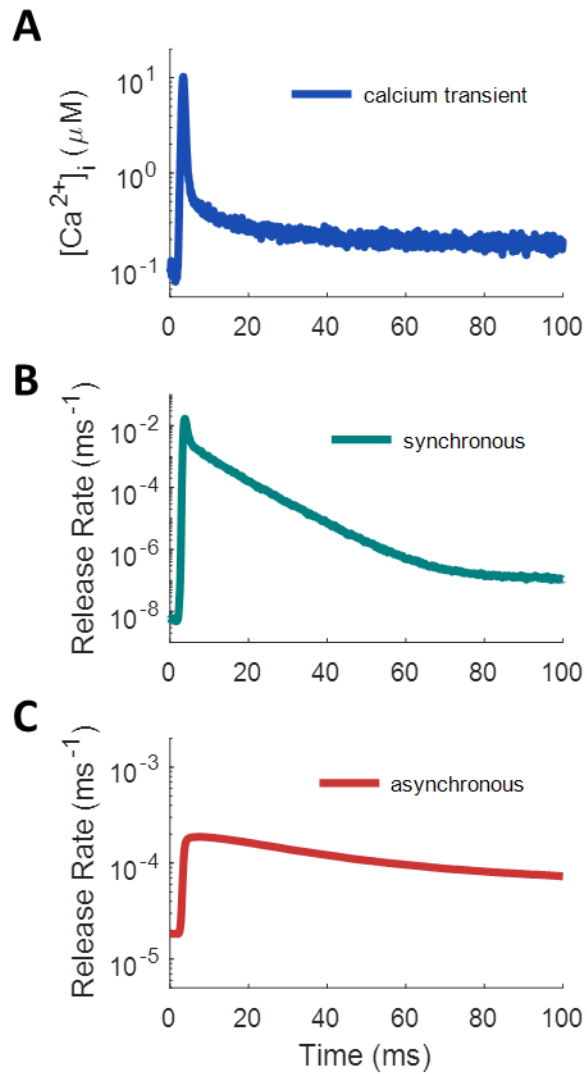


**Figure 2.12: Multi-Exponential Shape of  $Ca^{2+}$ -Driven Vesicle Release Rate.**

All plots given as semi-log to highlight exponential decay components (straight line segments of profiles). (A) A single, spike-evoked  $[Ca^{2+}]_i$  transient, which drives (B) the synchronous release rate and (C) the asynchronous release rate.

### 2.2.3.1 Temporal Filter of Release Rate Histograms

Of course, release of neurotransmitter cannot begin at exactly the moment of the spike, both because the AP itself is not entirely an instantaneous process and because it takes finite time for  $\text{Ca}^{2+}$  to diffuse from the VDCC source, through the buffer, to the  $\text{Ca}^{2+}$  sensor in the SNARE complex. MCell represents this complex process with a Markov chain Monte Carlo simulation (MCMC). Because of this, the release process, wherein sufficient  $\text{Ca}^{2+}$  must accumulate on the synaptotagmin to initiate fusion, cannot begin until the spike-evoked  $\text{Ca}^{2+}$  arrives, which time may vary randomly relative to the timing of the AP. Thus, the MCMC process acts as a temporal filter on the release dynamics, transforming the equation of release to

$$r(t) = r_0 + \sum_{j=1}^n \frac{P_j}{\tau_j} \left( e^{-t/\tau_j} u(t) \right) * a(t; k_j, \mu_j, \sigma_j), \quad (2.18)$$

where  $a(\cdot)$  is the temporal filter and  $k_j$ ,  $\mu_j$ , and  $\sigma_j$  are parameters to be discussed below. The convolution operation effectively smears the release profile over time to account for random temporal shifts across trials.

Importantly, the release-start-time filter  $a(\cdot)$  must integrate to one over all real numbers. That way, it does not affect the probability of release, only its timing. The temporal filter chosen is an ex-Gaussian distribution, resulting from the convolution of an exponential distribution of rate  $k$  with a normal distribution of mean  $\mu$  and standard deviation  $\sigma$ :

$$\begin{aligned}
a(t; k, \mu, \sigma) &= \left( k e^{-kt} u(t) \right) * \left( \frac{1}{\sigma\sqrt{2\pi}} e^{-\frac{(t-\mu)^2}{2\sigma^2}} \right) \\
&= \int_{-\infty}^t k e^{-k(t-t')} \frac{1}{\sigma\sqrt{2\pi}} e^{-\frac{(t'-\mu)^2}{2\sigma^2}} dt' \\
&= k e^{-k\left(t - \left(\mu + \frac{\sigma^2}{2}k\right)\right)} \Phi\left(\frac{t - (\mu + \sigma^2 k)}{\sigma}\right), \tag{2.19}
\end{aligned}$$

where  $\Phi(\cdot)$  represents the CDF of the zero-mean, unit-variance normal distribution. In the limit where  $\sigma \rightarrow 0$ , this CDF simply becomes the shifted step function  $u(t - \mu)$ , and  $a(t; k, \mu, \sigma) \rightarrow k e^{-k(t-\mu)} u(t - \mu)$ , which is just a rightward shift of the exponential distribution by  $\mu$ . The values of  $\mu$  and  $\sigma$  result from the sum of the delays caused by numerous random processes, including the timing of  $\text{Ca}^{2+}$  entry relative to the AP, the accumulation of collision events during Brownian motion, and the binding/unbinding events with the calbindin buffer. Assuming that the individual events of the buffered diffusion process are numerous and similar enough for a given spike, the central limit theorem states that the sum of their delays should approximate a normal distribution (DasGupta, 2010). The value of  $k$  represents the rate of some limiting step in the process of buffered diffusion, and it slows with increasing distance between the VDCC source and the  $\text{Ca}^{2+}$  sensor in the SNARE complex (see Methods 2.1.1.1). Keep in mind that these parameters constitute only a phenomenological approximation to the exact filter, but they work well enough for the purposes of this chapter.

Applying this filter in Equation 2.18, focusing on a single component and removing subscripts for simplicity, yields

$$\begin{aligned}
r(t) &= \frac{P}{\tau} \left( e^{-t/\tau} u(t) \right) * a(t; k, \mu, \sigma) \\
&= \frac{P}{\tau} \left( e^{-t/\tau} u(t) \right) * \left( k e^{-kt} u(t) \right) * \left( \frac{1}{\sigma\sqrt{2\pi}} e^{-\frac{(t-\mu)^2}{2\sigma^2}} \right) \\
&= \left( P \frac{k}{k\tau - 1} (e^{-t/\tau} - e^{-kt}) u(t) \right) * \left( \frac{1}{\sigma\sqrt{2\pi}} e^{-\frac{(t-\mu)^2}{2\sigma^2}} \right). \tag{2.20}
\end{aligned}$$

Stopping here and replacing the Gaussian with a delta function by letting  $\sigma \rightarrow 0$  yields

$$r(t) = P \frac{k}{k\tau - 1} (e^{-(t-\mu)/\tau} - e^{-k(t-\mu)}) u(t - \mu), \tag{2.21}$$

which includes both an initial phase where release rate ramps up after  $t = \mu$  and a decay phase where release rate falls off exponentially. Note that the area under the curve, and thus the probability of release, remains the same. For  $\sigma > 0$ , the final form of the release component looks like

$$\begin{aligned}
r(t) &= P \frac{k}{k\tau - 1} \left( e^{-\left(t - \left(\mu + \frac{\sigma^2}{2\tau}\right)\right)/\tau} \Phi\left(\frac{t - (\mu + \sigma^2/\tau)}{\sigma}\right) \right. \\
&\quad \left. - e^{-k\left(t - \left(\mu + \frac{\sigma^2}{2}k\right)\right)} \Phi\left(\frac{t - (\mu + \sigma^2 k)}{\sigma}\right) \right), \tag{2.22}
\end{aligned}$$

which basically just adds a little extra rightward temporal shift and smooths out the corner in the profile shape. Figure 2.13A-C shows how this filter affects the shape of a release profile component.

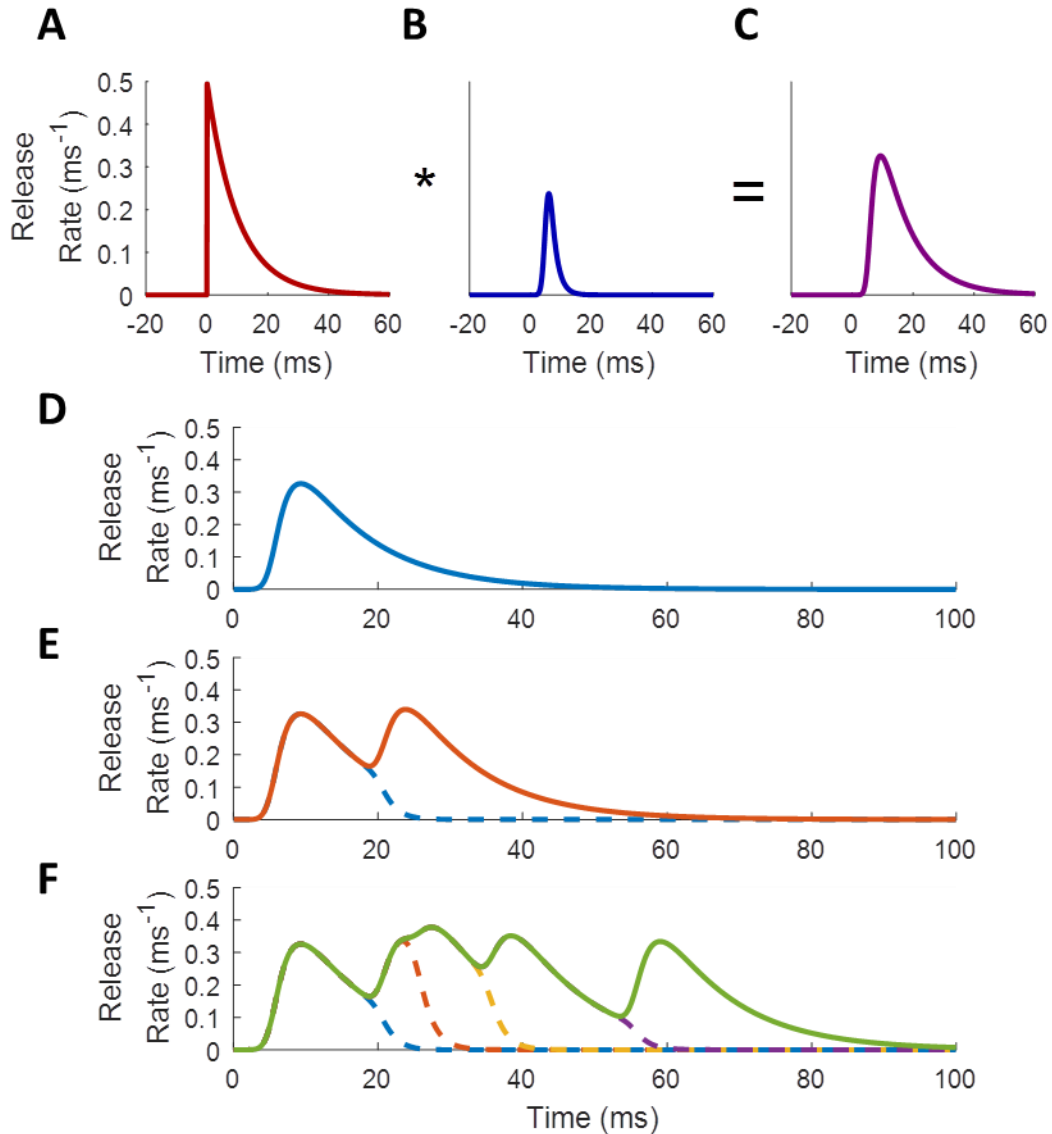


**Figure 2.13: Convolutional Filter Applied to a Component of a Release Rate Function.**

Toy model with  $P = 5$ ,  $\tau = 10$  ms,  $k = 0.5$  ms<sup>-1</sup>,  $\mu = 5$  ms, and  $\sigma = 1$  ms. (A) Unfiltered release rate component. (B) MCMC ex-Gaussian filter shape. (C) Filtered release profile produced by convolving the release rate profile with the temporal filter. (D) Release profile component in response to one spike, (E) two spikes, (F) and to multiple spikes. Dotted lines show how the histogram of response to one AP falls off with interference from the response to the following AP (see Equation 2.21). Spike times at 0, 15, 20, 30, and 50 ms.

When a second AP arrives at the release site, the VDCCs produce another influx of  $\text{Ca}^{2+}$  that can again propagate to the SNARE complex. The buffered diffusion again involves an ex-Gaussian-distributed delay, after which the release mechanism starts responding to the second spike, whose  $\text{Ca}^{2+}$  builds on the  $\text{Ca}^{2+}$  from the first. The probability  $D(t)$  that the  $\text{Ca}^{2+}$  sensor has begun responding to the  $\text{Ca}^{2+}$  from the latest AP (assumed to arrive at  $t = 0$ ) by initiating the release profile is simply the cumulative distribution of the temporal delay filter:

$$\begin{aligned} D(t) &= \int_{-\infty}^t a(t; k, \mu, \sigma) dt \\ &= \Phi\left(\frac{t - \mu}{\sigma}\right) - e^{-k\left(t - \left(\mu + \frac{\sigma^2}{2}k\right)\right)} \Phi\left(\frac{t - (\mu + \sigma^2 k)}{\sigma}\right). \end{aligned} \quad (2.23)$$

More intuitively, by letting  $\sigma \rightarrow 0$ , the Gaussian component becomes a delta function, and the first-release distribution function above becomes much more simply

$$D(t) = (1 - e^{-k(t-\mu)})u(t - \mu). \quad (2.24)$$

Thus, after the second spike, the histogram of releases from the first spike drops off exponentially, while those due to the second spike rise and fall as for the first spike. For two spike times,  $t_{s1} < t_{s2}$ , the net release profile that results is then

$$r(t; \{t_{s1}, t_{s2}\}) = r(t - t_{s1})(1 - D(t - t_{s2}))^{N_v} + r(t - t_{s2}), \quad (2.25)$$

where  $N_v$  is the number of vesicles awaiting  $\text{Ca}^{2+}$  to trigger release. In other words, the response to the first spike is cut short by  $D(\cdot)$  to give way to the response to the second spike. And every time another spike arrives, it decreases the probability of release relative to the first spike multiplicatively, such that

$$r(t; \mathbf{S}) = \sum_{t_{s1} \in \mathbf{S}} \left( r(t - t_{s1}) \prod_{\substack{t_{s2} \in \mathbf{S} \\ t_{s2} > t_{s1}}} (1 - D(t - t_{s2}))^{N_v} \right), \quad (2.26)$$

where  $\mathbf{S} = \{t_{s1}, t_{s2}, \dots\}$  is the set of all spike times. When  $\sigma$  is small relative to the median interspike interval, however, third spikes have an almost imperceptible effect at cutting the first profile short relative to the second spike's effect. Figure 2.13D-F shows what these profiles should look like for a certain set of parameters in response to various spike trains.

### 2.2.3.2 Release Profile Parameters

With the mathematical description of the release histograms in mind, I ran a fitting algorithm (see Methods 2.1.4) to determine the values of the parameters for each profile. Initially, I used release profiles driven by  $\text{Ca}^{2+}$  measured at 400 nm from the cluster of 100 VDCCs, which provides a physiologically realistic probability of release for a single vesicle (around 0.04) (Kandaswamy et al., 2010). The synchronous release mechanism exhibits more exponential decay components in its release rate histogram than does the asynchronous mechanism (4 versus 3), likely because it has more  $\text{Ca}^{2+}$  binding sites (5 versus 2) and because it operates on a faster time scale.

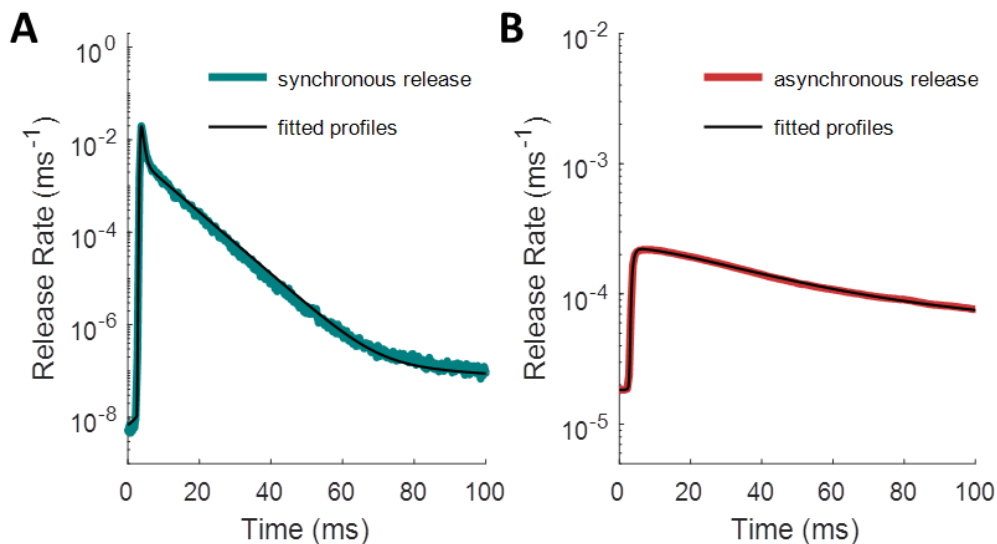


**Figure 2.14: Fitted Release Rate Histogram Profile Parameters.**

Parameter values given in Table 2.3. (A) Synchronous release rate: true histogram (black) with estimated histogram (green). (B) Asynchronous release rate: true histogram (black) with estimated histogram (dark red).

**Table 2.3: Spike-Evoked Release Rate Parameters.**

Parameter values calculated for a single spike following a period of low activity. Valid for  $\text{Ca}^{2+}$ -sensitive synchronous and asynchronous release mechanisms located 400 nm from a cluster of 100 VDCCs.

component	$P$	$\tau$	$k$	$\mu$	$\sigma$
$S_1$	0.0175	0.163 ms	$1.79 \text{ ms}^{-1}$	3.41 ms	0.168 ms
$S_2$	0.0220	6.50 ms	$18.0 \text{ ms}^{-1}$	3.56 ms	0.0977 ms
$S_3$	$1.70 \times 10^{-5}$	80.0 ms	$0.526 \text{ ms}^{-1}$	10.0 ms	4.44 ms
$S_4$	$1.10 \times 10^{-5}$	1000 ms	$0.142 \text{ ms}^{-1}$	50.0 ms	11.5 ms
$A_1$	$3.72 \times 10^{-3}$	17.7 ms	$1.60 \text{ ms}^{-1}$	3.05 ms	0.243 ms
$A_2$	0.0111	76.9 ms	$0.0759 \text{ ms}^{-1}$	4.00 ms	1.14 ms
$A_3$	0.0136	1000 ms	$0.0337 \text{ ms}^{-1}$	76.5 ms	21.9 ms

Keep in mind that the  $\mu$  values are somewhat arbitrary in that they depend on exactly when during the AP that the spike time is taken to occur. Action potential waveforms last a couple of milliseconds (see Figure 2.5 in Results 2.2.1) (Bischofberger et al., 2002); the values for  $\mu$  above used a point on the AP waveform before the rising phase as the spike time. Using the peak of the AP would take away about 2 ms from all values of  $\mu$ . Again, the time point along the AP where the spike is counted is arbitrary, but it must be consistent across all components.

#### **2.2.4 Distance-Dependence of Ca<sup>2+</sup> Sensor**

One would expect the strength of spike-evoked neurotransmitter release to diminish with increasing distance from the Ca<sup>2+</sup> source, where Ca<sup>2+</sup> has more time to diffuse and bind to buffer molecules before reaching the sensor. In fact, numerous studies have found that vesicles of the readily releasable pool (RRP) fall into one of two subpopulations, depending on their physical location of vesicles within the synapse: vesicles located very near Ca<sup>2+</sup> channels release quickly in response to spikes, while those farther away are more reluctant (J. S. Lee, Ho, & Lee, 2012; J. S. Lee et al., 2013; Moulder & Mennerick, 2005; Sakaba & Neher, 2001). To explore how the release rate profiles vary with distance, we established a linear array of Ca<sup>2+</sup> sensors along the length of the model axon, with a cluster of 50 VDCCs arranged in a half-disk at one end (Figure 2.15A). Reflective boundaries on the ends of a 2- $\mu$ m tube effectively simulated the effects of having one cluster of 100 VDCCs every 4  $\mu$ m, consistent with previous models of the Schaffer collateral axon (Nadkarni et al., 2010). Running the model again for 2000 trials, with a single action potential stimulus applied at the beginning, we obtained Ca<sup>2+</sup> traces measured at each point along the axon. For the first 1.4  $\mu$ m, free Ca<sup>2+</sup> from the initial influx dominated, and the peak concentration declined exponentially with distance

(length constant  $0.204 \mu\text{m}$ ; Figure 2.15C). Farther out, global accumulation and depletion of  $\text{Ca}^{2+}$  dominates, which, although spike-evoked, does not vary in magnitude with distance and acts over a much longer time scale and at a much lower level than most of the AP-triggered  $\text{Ca}^{2+}$ .

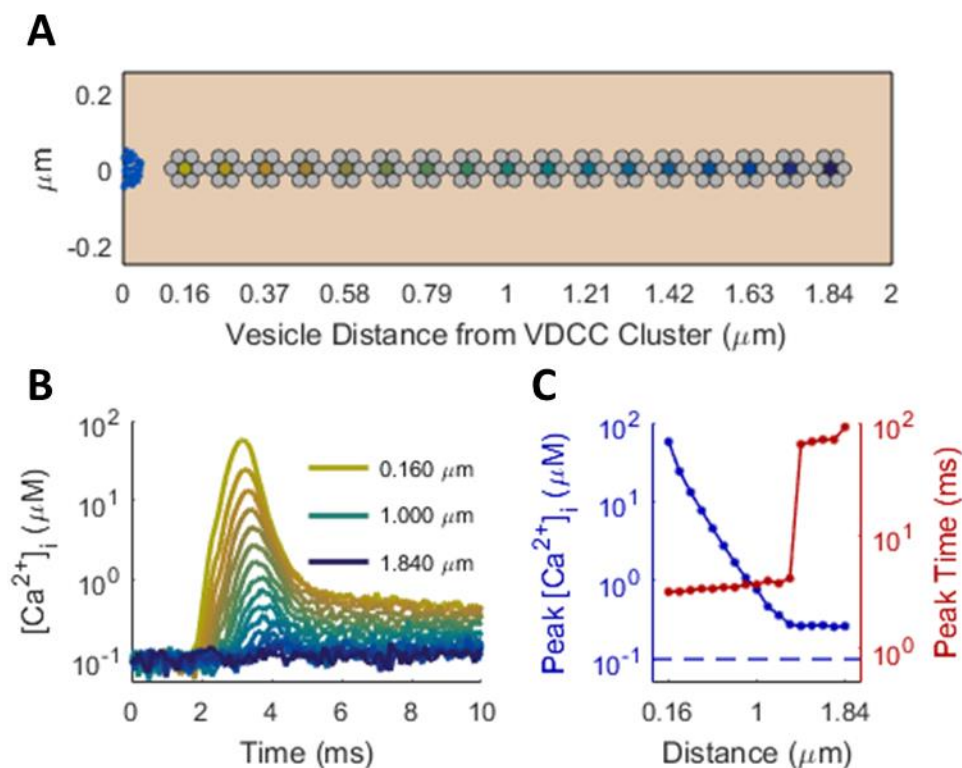


**Figure 2.15: Peak  $[\text{Ca}^{2+}]_i$  Drops Off Exponentially with Distance from VDCC Cluster.**

(A)  $\text{Ca}^{2+}$  sensors (dark yellow through dark blue filled circles) at vesicle cluster centers, displaced linearly from cluster of  $\text{Ca}^{2+}$  channels (blue half-disk on the left); distance in  $\mu\text{m}$ ,  $d_n = 0.160 + 0.105n$  for  $n \in \{0, \dots, 16\}$ . (B) Profiles of  $[\text{Ca}^{2+}]_i$  averaged from 2000 trials of MCell simulations with  $\Delta t = 0.1$  ms; color corresponds to distance from VDCC cluster (yellow proximal to blue distal). (C) Logarithmic plots of peak  $[\text{Ca}^{2+}]_i$  (blue) and peak time (red) as a function of distance from  $\text{Ca}^{2+}$  source; latent  $\text{Ca}^{2+}$  component dominates over the initial action-potential-evoked influx after  $1.4 \mu\text{m}$ .

Running these simulations in MCell, rather than as a much simpler well-mixed model, was essential for capturing both distance-dependent effects and temporal features of the  $\text{Ca}^{2+}$  waveform. The well-mixed assumption, which ignores diffusion and treats all chemical processes as occurring at the same point in space, does not hold at the spatial and temporal scales of interest in the synapse (K. M. Franks & Sejnowski, 2002; Warren, Mackay, Webster, & Arnot, 2009). As seen in Figure 2.15C, peak  $\text{Ca}^{2+}$  drops precipitously even over fractions of a micron away from the VDCC cluster, and the shape of the response changes dramatically over this same scale, transitioning from a predominantly synchronous to a predominantly asynchronous profile, even before the  $\text{Ca}^{2+}$  sensors start responding. These trends, elucidated by the spatial MCell model, are completely absent in the space-less well-mixed simulation (Figure 2.16A), even when all other aspects of the model remain the same, such as the number of VDCCs, calbindin buffer molecules, and PMCA pumps and the set of all state transitions for each molecular species (see Methods 2.1.1.1 for details). Note also from Figure 2.16A that the transition in time from the fast synchronous component to the extended asynchronous component is much sharper in the case without space. The extra  $\text{Ca}^{2+}$  decay component arises from local saturation effects. After the initial rapid influx, the calbindin buffer immediately around the VDCC cluster becomes saturated, causing the high free  $\text{Ca}^{2+}$  that remains to overwhelm the PMCA pumps' ability to evacuate it from the area. The pumps remove it at a constant maximum rate, leading to a short linear decay only evident very near the VDCCs (yellow traces, Figure 2.16A) or when all calbindin is removed from the simulation (Figure 2.16B). Such effects do not appear in the well-mixed case because all buffer molecules and pumps are simultaneously available to all the free  $\text{Ca}^{2+}$ , preventing any local saturation from occurring. Thus, in

light of all these effects, the spatial MCell model is crucial for the task of properly characterizing the  $\text{Ca}^{2+}$  transient in the synapse.

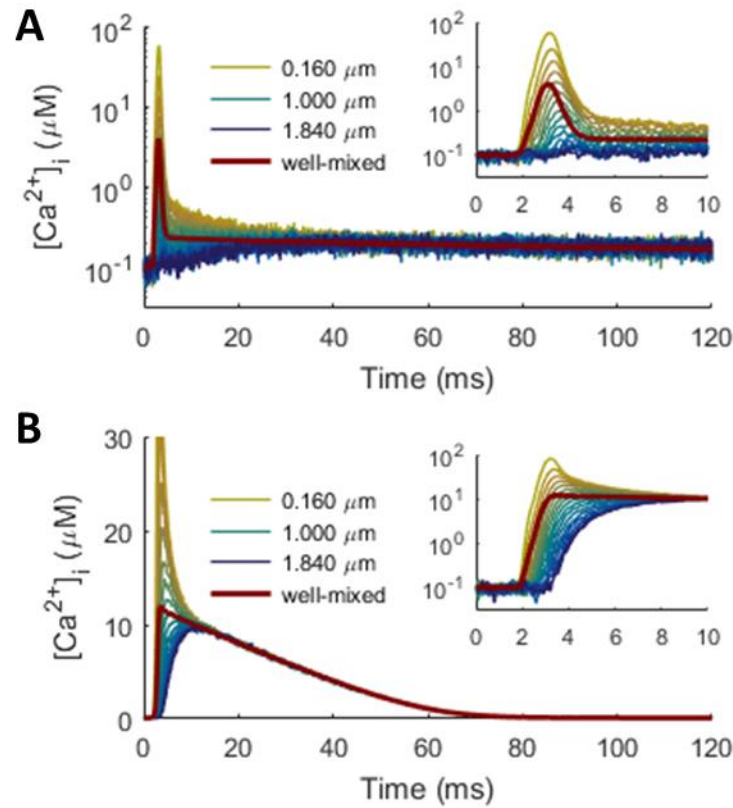


**Figure 2.16: Spatial Modeling Important for Capturing Fine-Grain Features of  $\text{Ca}^{2+}$  Transients.**

$[\text{Ca}^{2+}]_i$  measured over time in MCell (colored) and in the deterministic well-mixed model (maroon). Color transitions from yellow for vesicles proximal to the VDCC  $\text{Ca}^{2+}$  source to blue for vesicles far away (see Figure 2.15). Proximally (distally) measured  $[\text{Ca}^{2+}]_i$  displays more (fewer) components of decay than are evident in the deterministic model.

After obtaining the distance-dependent  $\text{Ca}^{2+}$  traces, we could use them to see how the rate of release changes with distance. Using the above-measured  $\text{Ca}^{2+}$  traces as input to the deterministic Markov model of Syt-1/7, we once again calculated the instantaneous rates of spike-evoked release for single vesicles at increasing distances. As expected, the single-vesicle probability of release decays with distance until it reaches a distance-independent baseline level (Figure 2.17), although this occurs differently for the synchronous and asynchronous mechanisms.

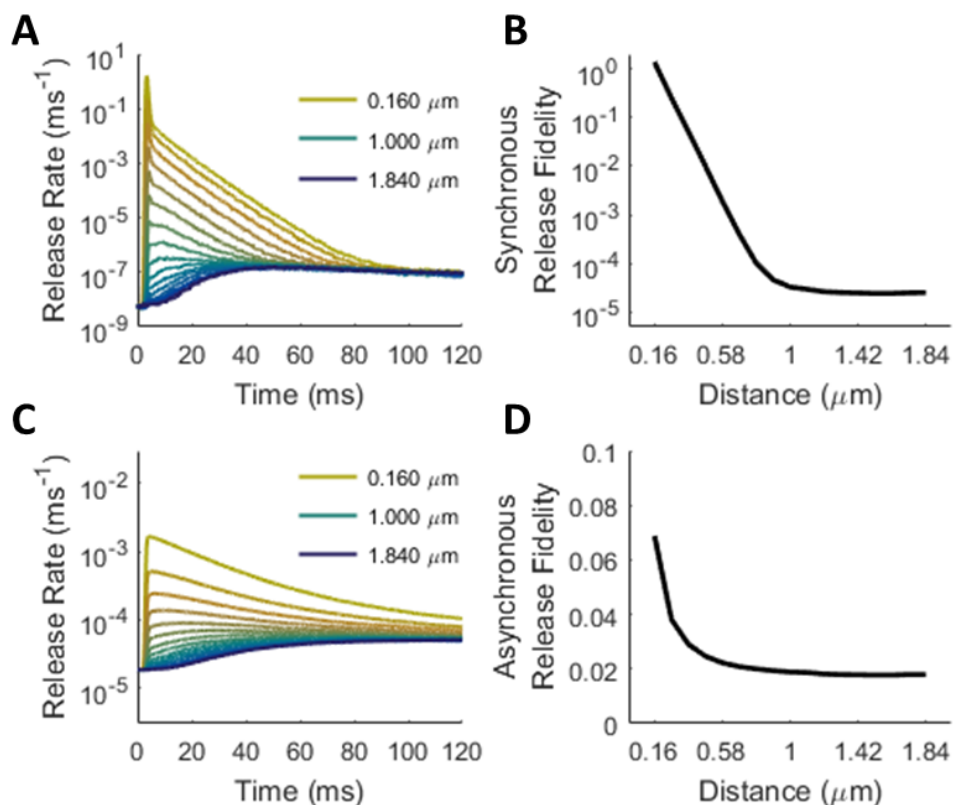


**Figure 2.17: Synchronous and Asynchronous Release Rates Decrease with Distance from the  $\text{Ca}^{2+}$  Source.**

Color scheme identical to that used in Figure 2.15: yellow to blue represent proximal to distal  $\text{Ca}^{2+}$  sensors. (A) Synchronous release rate. (B) Integrated probability of synchronous release falls off nearly exponentially with distance to a baseline level. (C) Asynchronous release rates. (D) Integrated probability of asynchronous release also decays with distance to some baseline, but not exponentially.

To account for the change in release profiles mathematically, I ran a fitting algorithm (see Methods 2.1.4) on each profile, exploring the space of values both for the magnitude of each component of release ( $P_j$  in Equations 2.17, 2.18) and for the temporal filter parameters ( $k_j$ ,  $\mu_j$ , and  $\sigma_j$  in Equations 2.18-2.23). I assumed that the time constants of release rate decay ( $\tau_j$ ) remained the same for the release histograms at all distances and that any changes in the size or shape in the histograms are due to depleted levels of  $[Ca^{2+}]_i$  and to increasing delays for  $Ca^{2+}$  ions to reach the sensors. Accordingly, I expected to see the  $P_j$  values decay with distance as  $Ca^{2+}$  is dissipated, sequestered, and removed; the  $k_j$  values to slow down as the limiting delay grows with distance; and the values of  $\mu_j$  and  $\sigma_j$  to increase somewhat due to greater numbers of potential interactions before the  $Ca^{2+}$  ions complete their traversal. The fitting algorithm produced sets of parameters at each location in the synapse that generally followed these trends (Figure 2.18C,D), although the noise in the data and the very high dimensionality of the problem prevented smooth trends from being ascertained.

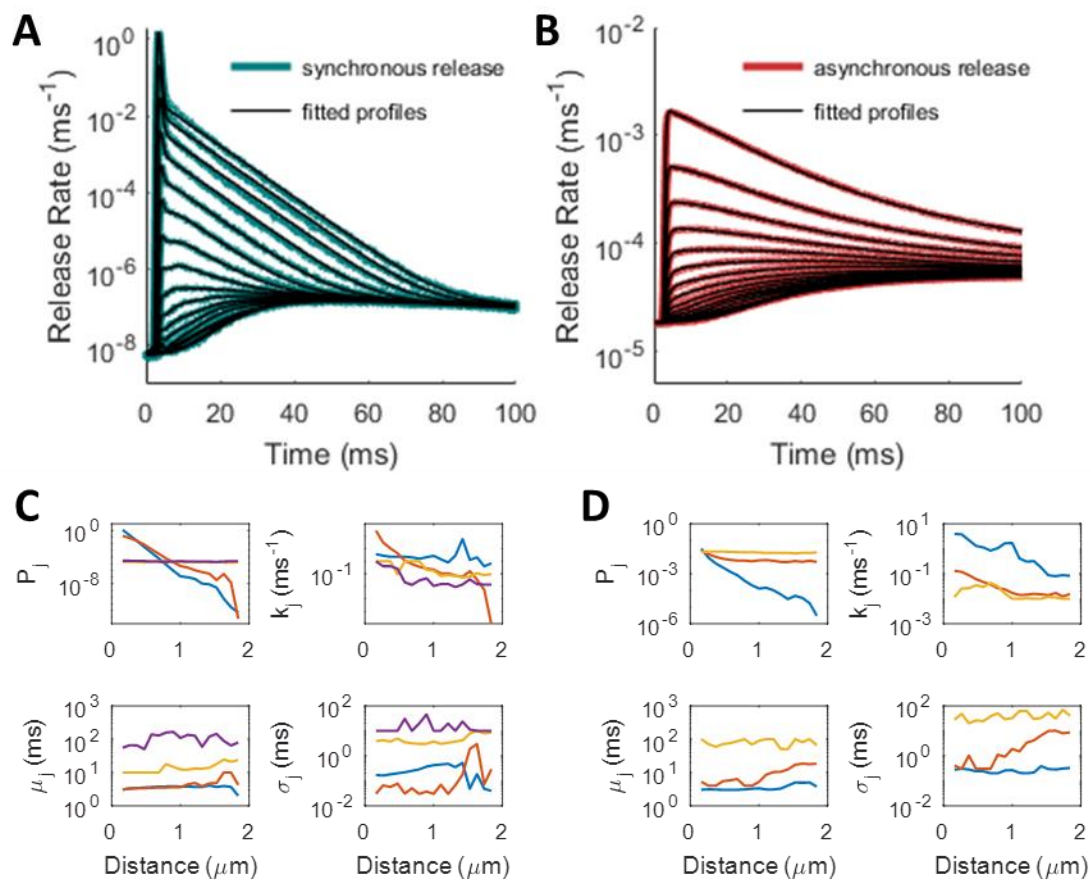


**Figure 2.18: Parametric Fits to Release Histogram Profiles at Increasing Distance from the  $\text{Ca}^{2+}$  Source.**

(A-B) Fitted release profiles (black) imposed over the true histograms for synchronous (A, blue) and asynchronous (B, red). (C) Parameter values as a function of distance for synchronous release. (D) The same for asynchronous release.

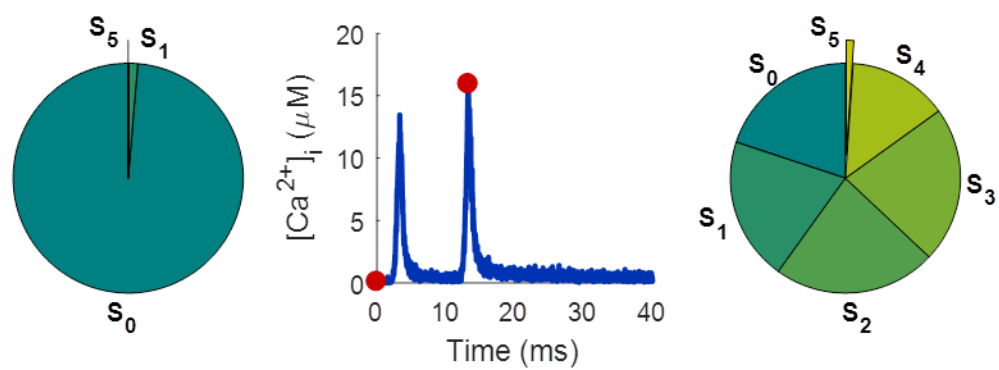
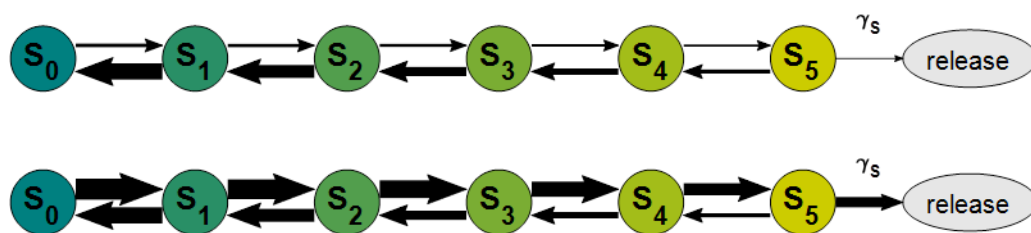
### 2.2.5 Facilitation in Release Probability

The discussion above has focused the release response of a single vesicle to a single action potential (AP). However, many synapses display a facilitation in release probability from one AP to another (Neher & Sakaba, 2008; Rosahl et al., 1993; Stevens & Wang, 1995; Thomson & Bannister, 1999; M. Tsodyks et al., 1998; Varela et al., 1997; Zucker & Regehr, 2002). This results both from an accumulation of  $\text{Ca}^{2+}$  in the presynaptic space (Neher & Sakaba, 2008) and from a stochastic accumulation of  $\text{Ca}^{2+}$  on the synaptotagmin sensor of the SNARE complex. In fact, simulations with this model suggest that nonlinear binding cooperativity in the calcium-sensitive synaptotagmins induces interspike facilitation even in lieu of cytoplasmic calcium buildup (data not shown). This happens because on some trials,  $\text{Ca}^{2+}$  accumulates on the sensor, not enough to trigger vesicle fusion on the first spike, but enough to increase the probability of reaching the releasable state after subsequent spikes. As can be seen in Figure 2.19,  $\text{Ca}^{2+}$  entry from one AP can predispose the distribution of bound states of the sensor to trigger release with greater alacrity on subsequent APs.

**Figure 2.19: Change in the Balance of Binding Kinetics and Internal State Distribution of  $\text{Ca}^{2+}$  Sensor with Spike History.**

State diagrams the same as shown in Figure 2.4 in Methods 2.1.1.3. (A) Synchronous state diagrams. At baseline  $[\text{Ca}^{2+}]_i$  (first red dot), unbinding kinetics (left arrows) overpower binding (right arrows), biasing Syt-1 toward unbound state ( $S_0$ ; top diagram), with almost no probability of having any  $\text{Ca}^{2+}$  ions bound before an AP (left pie chart). During peak  $\text{Ca}^{2+}$  influx (second red dot), binding rates (thicker right arrows) overpower unbinding, biasing Syt-1 toward its fully-bound releasable state ( $S_5$ ; lower diagram), with much greater probability of having at least some  $\text{Ca}^{2+}$  bound (right pie chart). (B) The same for asynchronous release with Syt-7, whose releasable state requires two  $\text{Ca}^{2+}$  ions bound ( $A_2$ ). Slower kinetics lead to only slight bias in favor of binding during an AP (slightly thicker right arrows in lower diagram), leading to miniscule increase in probability of being in the releasable state on later spikes (right pie chart). Release becomes more probable on subsequent spikes because previous activity has pushed synaptotagmin into higher-bound states, making reaching the releasable state easier.

A



B

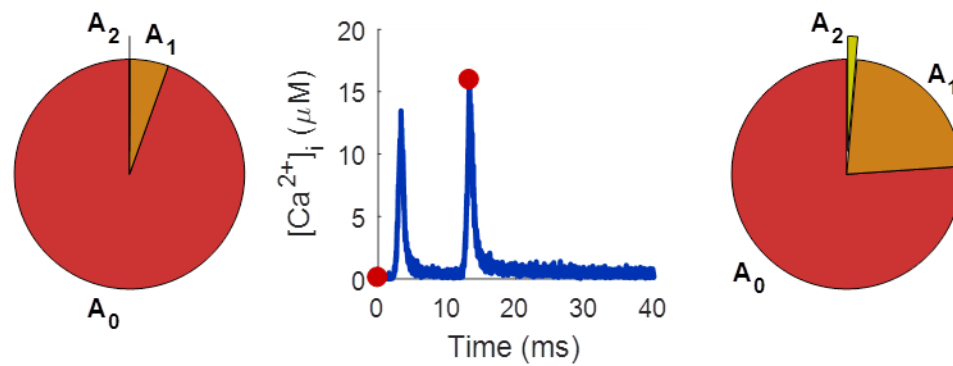
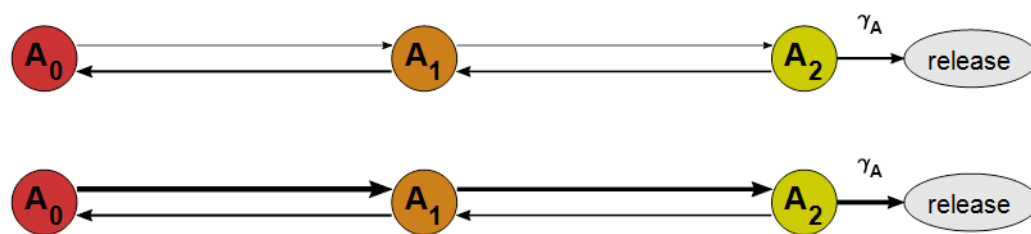
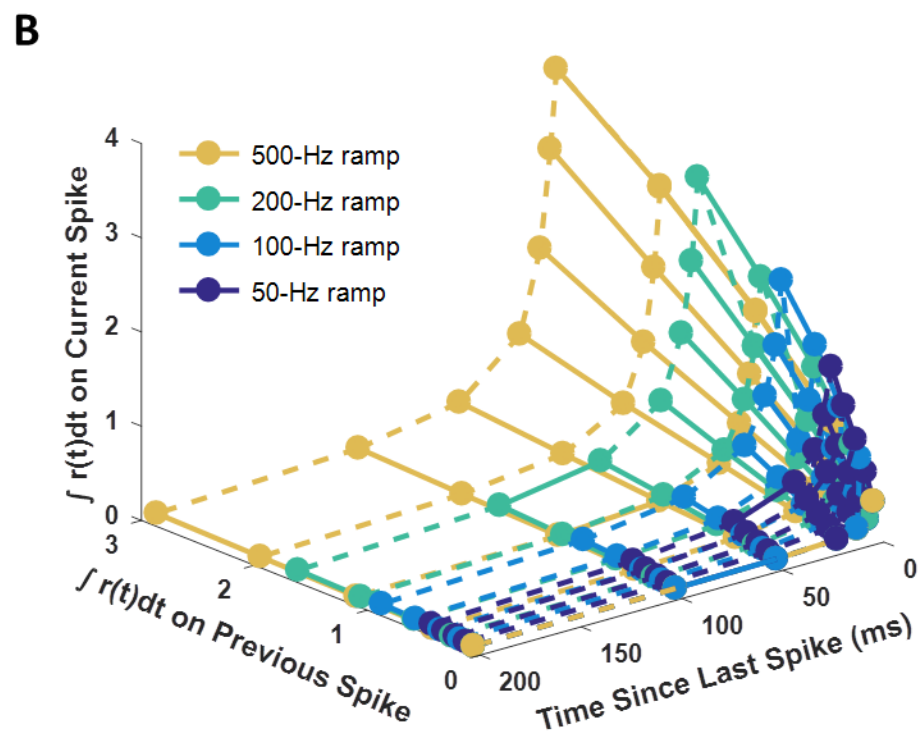
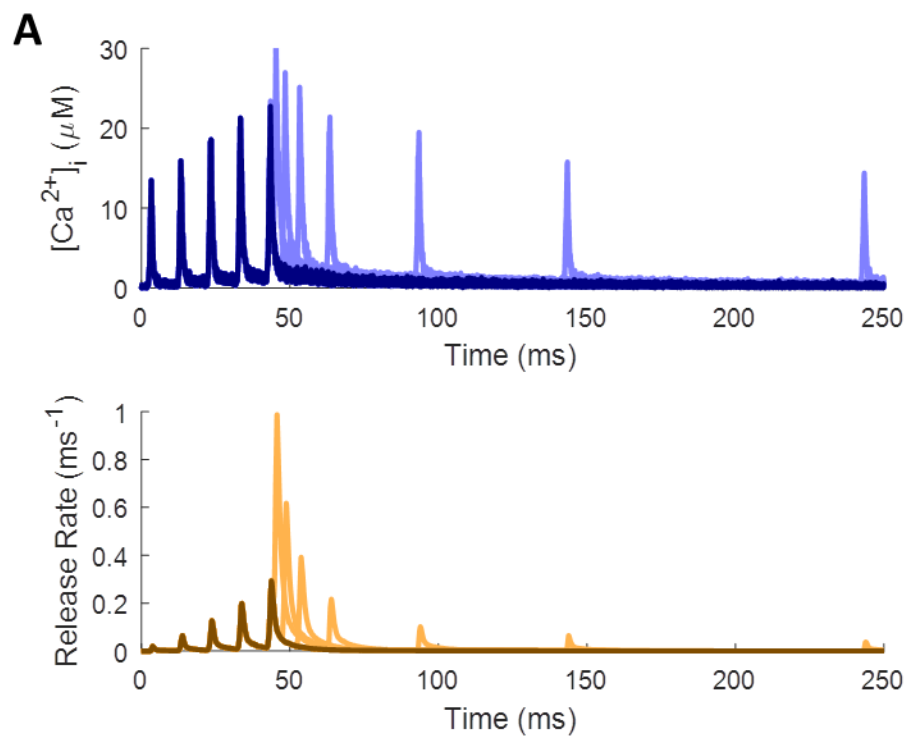


Figure 2.20A shows how the combined release rate from synchronous and asynchronous release mechanisms (brown/gold) grows far more quickly than does spike-evoked  $[Ca^{2+}]_i$  (black/gray). Thus, the magnitude of facilitation may be nonlinear due to the internal binding kinetics of the synaptotagmin (see Methods 2.1.1.3). Furthermore, the level of facilitation depends to some extent on the full history of spiking activity in the synapse. In the simplest case, the probability of release on one spike should depend only on the probability for the previous spike and the time since the previous spike. Indeed, as Figure 2.20B shows, the integrated rate of release  $r(t)$  increases from one AP to the next for short interspike intervals (ISIs) and decays back toward baseline for longer ISIs. However, the level of facilitation is not a simple function of the most recent activity but depends on the rate of stimulation prior to the last spike.

To explore the space of facilitation dynamics as fully as possible, we applied spike trains with spike ramps of different rates and durations, to see how quickly facilitation builds up, followed by single probe spikes at increasing ISI, to see how quickly it decays back to baseline (see Methods 2.1.3). Figure 2.20B explores the history-dependence of the facilitation function that this stimulus protocol reveals. For examples of how these different spike trains affect the rates of synchronous and asynchronous release, see Figure 2.21.

**Figure 2.20: Empirical Facilitation in Release Probability is a Nonlinear Function of Spike History and  $\text{Ca}^{2+}$  Buildup.**

(A)  $[\text{Ca}^{2+}]_i$  and release rate in response to a 5-spike ramp stimulus with a 10-ms ISI (black and brown), followed by a single probe spike at increasing delay from the end of the ramp (gray and gold; multiple cases overlaid on the same plot). Release rate grows much faster than  $\text{Ca}^{2+}$  buildup can account for. (B) Integrated release rate (related to release probability) for a given spike as a function of integrated release from the previous spike and of delay between spikes. Different colors distinguish facilitation functions with different spike histories



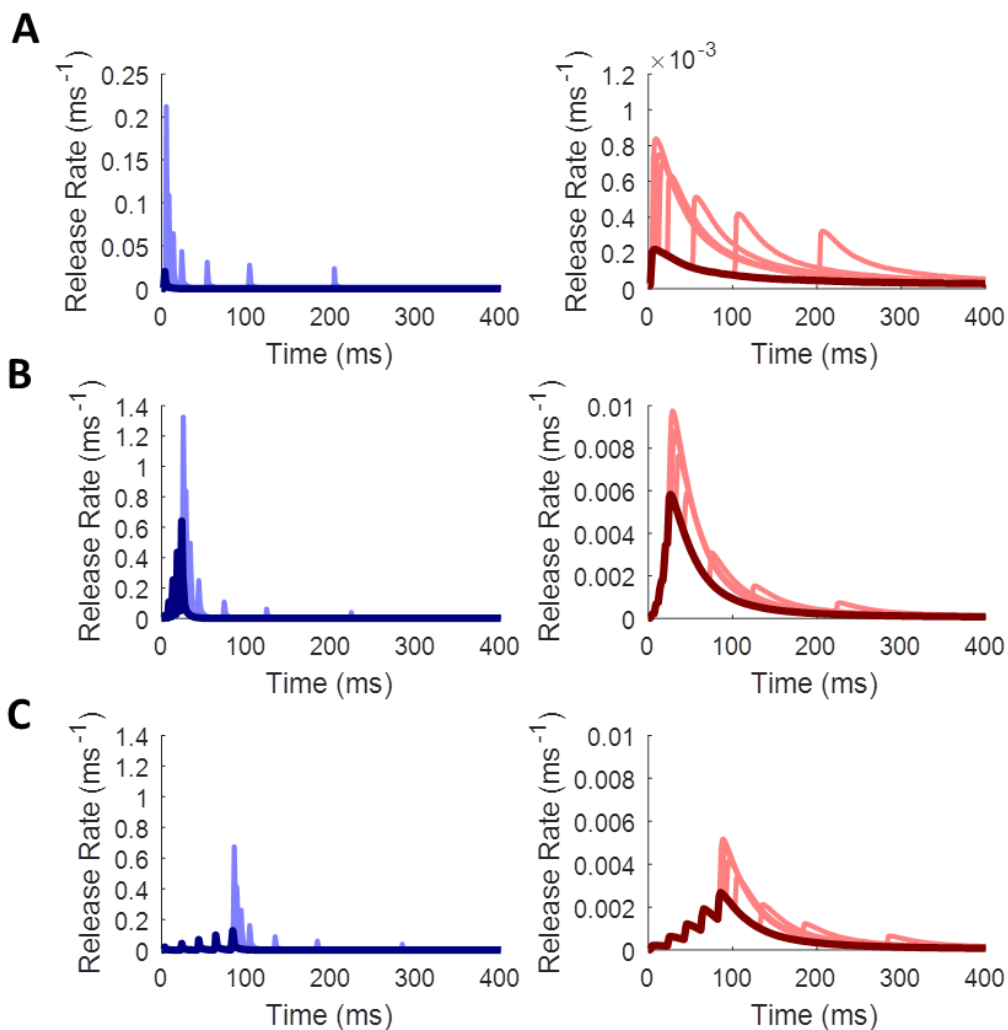


**Figure 2.21: Empirical Facilitation in Synchronous and Asynchronous Release Rates.**

Synchronous release rate shown in blue; asynchronous shown in red. Dark colors represent initial spike ramp (common to all traces on a plot); light colors represent single probe spikes from different simulations. Associated  $\text{Ca}^{2+}$  traces omitted for clarity. (A) PPF decays with increasing ISI. (B) 5-spike ramp with a 5-ms ISI shows strong facilitation. (C) 5-spike ramp with a 20-ms ISI shows weaker facilitation.

### 2.2.5.1 Functional Model of Facilitation

Facilitation results from a complex interplay of  $\text{Ca}^{2+}$  association and dissociation rates, where the stochastic accumulation of  $\text{Ca}^{2+}$  on the synaptotagmin from one AP to the next leads to an increase in the probability of neurotransmitter release. However, this increased alacrity does not affect all components of release equally. Therefore, I derived a general facilitation function  $F_j(\cdot)$  that affects each component  $j$  independently. The area under the curve of each component of the release histogram (see Equations 2.17, 2.18) depends on the facilitation factor according to

$$P_j(n) = P_{j0} \cdot F_j(n), \quad (2.27)$$

where  $P_{j0}$  is the baseline value and  $n$  is the index of the current spike. To ensure that the function works for arbitrary spike trains, the factor  $F_j(n)$  needs both to grow somehow from spike to spike and to decay back toward one for large ISIs. This growth can happen in a highly nonlinear fashion, so to account for this, I take  $F_j(n)$  to be a nonlinear combination of linear facilitation factors  $f_{jk}(n)$  such that

$$F_j(n) = \prod_{k=1}^{M_j} f_{jk}(n)^{\xi_{jk}}, \quad (2.28)$$

where  $M_{jk}$  represents the number of facilitation components (either one or two for all functions explored below), and  $\xi_{jk}$  represents the nonlinearity applied to facilitation component  $k$  of release component  $j$ . Each  $f_{jk}(n)$  accounts for some aspect of the internal state of the SNARE complex, in terms of how the expected number of  $\text{Ca}^{2+}$  ions bound changes with time, that helps determine the probability of release on subsequent APs.

In the simplest case, each  $f_{jk}(n)$  would result from a simple convolution of spike times with an exponential decay function:

$$f_{jk}(t) = \left( e^{-t/\tau_{jk}} u(t) \right) * \left( \sum_{t_s \in \mathbf{S}} \delta(t - t_s) \right). \quad (2.29)$$

Here,  $u(t)$  is again the Heaviside step function,  $\tau_{jk}$  is the time constant for decay of  $f_{jk}$ , and  $\mathbf{S}$  is the set of all spike times;  $f_{jk}(n)$  would then be the value of  $f_{jk}(t)$  sampled at the time of the  $n$ -th AP. This is equivalent to having the value of  $f_{jk}(n)$  decay exponentially from one spike to the next before incrementing by one:

$$f_{jk}(n) = 1 + f_{jk}(n-1)e^{-\Delta t/\tau_{jk}}, \quad (2.30)$$

where  $\Delta t$  is the delay from the previous AP to the current one. The increment of one is meant to account for the influx of about the same amount of  $\text{Ca}^{2+}$  during each AP. This formulation ensures that even after infinitely long intervals, the facilitation factor will equal a value no less than  $F_j(0) = 1$ , allowing the release components to return to their baseline values of  $P_j = P_{j,0}$  during periods of inactivity, as expected.

However, this formula implies that for an infinitely fast rate of stimulation,  $f_{jk}(n)$  could grow toward infinity, producing an infinitely fast rate of release, all of which are impossible. More realistically, there should exist some finite saturation level  $L_{jk}$ , such that the facilitation function could never theoretically exceed

$$F_j(\infty) = \prod_{k=1}^{M_j} L_{jk}. \quad (2.31)$$

When facilitation is still well below this level, it should continue to increment by approximately one on every spike, but this increment should fall to zero quickly enough that facilitation never exceeds saturation. Setting a maximum number of equal-sized steps to saturation for each component,  $N_{jk}$ , the value of  $f_{jk}(n)$  becomes

$$g_{jk}(n) = f_{jk}(n-1)e^{-\Delta t/\tau_{jk}},$$

$$f_{jk}(n) = 1 + g_{jk}(n) - \left( \frac{g_{jk}(n)}{N_{jk}} \right)^{N_{jk}}, \quad (2.32)$$

where  $g_{jk}(n)$  represents the amount of the facilitation parameter “left over” from the previous spike. The term subtracted off at the end ensures that  $f_{jk}(n)$  never exceeds  $N_{jk}$ , just as  $\text{Ca}^{2+}$  cannot accumulate to infinite concentrations but is limited by the electrochemical gradient across the cell membrane (Simons, 1988). An alternative would be simply to set  $f_{jk}(n) = N_{jk}$  whenever a step size of one would cause it to exceed this limit, but the formula in Equation 2.32 allows for a smoother approach. Figure 2.22A shows how different values for  $N$  (subscripts removed for convenience) cause the otherwise linear step sizes to saturate at different levels. Importantly,  $N \geq 1$  to ensure stable growth. Figure 2.22B shows how spike frequency also plays a role in determining the steady-state level of facilitation.

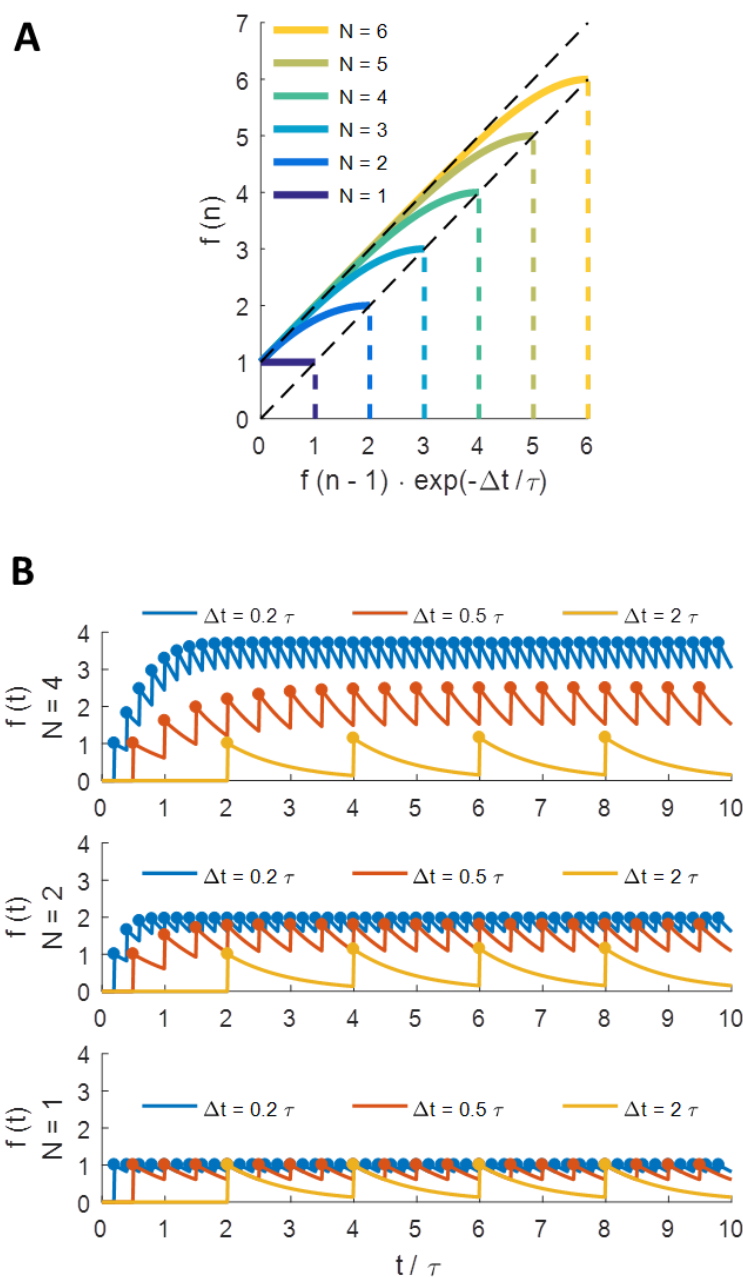


**Figure 2.22: Saturation of Facilitation Parameters.**

(A) Facilitation parameter  $f(\cdot)$  increases almost linearly from one spike ( $f(n-1)$ ) to the next ( $f(n)$ ), until it approaches some limit  $N \geq 1$ . (B) Curves represent the unseen change in  $f(\cdot)$  between APs. Dots represent actual values observed at spike times, values determined by the  $\text{Ca}^{2+}$ -triggered increment in release fidelity at each AP. Steady-state value for facilitation parameter limited by stimulus frequency and by value of  $N$ . No facilitation above baseline occurs for  $N = 1$ .

To gain a better intuition of this function, consider the case with a single component,

$$F(n) = f(n)^\xi, \quad (2.33)$$

where the subscripts have been removed for simplicity. In cases with a constant frequency of stimulation,  $\alpha := \Delta t^{-1}$ , the steady-state value for the facilitation component,  $f(\infty)$ , can be solved analytically by setting  $f(n) = f(n+1)$  and solving with Equation 2.32 to yield

$$\left(N^{-N} \exp\left(-\frac{N}{\alpha\tau}\right)\right) f(\infty)^N + \left(1 - \exp\left(-\frac{\Delta t}{\tau}\right)\right) f(\infty) - 1 = 0. \quad (2.34)$$

In the limit as  $N \rightarrow \infty$ , or at least for low enough stimulation frequencies that the intermediate variable  $g(n) = g(n+1) = f(n) \exp(-\Delta t/\tau) \ll N$  for all  $n$ ,

$$f(\infty) = \left(1 - \exp\left(-\frac{\Delta t}{\tau}\right)\right)^{-1} \Rightarrow F(\infty) = \left(1 - \exp\left(-\frac{\Delta t}{\tau}\right)\right)^{-\xi}. \quad (2.35)$$

Thus, there is a finite limit to facilitation even without the saturation parameter  $N$ . However, as stimulus frequency increases, saturation becomes more apparent, and in the limit of (unphysiologically) high stimulus frequency ( $\alpha \rightarrow \infty$  or  $\Delta t \rightarrow 0$ ),

$$f(n|n \ll N) = n \Rightarrow F(n|n \ll N) = n^\xi \quad (2.36)$$

$$f(\infty) = N \Rightarrow F(\infty) = N^\xi = L. \quad (2.37)$$

In other words, the function facilitates linearly for the first several spikes (for large enough  $N$ ) and then plateaus to some maximum value. For large enough  $N$  and  $\xi = 1$ , this set of functions acts as a simple convolution of an exponential with the spike times, as in Equation 2.29, so long as the  $\tau$  of facilitation decay exactly matches the  $\tau$  of release rate decay; this kind of linearity, however, is not observed in the release profile considered here. Although we have considered facilitation always to be positive, this model provides the flexibility to allow negative facilitation: for  $\xi > 0$ ,  $F(\infty) > 1$ , giving

positive facilitation as normal; for  $\xi < 0$ ,  $F(\infty) < 1$ , producing depression in the parameter; for  $\xi = 0$ ,  $F(\infty) = 1$ , and no change can occur in the release-rate parameter. Such negative facilitation, although not observed in the magnitude of release rate for the Syt-1/7 mechanisms studied here, could apply in other circumstances to other parameters like time constants or rates that decrease with activity. For instance, short-term depression induced by  $\text{Ca}^{2+}$ -triggered inactivation of  $\text{Ca}^{2+}$  channels (Ben-Johny & Yue, 2014; Catterall, Leal, & Nanou, 2013; A. Lee et al., 2002; Nanou et al., 2016) could be represented as second or third component of the facilitation function that has a negative value for  $\xi_{jk}$ . However, this feature was not included in the MCell model so is beyond the scope of the current dissertation.

### 2.2.5.2 Fitting Facilitation to Complex Spike Trains

With the model for facilitation well established, I sought to fit it to the empirical changes observed in release rate for complex spike trains. For simplicity, I took facilitation to apply only to the  $P_j$  parameters, which control for the magnitude of each release component, although in principle the parameters of the temporal filter ( $k_j$ ,  $\mu_j$ , and  $\sigma_j$ ) might also increase ( $\xi > 0$ ) or decrease ( $\xi < 0$ ) with spike history. As discussed in Methods 2.1.3, I explored 136 unique spike trains and how both spike rate (along the spike ramp) and ISI (of the probe spike) affect the release rate in response to the last AP. Synaptic fidelity in each of these cases has been measured in Figure 2.20B, and the stimulus response profiles are displayed in Figure 2.21.

For the fitting algorithm, we used a simplex method for gradient descent, since the derivatives of the error function are difficult to compute (see Methods 2.1.4). The values of the  $P_j$  parameters were allowed to vary within bounds, while the profile time constants and the temporal filter parameters were held constant. The best-fit set of

values for  $P_j$  were found for the AP-response profile at the end of each spike train, after which the meta-parameters of the facilitation functions could be fitted to the patterns in  $P_j$  (see Figure 2.23B). Through trial-and-error, I found that the two components of synchronous release with the fastest time constants, along with the fastest component of asynchronous release, each required two facilitation components to explain their patterns of change from case to case. The synchronous and asynchronous release components with “medium” time constants (each close to 80 ms) could each be fitted with a single facilitation component. The slowest release components, with time constants of 1000 ms due to latent  $[Ca^{2+}]_i$  released from the buffer (see Figure 2.11 in Results 2.2.2), were constrained not to facilitate, since changes in these components seemed to have a negligible effect on fitting error. Table 2.4 records the facilitation meta-parameters obtained from the fits, along with the baseline values for release fidelity for each component ( $P_0$ ). During each step of the fitting algorithm, these metaparameters were used to generate predictions for the state of facilitation across all 136 spike-train cases, and error was calculated as the fraction of the variance of the “true” release fidelity values unexplained by the predicted pattern (Figure 2.23C; see Methods 2.1.4).

**Figure 2.23: Release Rate Parameters and Facilitation Metaparameters Fitted to Empirical Histogram Profiles.**

(A) Synchronous and asynchronous profiles fitted for baseline (un-facilitated) case, (B) and for highly facilitated case (probe spike 5 ms after 5-spike ramp of 5-ms ISIs). (C) Release fidelity values fitted case-by-case (dark colors) overlaid with predictions from best-fit facilitation functions (light colors). (D) Errors across all cases in linear and logarithmic space for the predictive model.

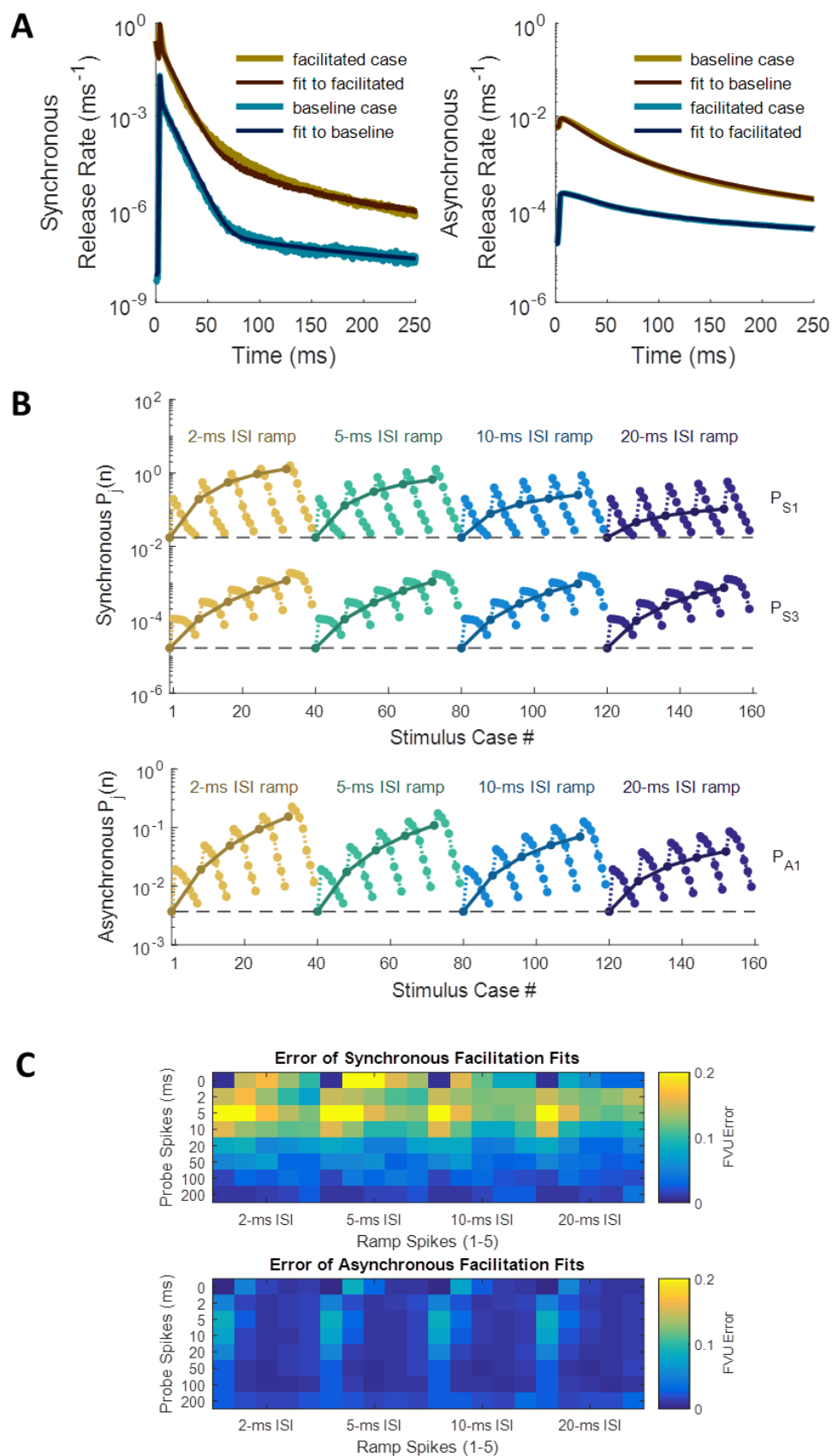


**Table 2.4: Metaparameters for Facilitation of Release Fidelity.**

First column shows baseline magnitudes of integrated release rate, duplicated from Table 2.3. First and second components of synchronous release and first component of asynchronous release facilitate with two time constants each. Smallest component of both release mechanisms does not facilitate.  $P_0$  is integrated release rate for the un-facilitated case (baseline),  $\tau$  is the time constant of decay for each facilitation component,  $N$  is the number of linear facilitation steps to saturation,  $\xi$  is the nonlinearity parameter, and  $L$  is the maximum facilitation factor contributed by each component. Valid for  $\text{Ca}^{2+}$ -sensitive synchronous and asynchronous release mechanisms located 400 nm from a cluster of 100 VDCCs.

component	$P_0$	$\tau$	$N$	$\xi$	$L = N^\xi$
$S_{11}$	0.0175	95.9 ms	7.00	1.27	11.8
$S_{12}$		7.66 ms	2.32	2.93	11.8
$S_{21}$	0.0220	13.1 ms	10.0	1.23	17.0
$S_{22}$		114 ms	17.6	1.68	125
$S_3$	$1.70 \times 10^{-5}$	199 ms	12.5	2.67	846
$S_4$	$1.10 \times 10^{-5}$	–	1	0	1
$A_{11}$	$3.72 \times 10^{-3}$	141 ms	12.2	1.48	40.0
$A_{12}$		17.2 ms	12.5	0.996	12.4
$A_2$	0.0111	126 ms	12.1	1.67	64.4
$A_3$	0.0136	–	1	0	1

Chapter 2, in part, is currently being prepared for submission for publication of the material. Bartol, Thomas M.; Sejnowski, Terrence J. The dissertation author was the primary investigator and author of this material.

### **3 A Phenomenologically Accurate and Computationally Efficient Event-Driven Model of Presynaptic Dynamics**

Using the validated MCell model and the results of the previous chapter as ground truth, we build an asynchronous phenomenological model that treats spikes and releases as point events and that jumps directly to the earliest next event time after each update to the state of the synapse. I treat vesicle release as a Poisson process with a decaying set of rate parameters and derive the equations for determining the timing of the next release event given the current time, the number of releasable vesicles, the nature of the decay in release rate, and the current state of facilitation relative to the most recent spike. Furthermore, I extend this framework to handle arbitrary numbers of synaptic processes and vesicle pools. Because of the event-driven structure, releases and other processes may occur with an arbitrary time resolution. Model outputs replicate the release time histograms obtained from full MCell simulations, with differences explained as sensitivity to the position of the  $\text{Ca}^{2+}$  sensor. Runtime complexity scales linearly with both the number of spikes and the total simulated time, with the latter only having a significant effect for extremely sparse input sequences. The event-driven structure of the model enables computationally efficient simulation of phenomenologically accurate vesicular release dynamics, amenable to inclusion in network models with many synapses. This will allow for controlled testing of which synaptic processes may be implicated in healthy and disease states of a network and what role each feature may play in information processing.

## 3.1 Methods

### 3.1.1 Model Overview

Vesicles in the model exist in homogeneous pools for sake of simplicity, each pool representing a different state. As the model evolves, driven both by action potentials and by spontaneous activity, the probabilistic state-transition rates change, dynamically updating the occupancy of each pool. Figure 3.1 shows all pools and vesicle-exchange pathways modeled in this chapter, representing both the spontaneous and the spike-evoked rates of transition.

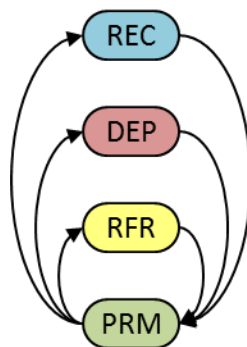


**Figure 3.1: Vesicle State-Transition Diagram.**

Vesicles transition between pools (colored shapes) during point event times for different processes (arrows). PRM holds the primed vesicles of the readily releasable pool (RRP); RFR holds vesicles in a post-release refractory period (see Results 3.2.1.1); DEP holds vesicles inactivated by release-independent depression (see Results 3.2.1.2); REC holds recycling vesicles after release events. Arrow from PRM to REC depicts vesicle release and reuptake, while arrow from PRM to RFR depicts simultaneous transition of all other primed vesicles in the active zone into a refracted state. Arrow from RFR back to PRM depicts vesicles coming out of refractory period, while arrow from REC back to PRM depicts redocking of recycled or reserved vesicles. Arrows from PRM to DEP and back respectively depict release-independent depression and recovery from depression.

The model treats the arrival of spikes, the fusion of vesicles, the end of the post-release refractory period, and the recruitment of vesicles to release sites as point events. Therefore, although events can occur at arbitrarily fine temporal resolution, this treatment effectively limits the resolution to the time scale of the processes in question, from a hundred microseconds to several milliseconds for spikes, releases, and priming events (Acuna et al., 2014; Pabst et al., 2002; Sabatini & Regehr, 1996). To avoid the cost of simulation between these time points, each synaptic process must be able to predict the timing of its next event from the synaptic state at a given point in time. Given that the model is able to do this (see next section), it stores all predicted next event times in a vector,  $\mathbf{n}$ , where the index corresponds to the event ID. Extracting the timing of the next event,  $t_e$ , and the identity,  $i_e$ , then simply requires finding the minimum:

$$t_e = \min_i \{\mathbf{n}\}, \quad (3.1)$$

$$i_e = \operatorname{argmin}_i \{\mathbf{n}\}. \quad (3.2)$$

Once it has chosen a next event, the model jumps forward to that time and performs the relevant update to the synaptic state before calculating a new set of event times, iterating until some specified stop time  $T$ . We derive how the model calculates new event times for each process in the next section.

### 3.1.2 Computing Next Event Times

All transitions in the model, other than spike times, take the form of Poisson processes with potentially time-varying rate parameters. Since the model is event-driven, each process needs to predict its next event time relative to the current state of the synapse. The probability for a Poisson event not occurring within a time window  $\Delta t$  after the current time  $t$  is

$$P(t_e \notin [t, t + \Delta t]) = e^{-\lambda(t)\Delta t}, \quad (3.3)$$

where  $t_e$  is the next event time and  $\lambda(t)$  is the average Poisson process rate in the interval (Cooper, 2005). The probability of an event time occurring within an interval  $[0, t)$  is then the complement of the product of the probabilities of not occurring in all subintervals:

$$\begin{aligned} P(0 \leq t_e < t) &= 1 - P(t_e \geq t) \\ &= 1 - \prod_0^t e^{-\lambda(t')\Delta t}. \end{aligned} \quad (3.4)$$

Letting  $\Delta t \rightarrow 0$  and bringing the exponential outside the product yields the general form

$$P(0 \leq t_e < t) = 1 - \exp\left(-\int_0^t \lambda(t') dt'\right). \quad (3.5)$$

This represents a cumulative distribution function, where all possible event times map to a number on the interval  $[0, p_e)$ , where  $p_e$  is the probability of the event occurring in finite time. Therefore, a random sample from the uniform distribution can predict an event time for a general synaptic process, starting at any time.

### 3.1.2.1 Spontaneous Events

Spontaneous events occur even in the absence of spiking activity, such as the neurotransmitter release events that induce mini-EPSCs (Kato et al., 2007; Malgaroli & Tsien, 1992; Nanou et al., 2016). Such processes have essentially constant rate parameters, proportional to the number of vesicles in the pool producing the event:

$$\lambda(t) = N_v \lambda_0, \quad (3.6)$$

where  $N_v$  represents the number of vesicles and  $\lambda_0$  the rate per vesicle.

To choose the next events time  $t_e$  after the current time  $t$ , first select a random number  $r_e \sim \mathcal{U}(0,1)$  from the uniform distribution, and then compute the inverse CDF after plugging the rate parameter  $\lambda(t)$  into Equation 3.5:

$$\begin{aligned}
r_e &= 1 - \exp\left(-\int_t^{t_e} N_v \lambda_0 dt'\right) \\
&= 1 - \exp(-N_v \lambda_0 (t_e - t)).
\end{aligned} \tag{3.7}$$

Solving for  $t_e$ , this yields

$$\begin{aligned}
t_e &= t - \frac{\ln(1 - r_e)}{N_v \lambda_0} \\
&= t + \text{exprnd}((N_v \lambda_0)^{-1}),
\end{aligned} \tag{3.8}$$

where  $\text{exprnd}(\tau)$  represents a random number from the exponential distribution with mean parameter  $\tau$ . This is the typical result for Poisson processes where the interval between successive events follows an exponential distribution with a mean parameter equal to the average interval (Cooper, 2005).

### 3.1.2.2 Spike-Evoked Events

When an action potential arrives at a presynaptic terminal, it elicits a transient influx of  $\text{Ca}^{2+}$  through voltage-dependent calcium channels (VDCCs), which falls off exponentially with time due to diffusion, buffering, and active pumps (see Chapter 2 Methods 2.1.1.1, Results 2.2.1). In response,  $\text{Ca}^{2+}$ -dependent processes, including both synchronous and asynchronous vesicle fusion, follow a similar time course with respect to their instantaneous rates. Release rates quickly rise to maximum (within a couple milliseconds) before falling exponentially toward baseline, with around four exponential decay components (see Table 2.3 in Chapter 2 Results 2.2.3.2). During the decay phases of release (or of any spike-evoked synaptic process), the (random) intervals between events must start small (fast rate) and increase with time since the spike (slower rate).

To derive a formula for determining the next spike-evoked event time, I treat each component of the synaptic process as a Poisson process with an exponentially decaying rate parameter, according to

$$\lambda(t) = \frac{N_v P}{\tau} e^{-(t-t_s)/\tau}, \quad (3.9)$$

where  $P$  is the fitted area under the rate curve (effectively the probability of release from that component if  $P < 1$ ),  $\tau$  is the time constant of rate decay, and  $t_s$  is the time of the last spike. Plugging this into Equation 3.5 produces

$$\begin{aligned} r_e &= 1 - \exp\left(-\int_t^{t_e} \frac{N_v P}{\tau} e^{-(t'-t_s)/\tau} dt'\right) \\ &= 1 - \exp\left(N_v P (e^{-(t_e-t_s)/\tau} - e^{-(t-t_s)/\tau})\right) \end{aligned} \quad (3.10)$$

for a current time  $t > t_s$ . Solving for  $t_e$  yields

$$t_e = t - \tau \ln\left(1 + \frac{\ln(1 - r_e)}{N_v P e^{-(t-t_s)/\tau}}\right). \quad (3.11)$$

This formalism ensures that event intervals close to the spike time are shorter than those further out.

Note that the above equation can produce complex or undefined event times. Therefore, we introduce an intermediate, exponentially distributed random variable  $K_{se}(t; t_s)$ , whose mean parameter value grows with time since the last spike and shrinks with a larger expected event count ( $P$ ) or number of vesicles ( $N_v$ ):

$$K_{se}(t; t_s) = \text{exprnd}\left(\left(N_v P e^{-(t-t_s)/\tau}\right)^{-1}\right). \quad (3.12)$$

Applying this to Equation 3.11 reveals that the next release time is both real and finite only when this variable is less than one. Otherwise, the model sets the next event time to infinity:

$$t_e = \begin{cases} t - \tau \ln(1 - K_{se}(t; t_s)) & K_{se}(t; t_s) < 1 \\ \infty & K_{se}(t; t_s) \geq 1 \end{cases} \quad (3.13)$$

By setting  $K_{se}$  equal to one, the probability of any further events from this exponential component after time  $t$  is

$$1 = -\frac{\ln(1 - p_e)}{N_v P e^{-(t-t_s)/\tau}}$$

$$p_e = 1 - \exp(-N_v P e^{-(t-t_s)/\tau}). \quad (3.14)$$

Thus, such events are more likely to occur with more vesicles, with a higher expected value, or closer in time to the most recent spike (relative to  $\tau$ ). This way, subsequent release times become less likely and further apart the further out into the tail of the release rate profile the simulation goes. Figure 3.2 shows how this event-generation scheme matches the analytically predicted histograms of Equation 2.17 in Chapter 2 Results 2.2.3.

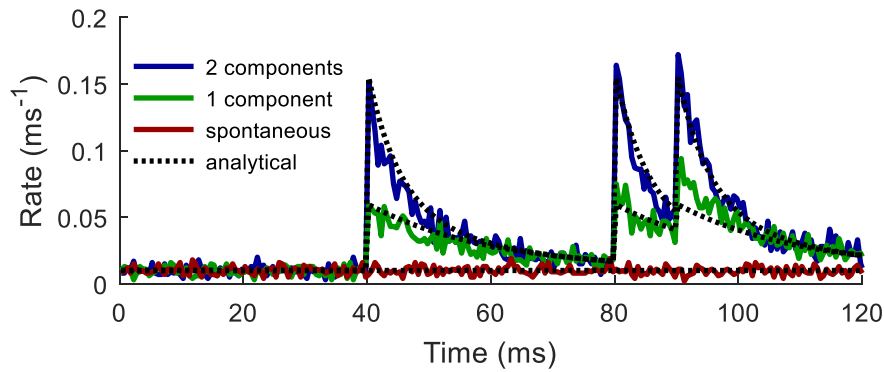


**Figure 3.2: Histogram of Spontaneous and Spike-Evoked Processes.**

Histograms generated over 2000 trials with 0.5-ms bins. 0 – 40 ms: Spontaneous event rate follows flat line. 40 – 80 ms: In response to one spike with one (green) or two (blue) components. 80 – 120 ms: Responses to two spikes in close succession (ISI = 10 ms), with components building off of each other. Parameter values:  $\lambda_0 = 0.01 \text{ ms}^{-1}$ ,  $P_1 = 0.5$ ,  $\tau_1 = 5 \text{ ms}$ ,  $k_1 = 0.5 \text{ ms}^{-1}$ ,  $\mu_1 = 2 \text{ ms}$ ,  $\sigma_1 = 0.3 \text{ ms}$ ,  $P_2 = 1$ ,  $\tau_2 = 20 \text{ ms}$ ,  $k_2 = 0.1 \text{ ms}^{-1}$ ,  $\mu_2 = 10 \text{ ms}$ ,  $\sigma_2 = 3 \text{ ms}$ .

Of course, because it takes finite time for  $\text{Ca}^{2+}$ -sensitive processes to detect the spike-evoked calcium influx, the events cannot begin instantly.  $\text{Ca}^{2+}$  ions must transition through numerous stochastic processes, entering the axon at some point during the AP, binding and unbinding with buffering molecules as they diffuse, and associating with the  $\text{Ca}^{2+}$  sensor, all of which may be considered a Markov chain Monte Carlo process. Therefore, to represent the time it takes for the  $\text{Ca}^{2+}$  ions to reach the sensor through buffered diffusion, I add a random delay relative to the originally calculated spike time, sampled from an ex-Gaussian distribution that is specific to each component  $c$  of the activity profile:

$$t_{0,c} = t_s + x_c + n_c, \quad (3.15)$$

where  $x_c \sim \mathcal{X}(k_c)$  is an exponentially distributed random number with rate parameter  $k_c$  and  $n_c \sim \mathcal{N}(\mu_c, \sigma_c^2)$  is normally distributed. This random delay acts as a convolutional filter on the exponentially decaying rate profile described above and leads to a distribution described in Equations 2.18-2.22 in Chapter 2 Results 2.2.3.1. To ensure that this method produces a spike-evoked event histogram that matches the empirical distribution after many trials, the model calculates the value of  $t_{0,c}$  once for each spike and vesicle pool, essentially treating it as the spike time for that activity component. Thus, each component has its own “idea” of when the latest spike occurred, and they calculate their subsequent event times as described above, using  $t_{0,c}$  instead of  $t_s$ .

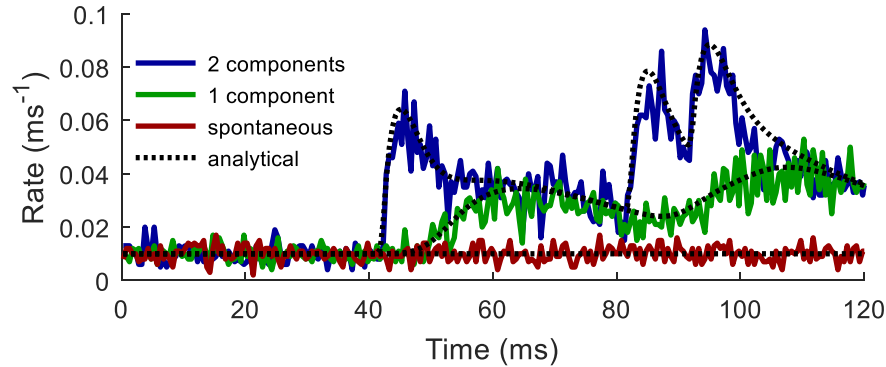


**Figure 3.3: Spike-Evoked Processes with Ex-Gaussian Delay Follow Analytical Predictions.**

Same toy process as Figure 3.2, with a temporal filter implemented by adding random delays after the spike event. 0 – 40 ms: Spontaneous event rate the same as in Figure 3.2. 40 – 80 ms: In response to one spike with one (green) or two (blue) components, with rising phases clearly visible. 80 – 120 ms: Responses to two spikes in close succession (ISI = 10 ms), with components building off of each other. Parameter values:  $\lambda_0 = 0.01 \text{ ms}^{-1}$ ,  $P_1 = 0.5$ ,  $\tau_1 = 5 \text{ ms}$ ,  $k_1 = 0.5 \text{ ms}^{-1}$ ,  $\mu_1 = 2 \text{ ms}$ ,  $\sigma_1 = 0.3 \text{ ms}$ ,  $P_2 = 1$ ,  $\tau_2 = 20 \text{ ms}$ ,  $k_2 = 0.1 \text{ ms}^{-1}$ ,  $\mu_2 = 10 \text{ ms}$ ,  $\sigma_2 = 3 \text{ ms}$ .

Many synaptic processes, such as vesicle release, use a combination of spontaneous and spike-evoked event timing, often with more than one exponential component. In these cases, each component can calculate its next event time independently, and the process will use the earliest of the calculated times. Figures 3.2 and 3.3 both show how the event histograms align with predictions for toy synaptic processes with multiple components, in the case of single spikes. For more complex spike trains, responses from consecutive spikes interfere with each other, such that prior to the delayed response start time  $t_{0,c}$  to spike  $n$ , the synaptic process must continue to make predictions relative to spike  $n - 1$ , using the value of  $t_{0,c}$  from the previous spike as the onset of its response phase. Once a predicted event time comes after the newest spike's delay, however, the process switches to responding to the latest spike. The post-

spike transition period awaiting the buffered-diffusion delay follows Equations 2.23-2.26 in Chapter 2 Results 2.2.3.1.

### **3.1.3 Model Dependencies**

Upon each event, the synapse receives a signal to update its state in some process-dependent manner. The update could involve the transition of vesicles from one pool to another, or it could entail spike-evoked changes in the transition rates of other synaptic processes, as in short-term facilitation. Once the synapse has changed its state, it recalculates the next event times for any process that might be affected. For instance, upon a release event, the releasable vesicle pool decrements by one while the empty pool increments. This change requires recalculation not only for the next release event, but also for the next vesicle reuptake event, likely sooner than the one previously calculated since the recycling pathway now has an extra vesicle (see Figure 3.1 in Methods 3.1.1 for the vesicle pools and process descriptions; see Methods 3.1.3.2 for how to recalculate times upon vesicle pool updates). To accomplish this, I constructed a set of general classes (in MATLAB; see [github.com/soiens24/Presynaptic\\_Framework](https://github.com/soiens24/Presynaptic_Framework) for source code) that track states for vesicle pools and synaptic processes and that notify one another of any changes (see Figure 3.4). This structure allows the model to act asynchronously and to scale efficiently.

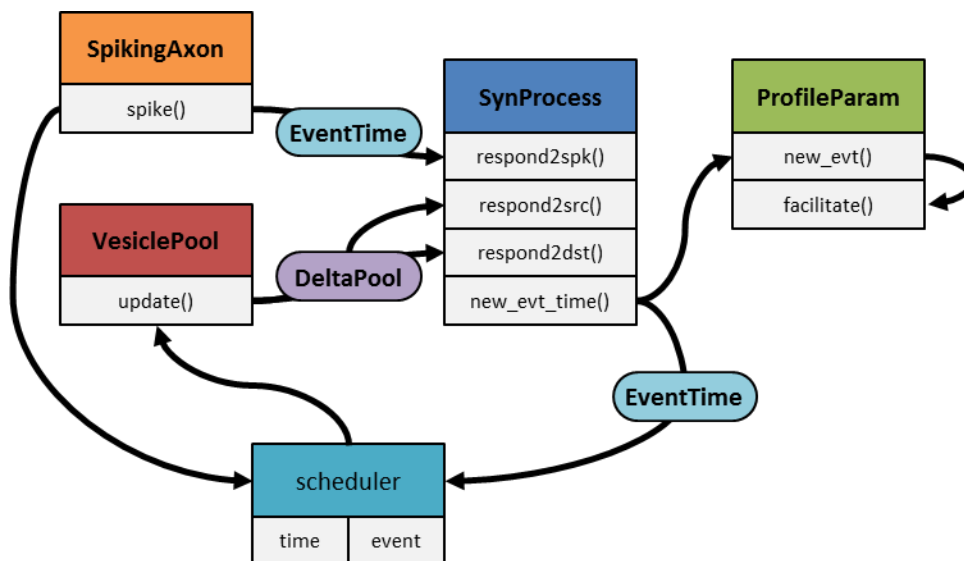


**Figure 3.4: Class Dependencies of the Event-Driven Model.**

Scheduler determines earliest next event time and updates synapse state according to each process' user-defined function. VesiclePool updates cause SynProcess updates for processes coming from and feeding into the pool ('respond2src' and 'respond2dst', respectively), depending on the change in pool size (DeltaPool). SynProcesses contain sets of ProfileParams that calculate new event times ('new\_evt') and notify the scheduler via an EventTime. SpikingAxon simply sends spikes to the model and may be elicited by anything in the simulation, such as a source model neuron in a network simulation.

At the beginning of the simulation, all vesicle pools (VesiclePool) are initialized to their desired sizes, and all synaptic processes (SynProcess) calculate their initial (spontaneous) event times, which are added to the scheduler. Then the simulation begins, and the scheduler jumps to the first event time, whether a spike or a vesicle transition. Upon reaching an event, the scheduler notifies a user-defined function that determines how it affects the synapse. When the function requires that a vesicle pool change size, the pool notifies the synaptic processes that use it as a source, which in turn recalculate new event times and notify the scheduler of the update. Below, I discuss these steps in more detail.

### 3.1.3.1 Spike Events

Each time a spike arrives from the axon, whether from a set of precomputed spike times or from an asynchronous network model, all spike-evoked synaptic processes must update their next expected event times. No vesicles change states, but each state transition process (the arrows in Figure 3.1 in Methods 3.1.1) will recalculate its spike-evoked event time according to Equations 3.11-3.15 in Methods 3.1.2.2, including the onset delay of Equation 3.15 and the facilitated rate of release described below, and update the corresponding value in  $\mathbf{n}$  if the new time comes earlier.

Numerous  $\text{Ca}^{2+}$ -dependent processes in the synapse increase in rate in response to high spiking activity (Ben-Johny & Yue, 2014; Brody & Yue, 2000; Hosoi, Holt, & Sakaba, 2009; Hosoi, Sakaba, & Neher, 2007; A. Lee et al., 2002; J. S. Lee et al., 2012; Neher & Sakaba, 2008; Okamoto et al., 2016; Sakaba, 2006; Sakaba & Neher, 2001; Wadel, Neher, & Sakaba, 2007; L. G. Wu, Hamid, Shin, & Chiang, 2014; X. S. Wu et al., 2009; X. S. Wu et al., 2014; J. Xue et al., 2011; L. Xue et al., 2012; Yamashita, Eguchi, Saitoh, von Gersdorff, & Takahashi, 2010; L. Yao & Sakaba, 2012; Yue & Xu, 2014), in a manner analogous to the facilitation of vesicle release probability. The facilitation function described in Equations 2.27-2.37 in Chapter 2 Results 2.2.5.1 therefore generally applies to all spike-evoked presynaptic processes. To recapitulate, spike-evoked processes act in this model as Poisson processes with exponentially decaying rate parameters and integrated rates  $P$ , which is related to probability of an event occurring over all time but may exceed one. The value of  $P$  on spike  $n$  depends on its baseline value  $P_0$  and on the facilitation factor for the spike,  $F(n)$ :

$$P(n) = P_0 \cdot F(n). \quad (3.16)$$

The value of  $F(n)$  depends on the nonlinear product of a set of internal facilitation state parameters  $f_k(n)$  as

$$F(n) = \prod_{k=1}^M f_k(n)^{\xi_k}, \quad (3.17)$$

where  $M$  is the number of components and  $\xi_k$  are the nonlinearities. The value of  $f_k(n)$  decays with time since the previous spike and increments by at most one at each spike according to

$$g_k(n) = f_k(n-1)e^{-\Delta t/\tau_k},$$

$$f_k(n) = 1 + g_k(n) - \left(\frac{g_k(n)}{N_k}\right)^{N_k}, \quad (3.18)$$

where  $g_{jk}(n)$  represents the amount of the facilitation parameter “left over” from the previous spike,  $\tau_k$  represents the time constant for decay, and  $N_k$  is the saturation level.

When a spike event occurs, the scheduler notifies all synaptic processes via their ‘respond2spk’ function, which signals each process to reevaluate its next scheduled event time. The process calls upon its components (except the spontaneous component), each of which has a different time course, a different probability of responding, and a different delay. Each component (ProfileParam) first calculates a random delay from the spike time until it begins to respond to the new spike,  $t_{0,c}$ ; this is the temporal filter described in Equation 3.15 in Methods 3.1.2.2 and in Equations 2.18-2.22 in Chapter 2 Results 2.2.3.1. It also determines the magnitude of facilitation for the latest spike based on the interval from the previous spike (Equation 3.18). Whether it recalculates a new event time depends on when its previously planned event falls relative to the end of the delay. If the next event occurs before the delay ends, the  $\text{Ca}^{2+}$  sensor has essentially not yet seen the  $\text{Ca}^{2+}$  from the latest spike, so it maintains its planned time. If, however, the delay ends before the planned event, the  $\text{Ca}^{2+}$  from the latest spike will interfere with the old plan, so it recalculates a new time, taking the facilitated rate into account. Recalculations use the number of vesicles in the source

pool at the time of the spike as  $N_v$  and the spike time as  $t$  in Equations 3.11-3.14 in Methods 3.1.2.2. Once the synaptic process has received any new times from each of its components, it takes the earliest one and compares it to its previously planned next event time. If the new time is earlier, it notifies the scheduler of the update.

### 3.1.3.2 Vesicle Transitions

During most non-spiking events, one or more vesicle pools will change size as vesicles change state or move around the synapse. Because the rate at which any vesicle-transition process can occur depends directly on the number of vesicles available for the transition, those pools that change in size must notify all processes that depend on them both of the magnitude of the change and of how many remain in the pool. The model does this by adding event listeners for each pool's 'DeltaPool' signal that call the 'respond2src' (source pool) or 'respond2dst' (destination pool) function for each relevant process. How a 'SynProcess' responds depends on the sign of the change and on the circumstances of the function call. The different cases for changes in the number of vesicles of the source pool are discussed below. Similar considerations are given to changes in the number of vacancies in the destination pool for those pools with limited capacity, such as the RRP, which has a limited number of release sites (Neher, 2010; Stevens & Wang, 1995; J. Y. Sun & Wu, 2001; L. G. Wu et al., 2014).

Upon an increase in the size of its source pool, a process needs only to calculate the time at which the newly introduced vesicles "want" to trigger an event. Before the new vesicle(s) arrived, the process already had an idea of when its next event would be, based on the number of vesicles already at its disposal. However, when more vesicles arrive, there is some chance that one of them would trigger an event earlier than the one already calculated. This happens rarely in most situations, where the number of vesicles

already in the pool far outweighs the number added (typically only one vesicle at a time), since the earliest time produced by sampling from each of a large number of vesicles usually comes earlier than a single random sample. However, to avoid ignoring any new vesicle's alacrity for participating in a new event, the model samples the added vesicles by calculating a new event time as described above, using the number of added vesicles (usually 1) as the value of  $N_v$  and the time at which they are added as  $t$  in Equations 3.6-3.14 in Methods 3.1.2. The process only takes the result of this sample as its new next event time if it precedes the time previously calculated. In this comparatively rare case, it notifies the scheduler of the update.

When an event causes a vesicle pool to decrease in size, one of two scenarios is possible from the perspective of a process that uses that vesicle pool as a source: either the same process triggered the event, or another process that has the same vesicle pool source triggered it. In the former case, the process simply recalculates a new event time without exception, using the number of vesicles remaining in the pool as the value for  $N_v$ . In the latter case, the process must randomly determine whether to recalculate. Since all vesicles in a pool are treated identically, the probability that a vesicle removed by the other process was one that would have been involved next with the current process is  $n_r/(N_v + n_r)$ , where  $n_r$  is the number of vesicles removed and  $N_v + n_r$  was the number of vesicles in the source pool before this event. If it decides to recalculate, it does so as described above, and it sends a notification to the scheduler of the update.

One important caveat affects the event-time recalculations describe above: When a component of a synaptic process has to deal with an update in the (usually) short interval between the time of the latest spike ( $t_s$ ) and the end of its random delay before responding to the spike ( $t_{0,c}$ ), it must consider both the latest and the previous spike times. If its earliest planned time happens to fall before its delay ends, it must

continue to respond to the previous spike, using the old value of  $t_{0,c}$  and of its facilitation factor  $F_c(n-1)$ . If, however, the previously planned event falls after the delay for the latest spike, it must recalculate using the new  $F_c(n)$  and the new  $t_{0,c}$  as a starting point. In this latter case, because the current time is earlier than the start time for responding to the new spike, it uses  $t_{0,c}$  rather than the current time as the value of  $t$  in Equations 3.11-3.14 in Methods 3.1.2.2. Most of the time, though, vesicle pool updates will occur outside of a process' spike-response delay interval, so this caveat has a miniscule effect on the event rate histograms. Outside of this interval, spike-evoked processes can respond safely to just the latest spike times.

## 3.2 Results

### 3.2.1 Validation

The event-driven model seeks to balance the phenomenological realism of the MCell model with the computational scalability of simpler models and is to minimize the trade-off between the two. For validation, I compare the results of the model first to the MCell model off of which it was based and then to other models and experiment. The model proves to make useful predictions and allows sufficient flexibility to perform controlled experimental simulations of the synaptic processes necessary to explain physiological data.

#### 3.2.1.1 Replicating MCell Results

Because the results of MCell formed the basis for characterizing the dynamics of release (see Methods 2.1.1 in Chapter 2), I first sought to replicate the MCell results with the event-driven model. In the paper that introduced the model (Nadkarni et al., 2010) off of which I based this model's phenomenology of the current model, vesicles of the readily

releasable pool (RRP) sit docked in a small cluster (usually seven vesicles) at some fixed distance (10-400 nm) from a cluster of a certain number (1-208) voltage-dependent  $\text{Ca}^{2+}$  channels (VDCCs). When an action potential (AP) evokes an influx of  $\text{Ca}^{2+}$ , it diffuses passively to the SNARE complex of each docked vesicle, which acts as the trigger for vesicle fusion and release of neurotransmitter. The  $\text{Ca}^{2+}$ -driven kinetics of the synchronous and asynchronous release mechanisms were explored in the previous chapter. To replicate the same model here, I established three vesicle pools: the primed vesicle pool (PRM) initialized to seven vesicles, the recycling pool (REC) initialized to zero, and the “refractory pool” (RFR) initialized to zero, which are a subset of the pools shown in Figure 3.1 in Methods 3.1.1. Vesicles of the RRP engaged in spontaneous and spike-triggered release, with facilitation, following the parameters outlined in the previous chapter for a SNARE complex located 400 nm from a cluster of 100 VDCCs (see Results 2.2.3 in Chapter 2). Both synchronous and asynchronous release were treated as independent synaptic processes, as outlined above in Methods, transferring one vesicle from PRM to REC (representing release and removal of a vesicle) and all the rest of PRM to RFR (representing the post-release refractory period). Another synaptic process acted as the end of the refractory period, transferring one vesicle at a time from RFR to PRM, which represents simply a change in state for vesicles sitting within the RRP. A redocking synaptic process takes one vesicle at a time from REC to PRM with a time constant of 2.8 s, as in the MCell model (Nadkarni et al., 2010). The vesicle state diagram for this model is shown in Figure 3.5A.

The efficiency and flexibility of the model allow for simulating a large number of trials several orders of magnitude faster than MCell (see Runtime in Results 3.2.2), for testing the output in response to arbitrary spike trains, and for testing the effect of adding or removing features from the model. Figure 3.5B shows the release rate histogram

obtained by running 100,000 trials in response to a single AP. Notice that the several of the very low-probability components of synchronous release do not appear, since they would require billions of trials to produce a discernable histogram at this resolution. The combined release rate (black) matches the results of the single-AP MCell experiments (Figure 3 in (Nadkarni et al., 2010)) in that it exhibits a seeming triple-exponential shape, where the first two components of synchronous release account for the “superfast” and “fast” components and the middle component of asynchronous release accounts mainly for the “slow” component. Spontaneous release results virtually entirely from the asynchronous mechanism. A simpler model could consolidate the two release mechanisms into a single “net” mechanism, further increasing the efficiency of the model (see Chapter 4 for more discussion). Applying a random spike train over 1000 ms for 1000 trials produced the results in Figure 3.5C-D, which show the release events and track the changes in size of the vesicle pools describes above. Both facilitation and depletion-induced depression are evident in the changes in density of the release rasters. This demonstrates the ability of the model to respond realistically to arbitrary input and to allow investigation into the internal dynamics that explain the observable effects.

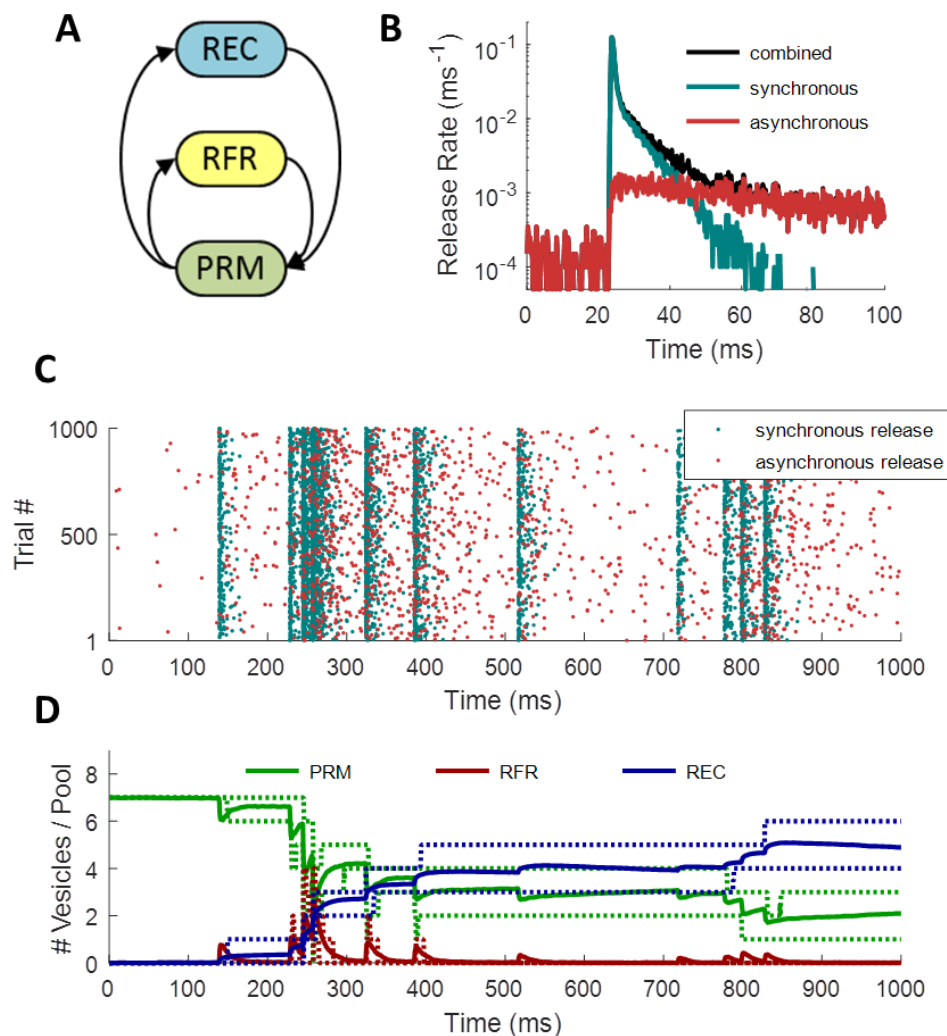


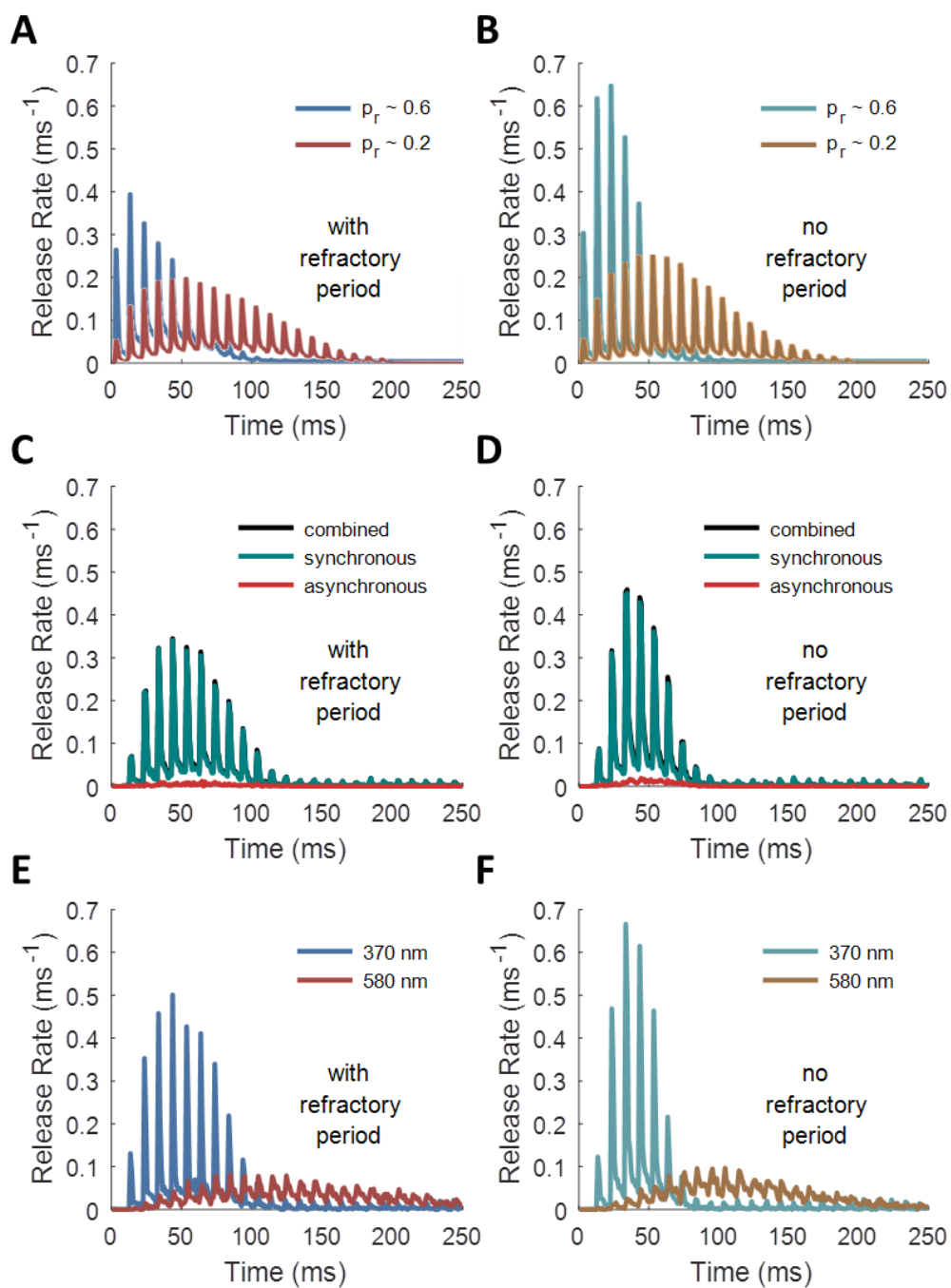
**Figure 3.5: Structure and Output of the Simple MCell-Analog Model.**

(A) Vesicle state diagram: PRM is the primed (releasable) state, RFR is the refracted state, REC is the recycling (undocked) state. Arrows signify vesicle transitions. (B) Release histograms for 100,000 trials of a synapse of seven docked vesicles responding to a single spike at 20 ms. (C) Release raster in response to random spike train stimulus. Colored dots correspond to release mechanism (synchronous = green; asynchronous = red), the same color scheme as in (A). (D) Number of vesicles transitioning over time between the primed/docked state (PRM, green), the post-release refractory state (RFR, yellow) and the recycling/undocked state (REC, blue). Solid lines indicate mean values over 1000 trial, while dotted lines indicate 25th and 75th percentiles. Value of recycling pool initialized to zero for comparison with (Nadkarni et al., 2010), which did not include an extra recycling pool but did allow for redocking of used vesicles.

One feature of interest in this model is the post-release refractory period. Dobrunz et al. (1997) have observed that the probability of vesicle release significantly drops immediately after a first vesicle fuses, preventing multiple vesicles from fusing at the same time at the same active zone. This likely arises from so-called “lateral inhibition” of release, where changes in the mechanical properties of the membrane immediately around the fused vesicle increase the energy barrier for membrane fusion (Dobrunz et al., 1997; Stevens & Wang, 1995). Nadkarni et al. (2010) modelled this in MCell as a refractory state that all unfused vesicles in the active zone enter after a release, each returning to a releasable state with a time constant  $\varepsilon = 6.34$  ms (see Table 2.2 in Chapter 2 Methods 2.1.1.3). Such a refractory period has significant effects on a synapse’s release rate histogram, particularly for those with high initial probabilities of release (see Figure 3.6 below and Figure 7 in Nadkarni et al. (2010)). Removing this refractory period has the dual effect of increasing probability of release for early spikes in a train of action potentials and of accelerating depletion. Including the release refractory period extends the time window for synaptic response to its input, as seen in Figure 3.6 below.

**Figure 3.6: Comparisons of Event-Driven Release to MCell Model, with and without Post-Release Refractory Period.**

Spike trains delivered at 100 Hz. MCell traces reproduced with permission from (Nadkarni et al., 2010). All histograms use 1-ms bins. (A) MCell release histograms for synapses with high initial probability of release ( $p_r = 0.6$ , blue) and with low initial probability of release ( $p_r = 0.2$ , red), with a post-release refractory period of  $\varepsilon = 6.34$  ms. (B) MCell release histograms for synapses with high initial probability of release ( $p_r = 0.6$ , turquoise) and with low initial probability of release ( $p_r = 0.2$ , gold), with no post-release refractory period. Lack of refractory period amplifies spike response but shortens release window. (C) Release histogram of event-driven model with parameters derived for SNARE complex 400 nm from  $\text{Ca}^{2+}$  source (see Results 2.2.3 in Chapter 2), including a post-release refractory period. (D) Same model as (C), but without a refractory period. (E) Release rates of two active zones with baseline release rates fitted at 370 nm and 580 nm from the  $\text{Ca}^{2+}$  source (facilitation functions still fitted at 400 nm), with a refractory period. (F) Same model as (E), but without a refractory period.



Note that the model's release rate histogram profiles in Figure 3.6C,D do not quite match those read from MCell in Figure 3.6A,B. In particular, while the release rate reaches a comparable magnitude, the window for significant release probability cuts off several tens of milliseconds earlier than with the MCell model. I hypothesized that this results from the fact that the vesicles of the MCell RRP were distributed in space. Peak release rate falls off exponentially with distance from the  $\text{Ca}^{2+}$  source (see Results 2.2.4 in Chapter 2), whereas the release rate parameters and facilitation meta-parameters in the event-driven model were derived for a release site at a single location in space, specifically, for a SNARE complex located 400 nm from a cluster of 100 VDCCs (see Results 2.2.3, 2.2.5.2 in Chapter 2).  $\text{Ca}^{2+}$  sensors closer to the VDCC cluster should respond more quickly and over a shorter time window than those farther away. Therefore, a pool of vesicles over a range of distances would exhibit a mix of high release rate (for more proximal vesicles) and longer-lasting release (for more distal vesicles). Figure 3.6E,F show how releasable pools at two arbitrary distances can exhibit each of these properties in turn. Further discrepancies between the MCell and event-driven models may be due to some form of distance-dependence in the dynamics of the facilitation function. That is, the amount of facilitation in per-vesicle release probability from spike to spike may depend nonlinearly on the amount of  $\text{Ca}^{2+}$  available to the sensor at a given distance. This would cause different release components to facilitate differently at different distances from the  $\text{Ca}^{2+}$  source, whereas the model presented here assumes that the same facilitation function applies at all locations. To determine how the function might depend on location, however, falls outside the scope of this dissertation.

### 3.2.1.2 Depressing Synapses

Hitherto, I have dealt primarily with a model for synaptic facilitation, which dominates the phenomenology of the axon terminals of pyramidal cells in hippocampus (Dobrunz et al., 1997; Dobrunz & Stevens, 1997; Kandaswamy et al., 2010). However, many types of synapses, notably from cortical pyramidal cells (Fuhrmann, Cowan, Segev, Tsodyks, & Stricker, 2004; Thomson & Bannister, 1999; Thomson & Deuchars, 1994; M. Tsodyks et al., 1998), exhibit synaptic depression, either predominantly or in concert with facilitation. Three major types of depression may exist in synapses: release-dependent depression (RDD), caused by simple depletion of used vesicles; release-independent depression (RID), caused by AP-triggered mechanisms that reduce the probability of neurotransmitter release on subsequent spikes; and the post-release refractory period, discussed in the previous section.

In any synaptic model that tracks the size of the RRP, release-dependent depression falls out naturally as a consequence of vesicle use. As long as vesicles can deplete, the model has implemented RDD. The mechanisms for recovery, however, can vary widely, from a steady-state supply of new vesicles, to activity-dependent recycling (L. G. Wu et al., 2014; X. S. Wu et al., 2009; J. Xue et al., 2011; L. Yao & Sakaba, 2012), to multiple recycling and recruitment pathways (de Lange, de Roos, & Borst, 2003; Gandhi & Stevens, 2003; Z. Li et al., 2005; Okamoto et al., 2016; Rizzoli & Jahn, 2007; Y. Wu et al., 2014). Recruitment of new or recycled vesicles to the active zone should have a limit, though, because synapses each have a limited number of release sites, at least on a timescale shorter than long-term potentiation (Neher, 2010; Stevens & Wang, 1995; J. Y. Sun & Wu, 2001; L. G. Wu et al., 2014; Yang & Calakos, 2013). Figure 3.7 shows how depletion alone contributes to synaptic depression over extended periods of stimulation. When the number of vesicles in the RRP does not decrease with

every release, synaptic fidelity continues indefinitely, but when RDD is restored, release rate falls significantly within a relatively short time period. Recycling of used vesicles, especially in an activity-dependent manner can limit the effect of this form of depression.

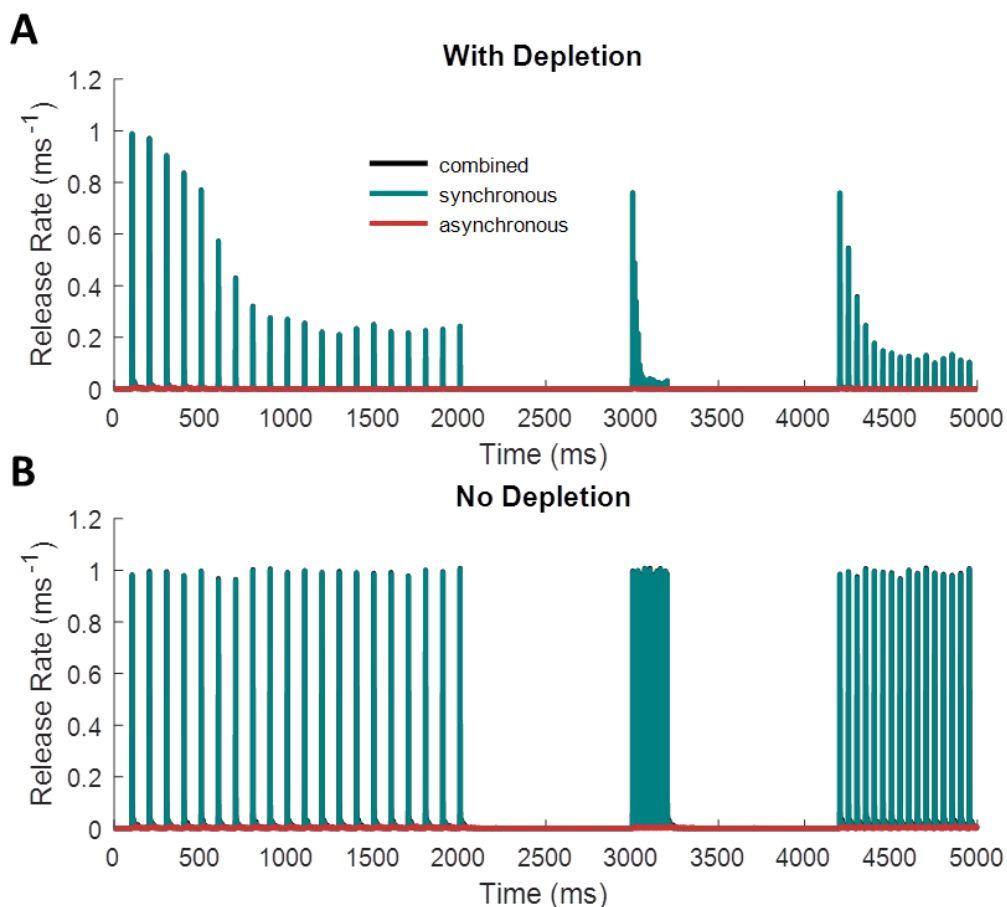


**Figure 3.7: Release-Dependent Depression Limits the Time Window for Synaptic Transmission under Sustained Stimulation.**

Spike trains consist of 20 APs at 10 Hz, followed by a 1-s delay, followed by 20 APs at 100 Hz, followed by a 1-s delay, followed by 20 APs at 20 Hz. Parameters for spike-evoked release rate profiles taken from fits at 160 nm from  $\text{Ca}^{2+}$  source (see Figure 2.18 in Chapter 2 Results 2.2.4), and facilitation disabled for clarity. (A) Normal synapse with depletion from RRP and a constant rate of redocking ( $\tau = 2.8$  s). (B) Synapse with depletion removed by omitting changes to vesicle pool sizes at each release event. Sustained high-fidelity transmission possible without depletion, or equivalently, with very fast replenishment of the RRP.

Another form of depression that features in certain synapses is release-independent depression (RID), where the probability of release decreases from spike to spike even without vesicle depletion. Fuhrmann et al. (2004) measured changes in synaptic fidelity in excitatory synapses of rat somatosensory cortex and observed a combination of RDD, RID, and frequency-dependent recovery (FDR) from depression. The changes in EPSC amplitude in response to different artificial spike train stimuli indicated a form of short-term depression (RID) acting independently of vesicle depletion and recovering more quickly under stronger stimulation (FDR), allowing the synapse to remain responsive even at high stimulus frequencies. Such opposing effects are consistent with a model of competitive interaction between one mechanism that suppresses  $\text{Ca}^{2+}$ -triggered release and one that restores it. In fact, studies have revealed a competition between calmodulin (CaM) and  $\text{Ca}^{2+}$  binding protein 1 (CaBP-1) in modulating the permeability of voltage-dependent  $\text{Ca}^{2+}$  channels (VDCCs) in neurons (Hardie & Lee, 2016; A. Lee et al., 2002). Inactivation of the VDCCs reduces the probability of release, but it also affects other  $\text{Ca}^{2+}$ -dependent processes. Direct inactivation of release sites, however, would have more local effects (Fioravante & Regehr, 2011).

In their model of RID-FDR, Fuhrmann et al. (2004) represented RID as a relative per-vesicle probability of release ( $U_{SE}$ ) that steps down by some fraction after each spike and exponentially recovers. They implemented FDR by having the time constant for this recovery also step down after each spike and exponentially recover. Although their model reasonably fit the data from their electrophysiological recordings, a model of competitive, stimulus-evoked inactivation/reactivation works just as well and seems more grounded in plausible physiology. Figure 3.8 shows how such a competitive model (cyan and red) compares to the Fuhrmann model (labelled RID-FDR in black). The

competitive model considers a release mechanism transition between an active and an inactive state, where the rate of inactivation ( $k_{RID}$ ) and the rate of reactivation ( $k_{FDR}$ ) both increase in response to spike-evoked  $\text{Ca}^{2+}$  and decay exponentially, according to

$$\tau_{RID} \frac{dk_{RID}}{dt} = k_{RID,0} - k_{RID} + P_{RID} \sum_{t_s \in \mathbf{S}} \delta(t - t_s), \quad (3.19)$$

$$\tau_{FDR} \frac{dk_{FDR}}{dt} = k_{FDR,0} - k_{FDR} + P_{FDR} \sum_{t_s \in \mathbf{S}} \delta(t - t_s), \quad (3.20)$$

where  $P_{RID}$  and  $P_{FDR}$  are the sizes of the respective jumps,  $t_s \in \mathbf{S}$  are the spike times,  $k_{RID,0}$  and  $k_{FDR,0}$  are the spontaneous (baseline) rates, and  $\tau_{RID}$  and  $\tau_{FDR}$  are the respective time constants. They each tug on the probability of the release mechanism being in the active state ( $A$ ), pulling it either toward zero (RID) or one (FDR):

$$\frac{dA}{dt} = -k_{RID}(t) \cdot A + k_{FDR}(t) \cdot (1 - A). \quad (3.21)$$

Figure 3.8A,C shows how insensitive the competitive model can be to different values of the inactivation time constant,  $\tau_{RID}$ , which can change by as much as an order of magnitude while still preserving the same overall shape of depression dynamics.

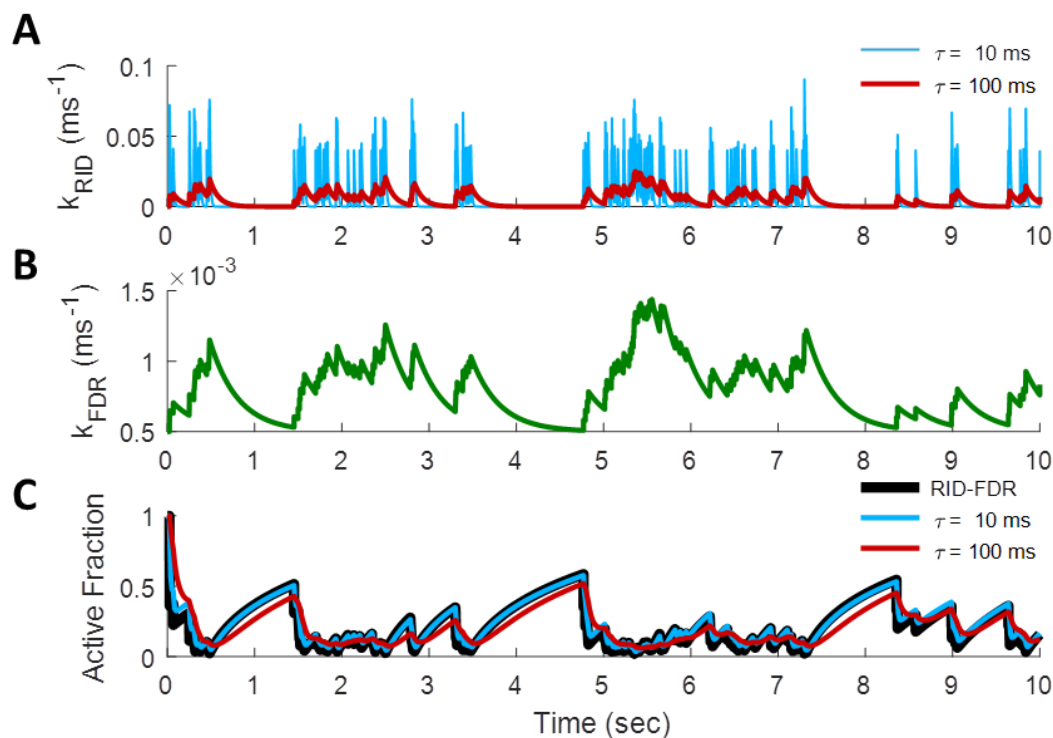


**Figure 3.8: Release-Independent Depression with Frequency-Dependent Recovery Equivalent to Competitive Model of Synaptic Inactivation and Reactivation.**

(A) Rate of inactivation process changing in response to a random spike train, with time constant  $\tau_{RID}$  at two separate orders of magnitude. (B) Rate of reactivation evolving in response to the same spike train, with a nonzero  $k_{FDR}$ . (C) Competitive models of RID-FDR (cyan and red) produce changes in synaptic release efficacy that closely follow the trajectory of the Fuhrmann et al. (2004) model.

The value of  $A$  could represent the fraction of VDCCs that have not been inactivated, in which case RID and FDR relate to the rates of  $\text{Ca}^{2+}$ -sensitive molecules interacting with the channels (Ben-Johny & Yue, 2014; Catterall et al., 2013; Hardie & Lee, 2016; A. Lee et al., 2002; Nanou et al., 2016). Alternatively, it could represent the fraction of docked vesicles whose fusion mechanisms remain unimpeded by some  $\text{Ca}^{2+}$ -dependent blocking mechanism (Fioravante & Regehr, 2011). For the event-driven model presented here, the latter is the less computationally expensive option. In this case, vesicles would stochastically transition between a depressed and an activated state, with transition rates  $k_{RID}$  and  $k_{FDR}$  determined as described above. Figure 3.9 shows the effect of introducing this form of short-term depression on synaptic dynamics for a synapse with a high initial probability of release, as is the case for most depressing synapses (C. C. Lee, Anton, Poon, & McRae, 2009; Rotman et al., 2011; Thomson & Bannister, 1999; M. Tsodyks et al., 1998; M. V. Tsodyks & Markram, 1997). Alternative formulations of RID might include adding a component to the release facilitation functions with a negative exponent ( $\xi$ ), which would allow the “facilitated” release probability to end up below baseline. I found, however, that the facilitation function used in this model, even with a negative exponent, does not match the dynamics of RID-FDR as well as the competitive state-transition model (data not shown). A new function that exclusively describes depression would enable efficient modelling of RID in future iterations of this model.

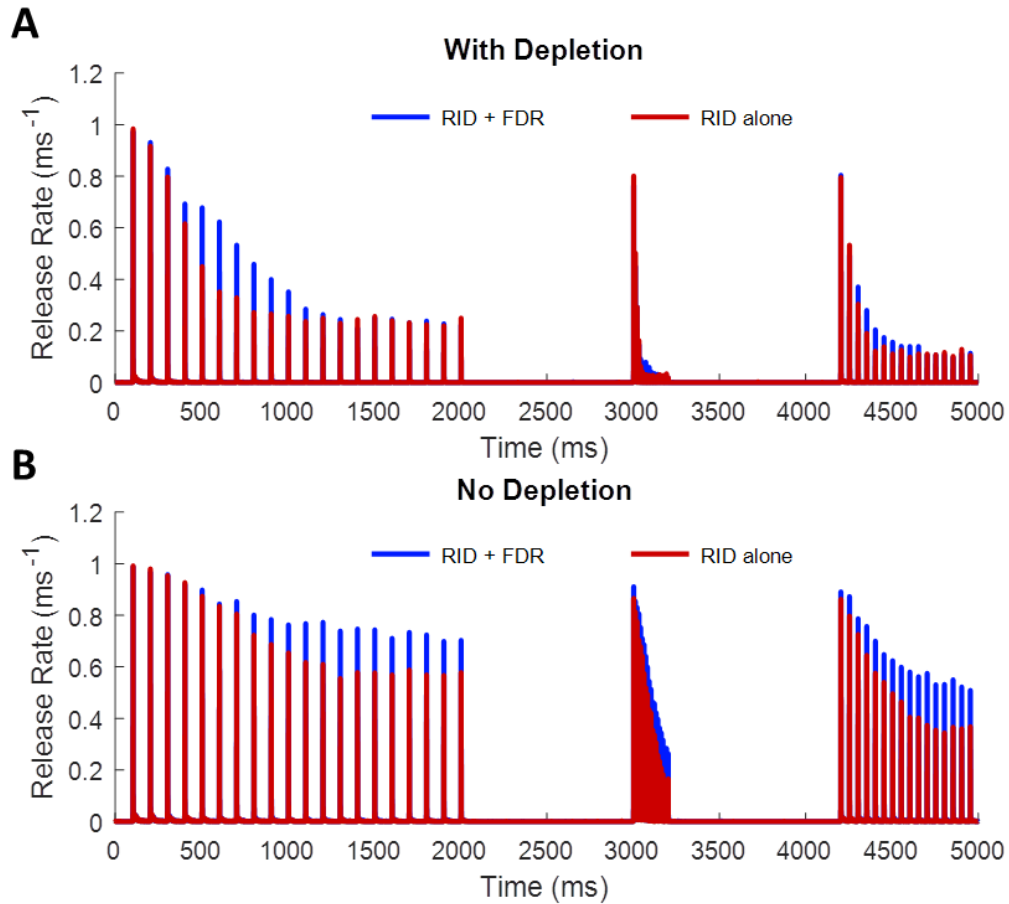


**Figure 3.9: Effect of Competitive RID-FDR Depression Model on Synaptic Dynamics.**

Same spike train as in Figure 3.7. Model includes depressed and active states for vesicles of the RRP. (A) With depletion (combined RDD and RID), frequency-dependent recovery (FDR) from the depressed state allows model to delay the reduction in release rate caused by depletion. (B) Without depletion (all depression caused by RID), FDR (blue) sustains release fidelity indefinitely over the levels attained by a constant rate of recovery (red).

Applying the model of RID-FDR that treats vesicles as transitioning between active and depressed states produces the results seen in Figure 3.9. In Figure 3.9A, both depletion (RDD) and RID are present, while in 3.9B, the “deactivation” of releasable vesicles is the only form of depression present. In RID, the rate of vesicle transition from the active state (PRM) to the depressed state (DEP; Figure 3.1) jumps with every AP and decays exponentially to zero (see Figure 3.8A). The rate of recovery is either constant (RID alone, red) or facilitating (RID + FDR, blue). Including the activity-dependent (i.e.,  $\text{Ca}^{2+}$ -dependent) recovery rate allows the synapse to mitigate the effects of depression for long spike trains, keeping the transmission fidelity within a useful range even for very high-frequency stimulation (Fuhrmann et al., 2004).

### 3.2.1.3 Achieving Sustained Facilitation with $\text{Ca}^{2+}$ -Dependent Recruitment

The generality of the event-driven model allows for controlled simulated experiments that can demonstrate which features of a synapse might explain the dynamics observed in physiological experiments. Kandaswamy et al. (2010) stimulated the Schaffer collateral fibers of rat hippocampal slices and performed whole-cell recordings of pyramidal cells in area CA1 and built a simple model to account for the patterns of facilitation in synaptic strength that they observed. In both observation and the fitted model, the synapses exhibited significant facilitation in synaptic strength on multiple time scales, coupled with a slower component of short-term depression that was presumably caused by vesicle depletion. The trend for a constant-rate stimulus of 40 Hz appears in Figure 3.10A (see Figure 1E in (Kandaswamy et al., 2010) for comparison to experimental recordings). However, when I applied the same 40-Hz stimulus to my model, described in Methods and seen in Figure 3.3 in Results 3.2.1.1, the released vesicles quickly depleted after an

initial facilitation (Figure 3.10B, blue). Sustained facilitation could not be achieved even for enhanced rates of recycling or for larger reserve vesicle pools (data not shown).

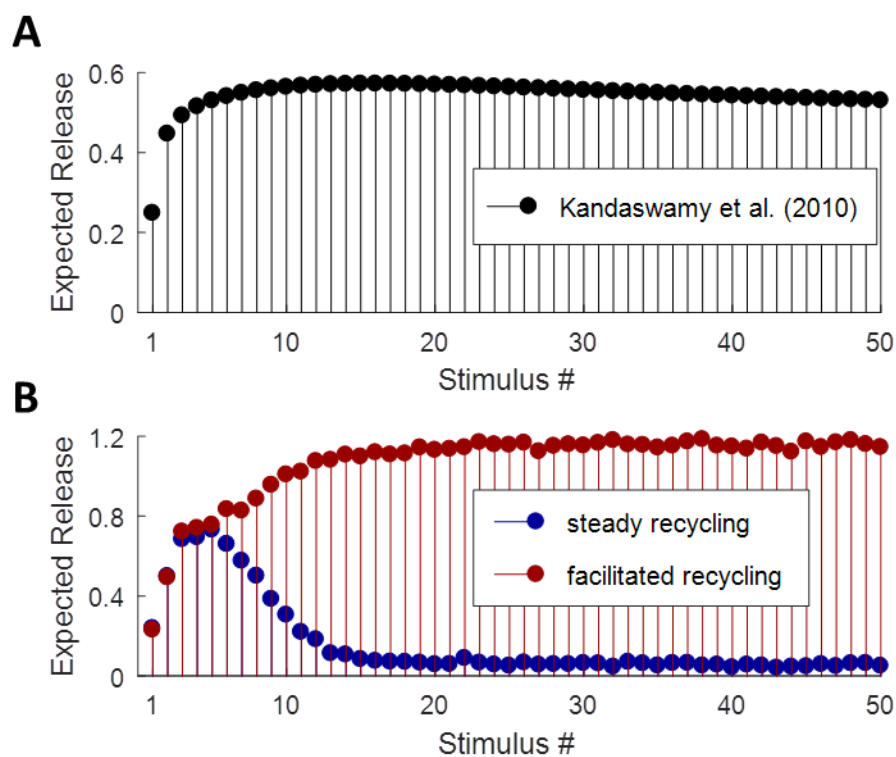


**Figure 3.10:  $\text{Ca}^{2+}$ -Dependent Vesicle Recruitment Enables Sustained Facilitation to Overcome Depletion.**

All plots reveal expected number of releases in response to each AP in a 40-Hz stimulus train. (A) Synaptic strength of model from (Kandaswamy et al., 2010) exhibits strong initial facilitation that is sustained over many spikes, decreasing gradually from depletion. (B) Output of the same event-driven model as in Figure 3.3 in Results 3.2.1.1. Expected number of release events per AP calculated from 10-ms time bins around spike times. With constant rate of redocking (blue), model shows both rapid facilitation and rapid and sustained depletion. Applying a facilitation function to the rate of vesicle redocking (red) restores high release fidelity under sustained stimulation.

The solution to this problem comes from research that demonstrates a relationship between  $[Ca^{2+}]_i$  and the rate of vesicle recruitment to release sites. Because  $[Ca^{2+}]_i$  so strongly depends on AP-mediated  $Ca^{2+}$  influx (Bischofberger et al., 2002; Neher & Sakaba, 2008; Simons, 1988), the level of  $Ca^{2+}$  in the intracellular space can serve as a useful proxy for measuring the recent level of spiking activity. Therefore, if the rate of vesicle recruitment to the RRP correlates with  $[Ca^{2+}]_i$ , then the synapse should be able to replace vesicles at a rate proportional to that at which it is depleting them, allowing it to maintain transmission fidelity even over long stimulus trains (Denker et al., 2011; Ertunc et al., 2007; Fernández-Alfonso & Ryan, 2004; Hallermann & Silver, 2013; Sara, Mozhayeva, Liu, & Kavalali, 2002). During more quiescent periods, the spontaneous undocking rate would shift the balance toward fewer occupied sites (Murthy, Schikorski, Stevens, & Zhu, 2001; Murthy & Stevens, 1999). In their study of the rat calyx of Held, Hosoi et al. (Hosoi et al., 2007) elucidated a linear relationship between  $Ca^{2+}$  concentration in the presynaptic volume and the rate of vesicle recruitment to the RRP, at low  $[Ca^{2+}]_i$ . According to their findings, the rate at which vesicles are recruited to the RRP depends linearly on the internal  $[Ca^{2+}]_i$  according to

$$k_1 = k_{1,b} + k[Ca^{2+}]_i, \quad (3.22)$$

where  $k_1$  is the rate of vesicle docking to a release site,  $k_{1,b} = 0.1$  pool/s is the  $Ca^{++}$ -independent docking rate, and  $k = 1.0$  pool/ $(\mu M \cdot s)$  gives the calcium dependence. Because the experiments were conducted at room-temperature, however, the precise values for these reaction rates could be different (Delvendahl, Vyleta, von Gersdorff, & Hallerman, 2016; Renden & von Gersdorff, 2007; Sabatini & Regehr, 1996; Watanabe et al., 2014).

Applying this concept to the model allows it to reclaim lost vesicles in an activity-dependent manner. This requires adding a spike-evoked component to the recycling

process (the pathway from REC to PRM in Figures 3.1, 3.4A) that evolves in proportion to the  $[Ca^{2+}]_i$  profile (see Figure 2.12 in Chapter 2 Results 2.2.3) according to Equation 3.22. The parameter values chosen were only first approximations, but including this feature restored the sustained level of facilitation seen in Figure 3.10B (red). This highlights the importance of  $Ca^{2+}$  mediated processes in vesicle recycling and retrieval in strongly facilitating synapses, and the model presented here provides a useful framework for studying the impact of synaptic structure and dysfunction on the transmission of signals between neurons.

This sustained level of facilitation was achieved even in the absence of a large reserve pool. A more complete model would include multiple recycling pathways, each acting on a different time scale (Kononenko & Haucke, 2015; Okamoto et al., 2016; Schikorski, 2014; Y. Wu et al., 2014; L. Xue et al., 2012; Zhang, Li, & Tsien, 2009), along with a “reluctant” pool of docked vesicles that may act as an extra reserve pool (J. S. Lee et al., 2012; J. S. Lee et al., 2013; Sakaba, 2006). Reluctant vesicles appear in various synaptic types, including the calyx of Held and hippocampal boutons (Moulder & Mennerick, 2005; Sakaba & Neher, 2001). Although they do not typically release neurotransmitter in response to action potentials, they may be induced to do so by global applications of  $Ca^{2+}$  or hypertonic sucrose (Bacaj et al., 2015; Rosenmund & Stevens, 1996; Sara et al., 2002), which demonstrates that the RRP is much larger than can be estimated through depletion via tetanic stimulation (Moulder & Mennerick, 2005; Neher, 2015). Synapses can actively recruit these vesicles during period of rapid stimulation in a  $Ca^{2+}$ - and actin-dependent manner (J. S. Lee et al., 2012; J. S. Lee et al., 2013). This would provide a way for synapses to maintain a facilitated state during long stimulus trains without depending on vesicle recycling as a rate-limiting step. I expect future implementations of the model presented here to match the data better as they include

more vesicle pools and synaptic processes from the literature. Such models are beyond the scope of this current project, not because the extra features would be difficult to include, but because the parameter values would require a great deal of fine-tuning. The model presented here provides a sufficient proof-of-concept for the utility of  $\text{Ca}^{2+}$ -dependent rates of vesicle recruitment.

### **3.2.2 Runtime Complexity**

A significant advantage of this model is its minimization of computational cost at runtime. As with other event-driven models of physical systems (Ros, Carrillo, Ortigosa, Barbour, & Agís, 2006), jumps directly from one event time to the next, skipping over the intervening periods without having to simulate directly any of the underlying processes. The only processing occurs during the point events, in which the synapse updates its state and uses the new state to calculate the timing of future events. Therefore, the runtime complexity depends most directly on the level of activity driving the synapse model rather than the amount of time being simulated; a long period of low activity may run just as fast as a short period of high activity. For a given synaptic model, the runtime grows linearly with the number of spikes used to stimulate it (Figure 3.11). For low spike rates, there is also a small linear dependence on the simulated time, but this arises from the existence of spontaneous processes. Removing all but the spike-evoked components of synaptic processes eliminates this dependence on time.

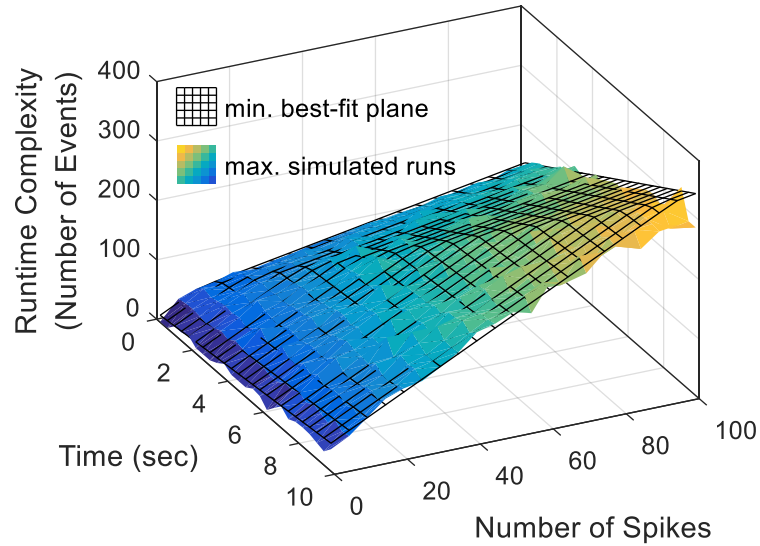


**Figure 3.11: Linear Runtime Complexity of Event-Driven Synaptic Model.**

Surface plot of the number of events simulated for a given number of spikes and length of simulated time. In each trial of a configuration, a fixed number of random spike times, spread uniformly over a fixed length of time, drove the model. Colored surface represents the maximum number of simulated events out of 25 trials in each configuration. Transparent mesh represents best-fit planes to this surface, where two distinct planar regions are visible, and the minimum of the two planes is shown at all points.

In general, as Figure 3.11 demonstrates empirically, the model has a linear runtime complexity of  $O(aS + bT + 1)$ , where  $S$  is the number of spikes,  $T$  is the length of simulated time, and  $a$  and  $b$  are their respective relative contributions to runtime. The value of  $a$  depends on the number and rate of spike-evoked processes;  $a = 0$  in the case where no synaptic processes depend on action potentials or  $\text{Ca}^{2+}$  influx. The value of  $b$  depends on the number and rate of spontaneous processes;  $b = 0$  when no spontaneous vesicle transitions occur and when all events are tightly coupled to the spike times (that is, no event windows longer than a typical ISI). A phase transition in model runtime occurs above a certain rate of stimulation, where the runtime switches

from depending predominantly on the number of spikes ( $a > b$ ) to depending more on the length of time simulated ( $a < b$ ). In this high-spike-rate regime, the runtime actually becomes less than what it would have been if it continued to depend mostly on the number of action potentials. The reason for this reduction is that above a certain rate of stimulation, the release times (and the times of other spike-evoked events) responding to one AP start to overlap with those triggered by the next AP. In other words, the average ISI becomes less than the average time window for spike-evoked activity, reducing the number of events that have time to occur. This phase transition manifests in Figure 3.11` as the function fitting to the minimum of two best-fit planes, where line of intersection of the two planes marks the spike-rate phase-transition boundary. This line of intersection should change depending on the time windows of whatever evoked synaptic processes are present in the model.

Chapter 3, in part, is currently being prepared for submission for publication of the material. Bartol, Thomas M.; Sejnowski, Terrence J. The dissertation author was the primary investigator and author of this material.

## 4 Discussion

Choosing or designing a synaptic model always involves tradeoffs between realism and efficiency. The model presented in this dissertation bridges a gap between existing models on both dimensions. In terms of realism, it includes features such as stochastic, asynchronous release of neurotransmitter from multiple  $\text{Ca}^{2+}$  sensitive mechanisms and demonstrates physiologically crucial features such as facilitation and depression. Furthermore, the explicit nature of vesicle pool exchange provides a highly flexible framework for building models of a diverse array of synapse types and for exploring the effects of synaptic dysfunction on a mechanism-specific level. In terms of efficiency, the event-driven structure allows for maximum scalability for a given level of abstraction of the underlying processes. The structure of the model allows for consolidation of related processes (such as synchronous and asynchronous release mechanisms, or different recycling pathways) into simpler, more abstract representations, although this comes at the cost of making testable predictions with the model.

### 4.1 Model Extensibility

One important feature of the model presented here is its applicability to a diverse array of synapse types. In the central nervous system, some synapses, such as those projecting from pyramidal cells in cortex and interneurons in hippocampus], predominately depress in release probability (Fuhrmann et al., 2004; Rotman et al., 2011; Thomson & Bannister, 1999; Thomson & Deuchars, 1994; M. Tsodyks et al., 1998; M. V. Tsodyks & Markram, 1997). Other synapses, such as those from interneurons in cortex and pyramidal cells in hippocampus, predominantly facilitate (Dobrunz et al., 1997; Dobrunz & Stevens, 1997; Rotman et al., 2011; Thomson &

Bannister, 1999; Thomson & Deuchars, 1994). Some large synapses, such as the calyx of Held in auditory brainstem, contain tens of thousands of vesicles and hundreds of active zone release sites (de Lange et al., 2003; Guo et al., 2015; Qiu, Zhu, & Sun, 2015), while others, such as hippocampal synapses, contain very few vesicles in a small active zone (Denker et al., 2011; Dobrunz & Stevens, 1997; N. Harata et al., 2001; Rosenmund & Stevens, 1996). Recycling pathways for used vesicles also display a huge variety, with many synapses responding to short-term changes in presynaptic activity by adjusting the balance between endocytosis and exocytosis, between kiss-and-run vesicle fusion and full-collapse fusion, or between single-vesicle retrieval and bulk endocytosis (Alabi & Tsien, 2013; Delvendahl et al., 2016; N. C. Harata, Aravanis, & Tsien, 2006; Jockusch, Praefcke, McMahon, & Lagnado, 2005; Park, Li, & Tsien, 2012; Rizzoli & Jahn, 2007; Watanabe et al., 2013; Watanabe et al., 2014; L. G. Wu et al., 2014; Y. Wu et al., 2014; J. Xue et al., 2011; Yamashita et al., 2010; Yue & Xu, 2014; Zhu, Xu, & Heinemann, 2009b). The current model possesses sufficient flexibility to represent any of these features simply by adding or removing vesicle pools and defining the dynamics of the processes whereby vesicles transition between them.

Chapter 3 had the event-driven framework modeling both facilitating hippocampal synapses based on Nadkarni et al. (2010) and Kandaswamy et al. (2010) and depressing cortical synapses based on Fuhrmann et al. (2004) (see Results 3.2.1). The framework easily extends to much larger synapses, such as the calyx of Held, simply by multiplying the number of releasable vesicle pools accordingly. Each releasable pool would have its own associated recycling pathways, feeding either into as many local recycling pools (Fernández-Alfonso & Ryan, 2004; Z. Li et al., 2005) or into a single, much larger recycling pool (Qiu et al., 2015; Staras et al., 2010; X. S. Wu & Wu, 2009). Each releasable pool would represent a single active zone, and runtime would scale

linearly with the number of active zones, since each would generate release times independently. The ability to include an arbitrary number of active zones (with a single shared recycling pool) is already implemented in the code simply by making the primed pool into an array of VesiclePools and using an array of SynProcesses to handle their respective release and redocking dynamics (see Chapter 3 Methods 3.1.3 and [github.com/soiens24/Presynaptic\\_Framework](https://github.com/soiens24/Presynaptic_Framework)).

Any number of recycling pathways are also possible, depending on the rates of each stage of fusion, retrieval, reacidification, and redocking. The way a synapse couples its rate of release/exocytosis with its rate of endocytosis strongly determines the nature of transmission fidelity (Hosoi et al., 2009; L. G. Wu et al., 2014; Xu et al., 2013; Zhu, Xu, & Heinemann, 2009a). Furthermore, this coupling depends on the extent to which the synapse relies on kiss-and-run release and retrieval or on full-collapse fusion and either clathrin mediated or ultrafast bulk endocytosis (Park et al., 2012; Rizzoli & Jahn, 2007; Watanabe et al., 2013; L. G. Wu et al., 2014; Zhang et al., 2009). Each of these processes happens at a different rate in an activity-dependent manner, and each leads to a different time course for reacidification and refill with neurotransmitter (Atluri & Ryan, 2006; X. S. Wu et al., 2009; Y. Wu et al., 2014; J. Xue et al., 2011; Yamashita et al., 2010). The framework presented in this dissertation allows one to explore how different levels of each recycling pathway might contribute to different synaptic adaptations in context of different levels of activity, and each can be made to depend on  $[Ca^{2+}]_i$  (Sakaba & Neher, 2001; X. S. Wu et al., 2014; L. Yao & Sakaba, 2012) by including both spontaneous and spike-evoked components to the vesicle transition rates (see Chapter 3 Methods 3.1.2). Figure 4.1 provides an example of the sort of complexity that this event-driven framework can naturally accommodate.

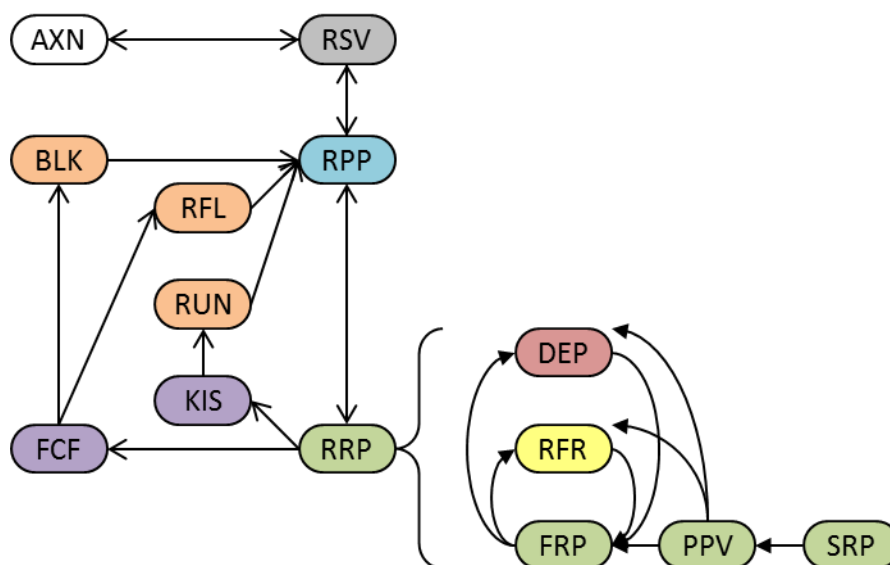


**Figure 4.1: Example of Complex Synapse Made Possible with Event-Driven Framework.**

Colored shapes represent vesicle pools; black arrows represent synaptic processes that move vesicles between pools/states. All pools and pathways based on physiological data. RRP (readily releasable pool) contains releasable vesicles in multiple states (Rosenmund & Stevens, 1996): SRP (slow-releasing pool) holds reluctant vesicles (Moulder & Mennerick, 2005); PPV (positionally-primed vesicles) holds vesicles that have been recruited via actin to sit near  $\text{Ca}^{2+}$  channels during periods of high activity (J. S. Lee et al., 2012); FRP (fast-releasing pool) holds vesicles that have undergone further molecular priming (J. S. Lee et al., 2013); RFR (refractory) represents a post-release refractory period based on local mechanical disturbances in the membrane (Dobrunz et al., 1997); DEP (depressed) represents an inactive state as part of release-independent depression (Fioravante & Regehr, 2011). Any number of RRP's may exist in a model to accommodate synapses of varying sizes. Purple states represent released vesicles that have released neurotransmitter but are still fused, either “kissing” the membrane (KIS; kiss) (Alabi & Tsien, 2013) or fully collapsed (FCF; full-collapse fusion) (Zhang, Cao, & Tsien, 2007). Orange states represent vesicles or membrane that have been retrieved and are being refilled with neurotransmitter (Atluri & Ryan, 2006), either into kiss-and-run vesicles (RUN; run) (Zhang et al., 2009), into clathrin-retrieved large vesicles (RFL; refill) (L. H. Yao et al., 2012), or into bulk endosomes (BLK; bulk) (Delvendahl et al., 2016). RPP (readily priming pool) represents those fully ready vesicles awaiting an open release site in the RRP (Qiu et al., 2015). RSV (reserve) holds vesicles that only slowly get incorporated into the recycling process (Z. Li et al., 2005); and AXN (axon) represents the superpool of vesicles in the axon distributed over numerous synapses (Staras et al., 2010).

## 4.2 Limiting Assumptions of MCell as Ground Truth

A major assumption of the model proposed in this dissertation is that the MCell model of a Schaffer collateral synapse put forth by Nadkarni et al. (2010) can serve as ground truth. However, this assumption is limited on several levels. First, it assumes that MCell can correctly replicate the dynamics of diffusion and molecular interactions of biophysical systems through its Markov chain Monte Carlo framework (Rex A Kerr et al., 2008; Stiles & Bartol, 2001; Stiles et al., 1996). Second, it assumes that the molecular kinetics of the included species match their true kinetics. Finally, it assumes that the molecular species and biological systems modelled are the only ones present in the presynaptic compartment, or at least that any other systems would produce only negligible changes to the phenomenology of the synapse. MCell has been sufficiently well validated to satisfy the first assumption, at least to the temporal and spatial scales of interest here (hundreds of microseconds and hundreds of nanometers).

The second assumption is valid insofar as the molecular models used by MCell correctly represent reality, both in terms of the molecular state diagrams and in terms of the binding and interaction kinetics fitted by other groups: Sun et al. (2007) for the descriptions of  $\text{Ca}^{2+}$ -driven SNARE kinetics for vesicular release; Bischofberger et al. (2002) for the VDCC dynamics for spike-evoked  $\text{Ca}^{2+}$  influx; Nägerl et al. (2000) for the high- and medium-affinity sites of the calbindin  $\text{Ca}^{2+}$  buffer; and Sneyd et al. (2003) for the kinetics of the PMCA pumps. The state diagrams and kinetic parameters for these species are summarized in Figures 2.1, 2.2, 2.4 and Tables 2.1, 2.2 in Chapter 2 Methods 2.1.1. Simplifying assumptions inevitably go into models such as these, which limit the accuracy of any model based on them. However, for the purposes of this dissertation, I assume that these models reproduce experimental results sufficiently to use them.

The greatest limitations to model accuracy come from the third assumption in that the variety of systems and molecular species far exceed what MCell represents (Rizzoli & Tabares, 2016). For instance, the Nadkarni et al. (2010) model did not include any endoplasmic reticulum (ER), which stores of intracellular  $\text{Ca}^{2+}$  and has a significant effect on neuronal signaling (Verkhatsky, 2002). Ryanodine receptors (RyR) (Bouchard, Pattarini, & Geiger, 2003; Lanner, Georgiou, Joshi, & Hamilton, 2010; Otsu et al., 1990) and inositol 1,4,5-trisphosphate receptors (IP3R) (Mikoshiba, 2007; Nixon, Mignery, & Somlyo, 1994) can unleash these  $\text{Ca}^{2+}$  stores. Inclusion of such an ER would likely alter the shape of the  $\text{Ca}^{2+}$  transient and increase the probability of neurotransmitter release, possibly over longer time scales, as in synaptic augmentation (de Juan-Sanz et al., 2017; Kandaswamy et al., 2010). Another system that would significantly affect  $\text{Ca}^{2+}$  dynamics over multiple APs is the inactivation and facilitation of  $\text{Ca}^{2+}$  channels mediated by  $\text{Ca}^{2+}$ -calmodulin (CaM) and  $\text{Ca}^{2+}$  binding proteins (CaBP1) (Ben-Johny & Yue, 2014; Catterall et al., 2013; Hardie & Lee, 2016; A. Lee et al., 2002; Nanou et al., 2016). These interactions might help control release-independent depression (RID) and the frequency-dependent recovery (FDR) from depression (Fuhrmann et al., 2004) by restricting  $\text{Ca}^{2+}$  influx over extended spike trains (see Chapter 3 Results 3.2.1.2). Furthermore, the presynaptic  $\text{Ca}^{2+}$  buffer includes more than just calbindin (Schwaller, 2010; Timofeeva & Volynski, 2015) and diffusion is limited by the plethora of intracellular microstructures (Blum, Lawler, Reed, & Shin, 1989; Novak, Kraikivski, & Slepchenko, 2009). Because location and movement through space plays a crucial role in phenomenology (see Chapter 2 Results 2.2.1, 2.2.4), investigating how these features affect release dynamics would require rerunning the MCell model with them included. Fitting functions to the results, as in Chapter 2, could then allow one to apply these effects to the event-driven model of Chapter 3.

Other considerations of synaptic physiology, those which do not affect the shape of the spike-evoked  $\text{Ca}^{2+}$  transient, would not require rerunning full MCell simulations and include the structure of the SNARE complex. In the MCell model, we assumed that each vesicle employs two  $\text{Ca}^{2+}$  sensors for triggering vesicle fusion, Syt-1/2 for synchronous release and Syt-7 for asynchronous release, as characterized by the Sun et al. (2007) model. Each mechanism acted independently, and together they served as the sole mechanism of release. However, many more molecules comprise the SNARE complex, each affecting release fidelity in complex ways (Imig et al., 2014; J. S. Lee et al., 2013; Südhof, 2004; Südhof, 2013a, 2013b; Südhof & Rothman, 2009; Tang et al., 2006; Varoqueaux et al., 2002). In fact, the inclusion of extra molecules in the SNARE assembly may play a crucial “superpriming” step in enhancing the release alacrity of already-primed vesicles (J. S. Lee et al., 2013; Neher & Sakaba, 2008). Furthermore, although a single SNARE complex is sufficient to induce spike-evoked release (van den Bogaart et al., 2010), each vesicle may have multiple SNARE complexes associated with it, which is necessary for fast vesicle fusion (Mohrmann, de Wit, Verhage, Neher, & Sørensen, 2010). I predict that multiplying SNARE complex would simply multiply release rate in proportion. It is less clear what effects that other molecules, such as complexins and Muncs, would have on release kinetics. A new, validated model of their molecular interaction kinetics is required before they can be applied to this model.

The advantages of using MCell as ground truth, I believe, outweigh the limitations enumerated above. A simulated synaptic model allows for much finer experimental control and consistency from trial to trial, while yielding far more precise results than physiological experiments. Measuring release rate, probability, facilitation, and depression at biological synapses is difficult and requires a number of problematic assumptions (Neher, 2015). Using MCell allows for precise measurements of unmodified

Ca<sup>2+</sup> traces (Bartol et al., 2015) and of single-vesicle release rates, even controlling for such confounding processes as the post-release refractory period (Nadkarni et al., 2010). All things considered, the approach taken in this dissertation made the development of a flexible event-driven framework possible. Any new features, including arbitrary numbers of vesicle pools and synaptic processes, can easily be included in future work (see Section 4.1).

### 4.3 Room for Improvement in Scalability

Although a major part of the purpose of this presynaptic model is to balance realistic phenomenology with computational efficiency, the model presented in this dissertation tends to prioritize the former over the latter. However, there are a number of ways to improve the efficiency significantly. First, and most trivially, the code needs to migrate from a high-level interpreted language (MATLAB; see [github.com/soiens24/Presynaptic\\_Framework](https://github.com/soiens24/Presynaptic_Framework)) to a more machine-level compiled language. Second, although memory necessarily scales linearly with the number of synapses, this increased load can remain insignificant through a shared-memory system. All synapses of the same type could reference the same location in memory for retrieving parameter values, and all synapses of the same axon may share the same states of facilitation, which depends only on spike history (see Chapter 2 Results 2.2.5), without sharing vesicle pool sizes or event times. Both of these changes could reduce processing time and memory requirements without affecting accuracy.

For large-scale simulations that do not require sub-millisecond precision in the timing of events, the temporal filter described in Chapter 2 Results 2.2.3.1 and Chapter 3 Methods 3.1.2.2 may be eliminated. This would, for instance, cause the release response to begin exactly at the spike time or at some fixed delay ( $\mu$ ), while maintaining

most of the realism in the release histogram shape. The number of spike-evoked, exponentially decaying release rate components could also be reduced without much loss in accuracy. Combining synchronous and asynchronous release into one effective mechanism, as done by Nadkarni et al. (2010) when fitting the release histograms, would yield a single triple-exponential shape that fits to within reasonable accuracy over a timescale of a few hundreds of milliseconds (see Figure 3.5B in Chapter 3 Results 3.2.1.1). Longer timescales of release resulting from residual  $\text{Ca}^{2+}$  (see Chapter 2 Results 2.2) may still be included, although their effect on the release histogram is not significantly above spontaneous release rate even for thousands of trials (data not shown). Removing these low-magnitude, long-timescale components may prove not to incur an appreciable cost in accuracy while allowing for a significant speedup in processing time.

Further improvement in efficiency may come by reducing the number of facilitation components used by each component of the spike-evoked processes. Although it is clear that the various time scales of vesicle release, for example, facilitate according to unique functions (see Chapter 2 Results 2.2.5.2), there are possible correlations between components that I did not explore in this dissertation. Future work may elucidate what sorts of reductions and correlations may exist. To simplify the computations required for estimating release rate and facilitation, the model may further use lookup tables for calculating event times based on empirical release-rate histogram profiles. This would allow the model to capture more nuanced dynamics without having to uncover analytical functions to approximate the true histograms or to fit those parameters. It could also allow significant speedup and reduction in memory requirements (Ros et al., 2006), although it may be at the cost of having a system that cannot converge to a smooth histogram over many trials, as the noise of the empirical

lookup table would be preserved. I considered this approach and decided against it in favor of theoretical elegance, but future work may wish to explore incorporating lookup tables into this event-driven framework.

One source of computational load is the post-release refractory period, where all remaining vesicles in the active zone of a release event simultaneously enter a refracted state for 5-8 ms, a form of very-short-term synaptic depression (Dobrunz et al., 1997; Stevens & Wang, 1995). The major cost comes from the fact that each vesicle exits the refracted state individually, as in the MCell implementation (Nadkarni et al., 2010), although it is unclear from experiment whether this is how it happens. To speed this up, one may have all vesicles come out of their refractory period simultaneously. It would preserve the average-case histogram for recovery while significantly speeding up simulations by  $O(N_v)$ , where  $N_v$  is the number of vesicles per active zone. However, it remains unclear how much of an effect this would have on the information transmitted in single trials and whether it would bring the model closer to reality or further away. Other processes, such as bulk endocytosis (Watanabe et al., 2013; J. Xue et al., 2011) and the clathrin-mediated budding of synaptic vesicles from endosomes (Watanabe et al., 2014), could also benefit from having multiple effective vesicles transition between states at once.

A similar gain in efficiency might be possible with a different implementation of release-independent depression and frequency-dependent recovery (RID-FDR). The original model (Fuhrmann et al., 2004) treated recovery from depression as a process with a time constant that changes with time, depending on activity, but this requires simulation of intervening time steps, which can be computationally expensive. The RID-FDR model introduced in this dissertation used competing  $\text{Ca}^{2+}$ -dependent processes to move vesicles between releasable and inactive states (Fioravante & Regehr, 2011) (see

Chapter 3 Results 3.2.1.2). While more efficient for small number of vesicles, such a model becomes impractical for very large releasable pools, and it becomes quite unwieldy when it is taken to occur at individual  $\text{Ca}^{2+}$  channels (Ben-Johny & Yue, 2014; Catterall et al., 2013; Hardie & Lee, 2016; A. Lee et al., 2002; Nanou et al., 2016). A much more efficient model would be to implement RID-FDR with a function that depends only on the value of some variable at the previous spike and on the time interval from then to the current spike, just like the facilitation function explored throughout this dissertation (see Chapter 2 Results 2.2.5 and Chapter 3 Methods 3.1.3.1).

There will always exist trade-offs between accurate representation and efficient computation. The event-driven framework presented in this dissertation allows one to explore these trade-offs on a spectrum, from molecular-level, sub-millisecond representation to a highly abstract level that operates over much longer timescales. It allows for easy inclusion and exclusion of both dynamic features and levels of detailed complexity.

## **4.4 Comparisons to Other Models**

Over the years, many synaptic models have been explored and used in various applications. Many neural networks used both for theoretical research in neuroscience and for practical applications in machine learning and artificial intelligence use “synapses” that act as simple multiplicative weights (Chapeau-Blondeau & Chambet, 1995; Dayhoff & DeLeo, 2001; Maass & Zador, 1999; Schmidhuber, 2015). While such abstractions have enabled a great deal of progress in areas such as deep learning for image recognition and natural language processing, they bear only distant resemblance to real synapses. As such, they are not amenable to studying the effects of synaptic function or dysfunction in brain circuits. The model presented in this dissertation

overcomes this limitation by enabling a scalable representation of many different synaptic features in a way that bridges the gap between concrete physiology and abstract phenomenology.

It is unfortunately impossible to make an exact quantitative comparison between the different models below because they each produce different types of outputs, whether actual release event times (my model), instantaneous synaptic current (M. V. Tsodyks & Markram, 1997), Boolean release events (Maass & Zador, 1999), or spike-evoked release probabilities (Kandaswamy et al., 2010). Fortunately, each of these generates the same downstream effect on the postsynaptic neuron, namely an excitatory post-synaptic potential (EPSP, assuming excitatory synapses). The associated excitatory postsynaptic current (EPSC) results from the opening of AMPA receptors at the postsynaptic density upon the release of neurotransmitter, and the magnitude is proportional to the fraction of activated synaptic resources (M. V. Tsodyks & Markram, 1997) or to the probability of spike-evoked release (Kandaswamy et al., 2010; Maass & Zador, 1999). The resulting current,  $I_{syn}(t)$ , jumps in response to a release event (or probabilistically in response to an AP) and decays exponentially with a time constant of 1-3 ms as activated AMPARs close (M. V. Tsodyks & Markram, 1997). It drives the EPSP ( $V$ ) according to

$$\tau_{mem} \frac{dV}{dt} = -V + R_{in} I_{syn}(t), \quad (4.1)$$

where  $\tau_{mem} = 50$  ms is the membrane time constant and  $R_{in} = 100$  M $\Omega$  is the input (synaptic) resistance (M. Tsodyks et al., 1998). However, because synaptic conductance is incidental to the concern for short-term presynaptic plasticity, I treated the resulting EPSP magnitudes as arbitrary, although it typically fell in the range of a couple millivolts.

#### 4.4.1 Tsodyks and Markram (1997)

One popular synaptic model that represents a wide range of synapse types through its elegant implementation of short-term plasticity is the model designed by Tsodyks and Markram (1997). It uses a relatively simple representation of the utilization of synaptic resources, tracking the fraction of resources in recovered, active, and inactivated states, to flexibly model both short-term depression and facilitation (M. Tsodyks et al., 1998). It has already proven useful in simulated neural network contexts for producing complex behavior (Cortes et al., 2013).

The Tsodyks-Markram (TM) model does all this deterministically, representing average or aggregate synaptic behavior rather than single-trial behavior. However, the presence of trial-to-trial stochasticity in synaptic transmission may have important implications for the learning and information processing performed in neural circuits (Buesing, Bill, Nessler, & Maass, 2011; Faber, Young, Legendre, & Korn, 1992; Faisal, Selen, & Wolpert, 2008; Otmakhov, Shirke, & Malinow, 1993; Seung, 2003). Although the TM model captures a wide variety of synaptic dynamics, including facilitation and depression of transmission strength, its deterministic formulation fails to capture this trial-to-trial variability. Furthermore, it lacks the predictive inherent to my model since it abstracts away all the internal processes of the synapse, even conflating presynaptic (vesicle availability, release probability) with postsynaptic (neurotransmitter receptor saturation) resources. As seen in Figure 4.2 below, both my event-driven framework and the TM model are able to represent a wide variety of synapse types, both predominantly facilitating (red) and predominantly depressing (blue), through changes to parameter values.

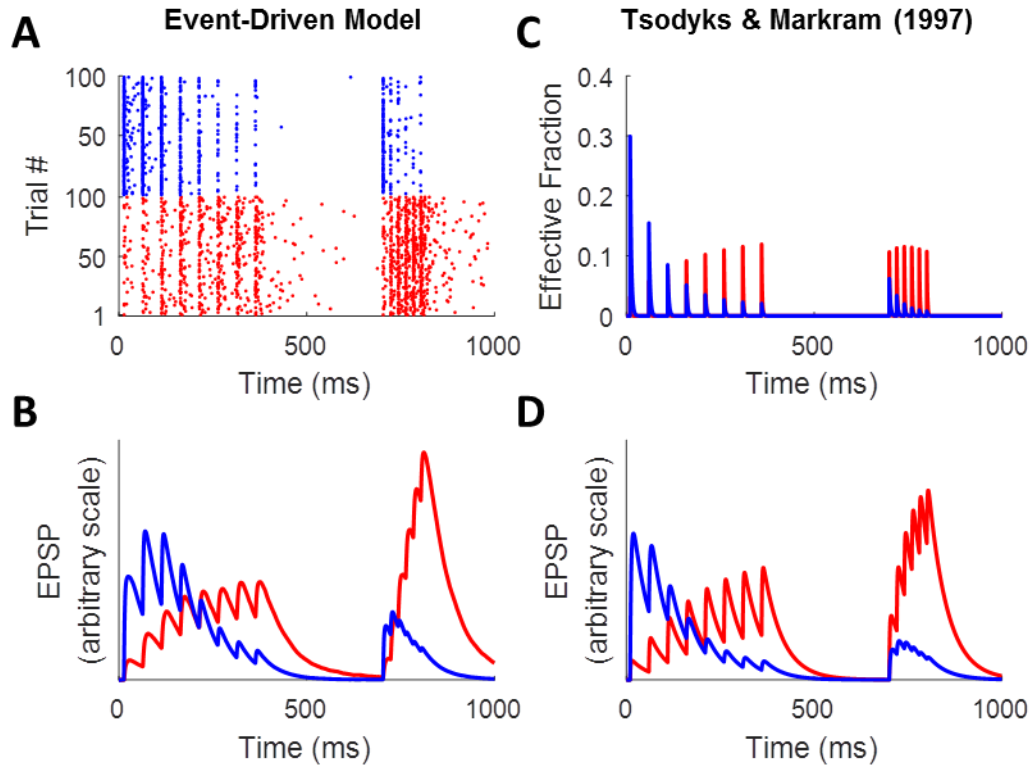


**Figure 4.2: Comparison of My Model with That of Tsodyks and Markram (1997).**

In both models, blue represents the output of a model with depressing parameter values, and red represents output with facilitating values. Eight spikes delivered at 20 Hz followed by six spikes delivered at 50 Hz. (A) Release event raster for 100 trials of each event-driven model. (B) EPSPs generated from the respective release time histograms of the event-driven models. (C) Fraction of synaptic resources in use for transmission over time for the TM model. (D) EPSPs generated from TM model.

The TM model succeeds in the simplicity of its representation of different synapse types. It can serve well for high-level models that care more about aggregate changes in short-term synaptic transmission than the contributions of individual synapses (Cortes et al., 2013). My model has the advantage of capturing trial-to-trial variability, asynchronicity, and internal synaptic dynamics, which the TM model fails to represent. It works best for simulations that aim to uncover the contributions of single synapses or synaptic features to network computations.

#### 4.4.2 Maass and Zador (1999)

An example of a presynaptic model that captures probabilistic release is that by Maass and Zador (1999). The Maass-Zador (MZ) model tracks short-term facilitation in response to spike history and short-term depression in response to release history, calculating the probability of release in response to each spike as a function of the facilitation and depression functions at each spike time and generating Boolean release events according to this probability. As such, it captures stochasticity and trial-to-trial variability of real synapses. However, it still fails to account for spontaneous or asynchronous release of neurotransmitter since releases in the MZ model can only occur exactly at spike times. Furthermore, a series of mathematical quirks in the model cause depression to over-exert itself (specifically, pulling the depression function below zero), forcing an extended quiescent period and limiting the number of release events for a given spike train over many trials. When stimulated at high frequency, the MZ model generates releases in waves of alternating quiescence and recovery (data not shown). These oscillations do not arise from physiological data but rather as a mathematical artifact of the model.

A further limitation is the lack of explanatory power as to the synaptic origins of short-term plasticity. The phenomenology of the MZ model, while elegant, arises from mathematical abstractions rather than from physiologically grounded mechanisms, making it susceptible to produce unrealistic behavior as described above and limiting its utility as a testable model. Once again, the advantage of my event-driven framework is its balance of efficiency with physiologically grounded realism. It further includes both asynchronous and spontaneous release events, which the MZ model lacks (see Figure 4.3). Both models can have their parameters adjusted to alter the balance between short-term facilitation and depression, but only my model bridges the gap between

molecular mechanisms and phenomenology. For neural network simulations where the presence of stochasticity in synaptic transmission is more important than reproducing true dynamics, the MZ model may suffice. Of course, it surpasses my model in terms of computational scalability, both in memory load and in number of computations. However, for investigations into how presynaptic mechanisms of vesicle release and recycling affect information transmission and network behavior, my model provides an indispensable layer of flexibility.

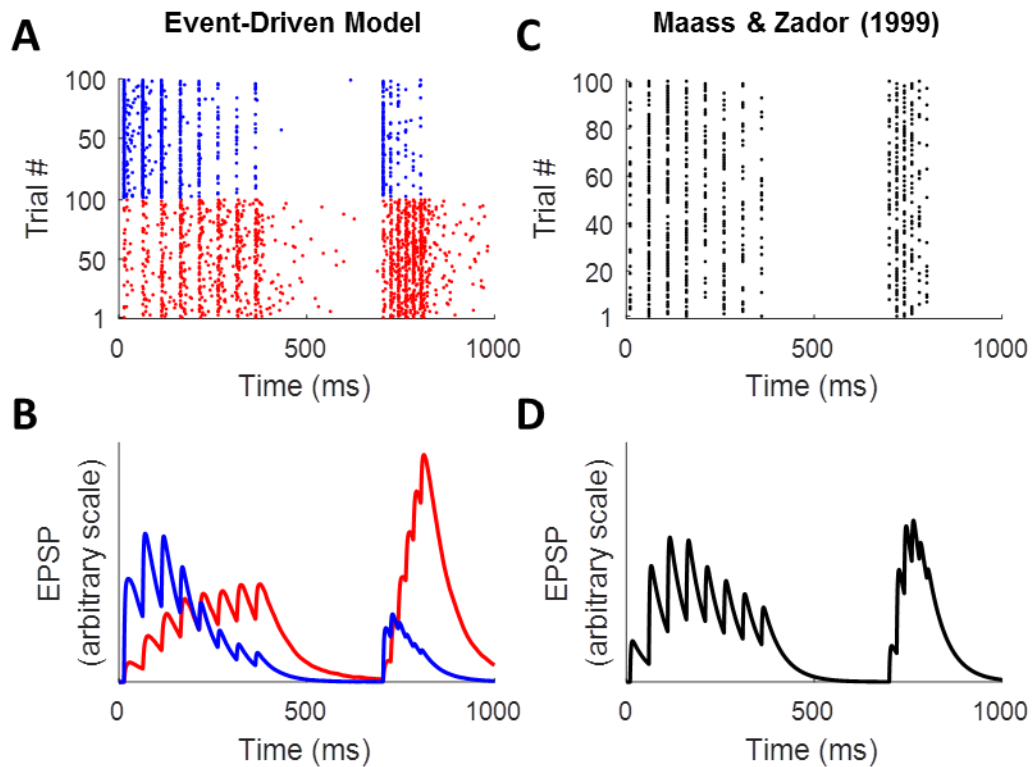


**Figure 4.3: Comparison of My Model with That of Maass and Zador (1999).**

Same spike train as in Figure 4.2. (A) Same as Figure 4.2A. (B) Same as Figure 4.2B. (C) Release raster of the MZ model with release events occurring probabilistically at spike times. (D) EPSP generated from MZ model.

### 4.4.3 Kandaswamy et al. (2010)

Although the Kandaswamy et al. (KK) model (2010) does match the experimental data well, it lacks generalizability. In particular, the free parameters of their model, which they adjusted to fit the experimental data, depend empirically on the frequency of stimulation but without any discernible pattern that would provide insight into their origin (see Table 2 in (Kandaswamy et al., 2010)). Additionally, the exponential decay model for the REC pool assumes a constant rate of stimulation, and their  $\xi$  parameter, introduced to prevent overfilling of the RRP, relies on the assumption that a minimum time interval has passed between action potentials (data not shown). Finally, and crucially, the model for facilitation treats the first spike as a special case relative to all subsequent spikes. As seen in Figure 4.4C, the facilitation from the first to the second spike of the first AP train is much larger than for the second AP train beginning at 700 ms. A realistic short-term facilitation model should scale the probability of release on the first spike as though it occurred in the middle of a train after an infinite ISI, as the synapse should return to its baseline state after a sufficiently long interval of no spiking activity, all else being equal. However, the KK model instead arbitrarily excludes the first spike from facilitation to fit the data. Thus, it lacks the generalizability to appropriately accommodate spike trains with arbitrarily large inter-spike intervals.

The model I developed in this dissertation overcomes these limitations by providing a highly flexible and explanatory framework. Each of the parameters for describing the profile of the release histogram ( $P$ ,  $\tau$ ,  $k$ ,  $\mu$ ,  $\sigma$ ; see Equations 2.17-2.26 in Chapter 2 Results 2.2.3) has an almost direct link to the underlying physiology, whether to the  $\text{Ca}^{2+}$ -binding and vesicle fusion kinetics of the SNARE complex ( $P$  and  $\tau$ ) or to the stochastic delay in response to the AP caused by buffered diffusion of  $\text{Ca}^{2+}$  ( $k$ ,  $\mu$ , and  $\sigma$ ). Furthermore, the facilitation function has sufficient complexity to account for the changes

seen in neurotransmitter release fidelity of a wide variety of spike train patterns. Importantly, all spikes are treated equally: Equations 2.27-2.32 (in Chapter 2 Results 2.2.5) apply as consistently to the first spike as to the  $n$ -th. While it falls short in terms of computational efficiency relative to the Kandaswamy et al. model, it makes up for it in terms of biophysical plausibility and its utility for testing hypotheses regarding synaptic function.

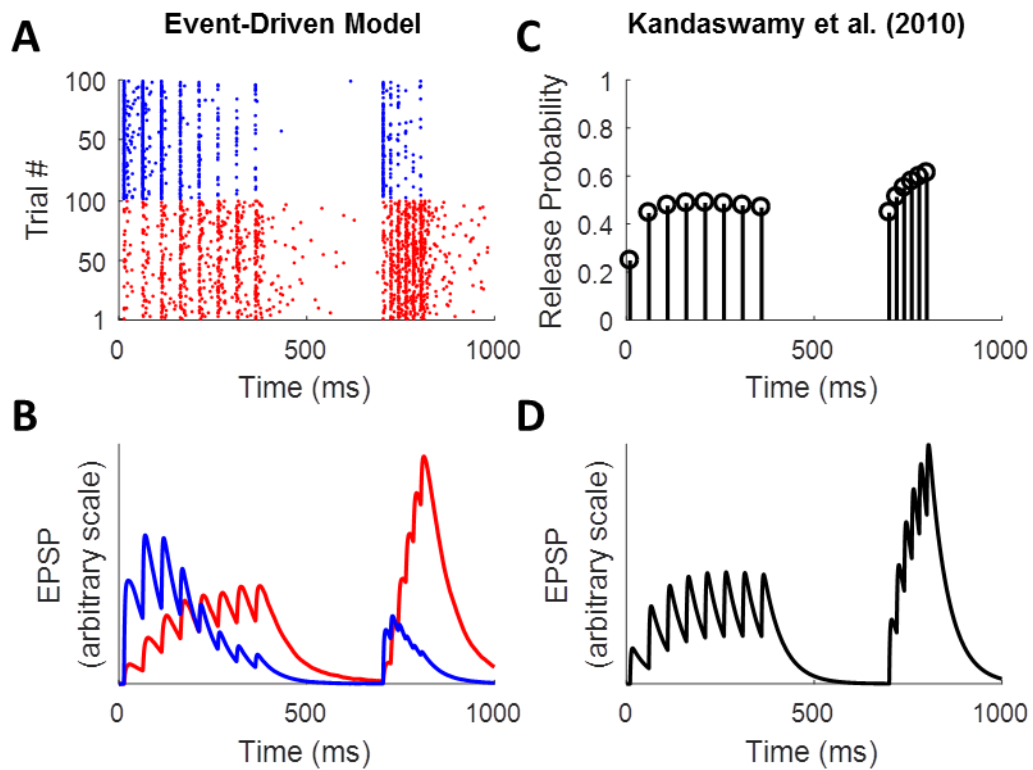


**Figure 4.4: Comparison of My Model with That of Kandaswamy et al. (2010).**

Same spike train as in Figure 4.2. (A) Same as Figure 4.2A. (B) Same as Figure 4.2B. (C) Probability of neurotransmitter release in response to each spike for the KK model. (D) EPSP generated from KK model.

## 4.5 Summary and Further Applications

The event-driven model that I introduce in this dissertation provides a framework for making testable predictions and performing controlled experiments of synaptic function in a manner that balances the realism, versatility, and scalability required for large-scale simulations of synaptic information processing. The MCell model of Schaffer collateral synapses off of which much of this work was based (Nadkarni et al., 2010) must keep track of dozens of parameters and thousands of molecular positions, trajectories, and reactions at high spatial and temporal resolution. Such a high computational overhead can reproduce highly detailed phenomenology and generate testable predictions (Bartol et al., 2015; R. A. Kerr et al., 2008; Stiles & Bartol, 2001; Stiles et al., 1996), assuming the validity of chosen parameter values and molecular state diagrams (Bischofberger et al., 2002; Nägerl et al., 2000; Simons, 1988; Sneyd et al., 2003; J. Sun et al., 2007), but at the cost of speed and computer memory. Other synaptic models, reviewed in the previous section, operate at high speed and with low memory requirements, but at the cost of realism and predictive power, either because they are too mathematically abstract (Maass & Zador, 1999) or because they represent only the aggregate behavior of many synapses (Kandaswamy et al., 2010; M. V. Tsodyks & Markram, 1997). My event-driven framework bridges the gap between these molecular and aggregate models. Its predictive power arises from explicit vesicle pool dynamics and from the extreme versatility of its spike-evoked,  $\text{Ca}^{2+}$ -dependent processes. It can represent synapses of arbitrary size and complexity (see Section 4.1) while minimizing simulation time between successive events.

To study the roles of short-term facilitation, depression, and recovery at synapses relative to information transfer, researchers may use computational models rather than experimental investigations because of the difficulty in the latter (Scott et al.,

2012). The event-driven presynaptic framework presented in this dissertation is ideal for this purpose, not only because it produces arbitrarily realistic dynamics, but also because it can elucidate the link between the molecular and information-processing scales. Specifically, the flexibility of the model can uncover the roles that each presynaptic biochemical process plays in transforming the spiking code into the synapse-specific release code by allowing investigators to perform the necessary controlled experiments without requiring the manipulation of living tissue.

Much debate has gone on about whether neurons use predominantly a spike-timing code or a spike-rate code (O'Keefe & Burgess, 2005; Van Rullen, Guyonneau, & Thorpe, 2005; Van Rullen & Thorpe, 2001), but the answer could simply be that it depends on what the neuron is trying to represent in context of its position in the perception-action cycle in the brain (Prescott & Sejnowski, 2008; Tateno & Robinson, 2006). Facilitating synapses, such as those from hippocampal pyramidal cells (Kandaswamy et al., 2010; O'Keefe & Burgess, 2005), exhibit high-pass filtering. Due to their low baseline probability of release, they ignore lone spikes and instead respond selectively to bursts of action potentials, which might imply that such synapses wait until their source neuron has accumulated enough evidence to be adamantly certain of its associated belief state before it conveys this information to the next neuron. Depressing synapses, on the other hand, such as layer 5 and 6 cortical pyramidal cells (Fuhrmann et al., 2004; Thomson & Bannister, 1999; Thomson & Deuchars, 1994), acts as low-pass filters. With high initial release probabilities, they respond to isolated spikes while ignoring extended high-activity trains, which might imply a preference for conveying information about the timing of stimulus onset (Rotman et al., 2011).

My model can reproduce a wide variety of synaptic dynamics, essential for representing the diversity of computations performed in the various circuits throughout

the brain. Simply changing a handful of parameters can transform the synapse from predominantly facilitating to predominantly depressing, for instance. Crucially, it can reveal how each of the various internal presynaptic processes that couple exocytosis and endocytosis control the resonance of the synapse's release code with the neuron's spike code (C. C. Lee et al., 2009; L. G. Wu et al., 2014; Zhu et al., 2009a). Furthermore, the same flexibility of the model that allows one to explore each mechanism's role in information processing by turning features on and off can enable future investigators to explore how disease states in synaptic function may induce disease states at the level of network behavior. Scientists studying the role of synaptic dysfunction in behavioral or mental disorders (Crabtree & Gogos, 2014; Deng et al., 2011; Giovedi et al., 2014; Vawter et al., 2002) may manipulate relevant recycling pathways, time constants, or  $\text{Ca}^{2+}$  dependencies in the model to help pinpoint not only which molecular mechanisms might contribute most to the disease state but also which pharmacological interventions might produce the greatest benefit. For such purposes, my model could help save considerable time and cost of research by providing the necessary flexibility for performing such controlled experiments. In summary, I have presented in this dissertation a tool for computational neuroscientists to explore how low-level presynaptic dynamics effect large-scale neural computations. By explicitly tracking vesicle pools and state transitions and their spontaneous and  $\text{Ca}^{2+}$ -dependent rates in a flexible manner and by representing dynamics in an event-driven fashion, the model balances physiological realism with both representational versatility and computational scalability.

## REFERENCES

- Abbott, L. F., & Regehr, W. G. (2004). Synaptic computation. *Nature*, *431*(7010), 796-803.
- Acuna, C., Guo, Q., Burré, J., Sharma, M., Sun, J., & Südhof, T. C. (2014). Microsecond dissection of neurotransmitter release: SNARE-complex assembly dictates speed and Ca<sup>2+</sup> sensitivity. *Neuron*, *82*(5), 1088-1100. doi:10.1016/j.neuron.2014.04.020
- Alabi, A. A., & Tsien, R. W. (2012). Synaptic vesicle pools and dynamics. *Cold Spring Harb Perspect Biol*, *4*(8), a013680.
- Alabi, A. A., & Tsien, R. W. (2013). Perspectives on kiss-and-run: role in exocytosis, endocytosis, and neurotransmission. *Annu Rev Physiol*, *75*, 393-422.
- Atluri, P. P., & Ryan, T. A. (2006). The kinetics of synaptic vesicle reacidification at hippocampal nerve terminals. *J Neurosci*, *26*(8), 2313-2320.
- Bacaj, T., Wu, D., Burré, J., Malenka, R. C., Liu, X., & Südhof, T. C. (2015). Synaptotagmin-1 and -7 Are Redundantly Essential for Maintaining the Capacity of the Readily-Releasable Pool of Synaptic Vesicles. *PLoS Biol*, *13*(10), e1002267.
- Bacaj, T., Wu, D., Yang, X., Morishita, W., Zhou, P., Xu, W., . . . Südhof, T. C. (2013). Synaptotagmin-1 and synaptotagmin-7 trigger synchronous and asynchronous phases of neurotransmitter release. *Neuron*, *80*(4), 947-959.
- Bartol, T. M., Keller, D. X., Kinney, J. P., Bajaj, C. L., Harris, K. M., Sejnowski, T. J., & Kennedy, M. B. (2015). Computational reconstitution of spine calcium transients from individual proteins. *Front Synaptic Neurosci*, *7*, 17.
- Ben-Johny, M., & Yue, D. T. (2014). Calmodulin regulation (calmodulation) of voltage-gated calcium channels. *J Gen Physiol*, *143*(6), 679-692.
- Bischofberger, J., Geiger, J. R., & Jonas, P. (2002). Timing and efficacy of Ca<sup>2+</sup> channel activation in hippocampal mossy fiber boutons. *J Neurosci*, *22*(24), 10593-10602.
- Blum, J. J., Lawler, G., Reed, M., & Shin, I. (1989). Effect of cytoskeletal geometry on intracellular diffusion. *Biophys J*, *56*(5), 995-1005. doi:10.1016/S0006-3495(89)82744-4
- Bouchard, R., Pattarini, R., & Geiger, J. D. (2003). Presence and functional significance of presynaptic ryanodine receptors. *Prog Neurobiol*, *69*(6), 391-418.
- Branco, T., & Staras, K. (2009). The probability of neurotransmitter release: variability and feedback control at single synapses. *Nat Rev Neurosci*, *10*(5), 373-383.
- Brody, D. L., & Yue, D. T. (2000). Release-independent short-term synaptic depression in cultured hippocampal neurons. *J Neurosci*, *20*(7), 2480-2494.
- Buesing, L., Bill, J., Nessler, B., & Maass, W. (2011). Neural dynamics as sampling: a model for stochastic computation in recurrent networks of spiking neurons. *PLoS Comput Biol*, *7*(11), e1002211. doi:10.1371/journal.pcbi.1002211

- Buzsáki, G., Anastassiou, C. A., & Koch, C. (2012). The origin of extracellular fields and currents—EEG, ECoG, LFP and spikes. *Nat Rev Neurosci*, *13*(6), 407-420. doi:10.1038/nrn3241
- Catterall, W. A., Leal, K., & Nanou, E. (2013). Calcium channels and short-term plasticity. *J Biol Chem*, *288*(15), 10742-10749.
- Chapeau-Blondeau, F., & Chambet, N. (1995). Synapse models for neural networks: from ion channel kinetics to multiplicative coefficient  $w_{ij}$ . *Neural Comput*, *7*(4), 713-734.
- Collinger, J. L., Wodlinger, B., Downey, J. E., Wang, W., Tyler-Kabara, E. C., Weber, D. J., . . . Schwartz, A. B. (2013). High-performance neuroprosthetic control by an individual with tetraplegia. *Lancet*, *381*(9866), 557-564. doi:10.1016/S0140-6736(12)61816-9
- Cooper, J. C. (2005). The Poisson and Exponential Distributions. *Mathematical Spectrum*, *37*(3), 123-125.
- Cortes, J. M., Desroches, M., Rodrigues, S., Veltz, R., Muñoz, M. A., & Sejnowski, T. J. (2013). Short-term synaptic plasticity in the deterministic Tsodyks-Markram model leads to unpredictable network dynamics. *Proc Natl Acad Sci U S A*, *110*(41), 16610-16615.
- Crabtree, G. W., & Gogos, J. A. (2014). Synaptic plasticity, neural circuits, and the emerging role of altered short-term information processing in schizophrenia. *Front Synaptic Neurosci*, *6*, 28.
- DasGupta, A. (2010). Normal Approximations and the Central Limit Theorem. In *Fundamentals of Probability: A First Course* (pp. 213-242): Springer.
- Dayhoff, J. E., & DeLeo, J. M. (2001). Artificial neural networks. *Cancer*, *91*(8), 1615-1635. doi:10.1002/1097-0142(20010415)91:8+<1615::AID-CNCR1175>3.0.CO;2-L
- de Juan-Sanz, J., Holt, G. T., Schreiter, E. R., de Juan, F., Kim, D. S., & Ryan, T. A. (2017). Axonal Endoplasmic Reticulum Ca(2+) Content Controls Release Probability in CNS Nerve Terminals. *Neuron*, *93*(4), 867-881.e866. doi:10.1016/j.neuron.2017.01.010
- de Lange, R. P., de Roos, A. D., & Borst, J. G. (2003). Two modes of vesicle recycling in the rat calyx of Held. *J Neurosci*, *23*(31), 10164-10173.
- Delvendahl, I., Jablonski, L., Baade, C., Matveev, V., Neher, E., & Hallermann, S. (2015). Reduced endogenous Ca<sup>2+</sup> buffering speeds active zone Ca<sup>2+</sup> signaling. *Proc Natl Acad Sci U S A*, *112*(23), E3075-3084.
- Delvendahl, I., Vyleta, N. P., von Gersdorff, H., & Hallerman, S. (2016). Fast, Temperature-Sensitive and Clathrin-Independent Endocytosis at Central Synapses. *Neuron*, *90*(3), 492-498.
- Deng, P. Y., Soika, D., & Klyachko, V. A. (2011). Abnormal presynaptic short-term plasticity and information processing in a mouse model of fragile X syndrome. *J Neurosci*, *31*(30), 10971-10982.

- Denker, A., Bethani, I., Kröhnert, K., Körber, C., Horstmann, H., Wilhelm, B. G., . . . Rizzoli, S. O. (2011). A small pool of vesicles maintains synaptic activity *in vivo*. *Proc Natl Acad Sci U S A*, *108*(41), 17177-17182.
- Dobrunz, L. E., Huang, E. P., & Stevens, C. F. (1997). Very short-term plasticity in hippocampal synapses. *Proc Natl Acad Sci U S A*, *94*(26), 14843-14847.
- Dobrunz, L. E., & Stevens, C. F. (1997). Heterogeneity of release probability, facilitation, and depletion at central synapses. *Neuron*, *18*(6), 995-1008.
- Edwards, R. H. (2007). The neurotransmitter cycle and quantal size. *Neuron*, *55*(6), 835-858.
- Ertunc, M., Sara, Y., Chung, C., Atasoy, D., Virmani, T., & Kavalali, E. T. (2007). Fast synaptic vesicle reuse slows the rate of synaptic depression in the CA1 region of hippocampus. *J Neurosci*, *27*(2), 341-354.
- Faber, D. S., Young, W. S., Legendre, P., & Korn, H. (1992). Intrinsic quantal variability due to stochastic properties of receptor-transmitter interactions. *Science*, *258*(5087), 1494-1498.
- Faisal, A. A., Selen, L. P., & Wolpert, D. M. (2008). Noise in the nervous system. *Nat Rev Neurosci*, *9*(4), 292-303. doi:10.1038/nrn2258
- Fernandez, I., Araç, D., Ubach, J., Gerber, S. H., Shin, O., Gao, Y., . . . Rizo, J. (2001). Three-dimensional structure of the synaptotagmin 1 C2B-domain: synaptotagmin 1 as a phospholipid binding machine. *Neuron*, *32*(6), 1057-1069.
- Fernández-Alfonso, T., & Ryan, T. A. (2004). The kinetics of synaptic vesicle pool depletion at CNS synaptic terminals. *Neuron*, *41*(6), 943-953.
- Fioravante, D., & Regehr, W. G. (2011). Short-term forms of presynaptic plasticity. *Curr Opin Neurobiol*, *21*(2), 269-274.
- Franks, K. M., & Sejnowski, T. J. (2002). Complexity of calcium signaling in synaptic spines. *Bioessays*, *24*(12), 1130-1144. doi:10.1002/bies.10193
- Franks, K. M., Stevens, C. F., & Sejnowski, T. J. (2003). Independent sources of quantal variability at single glutamatergic synapses. *J Neurosci*, *23*(8), 3186-3195.
- Fuhrmann, G., Cowan, A., Segev, I., Tsodyks, M., & Stricker, C. (2004). Multiple mechanisms govern the dynamics of depression at neocortical synapses of young rats. *J Physiol*, *557*(2), 415-438.
- Gandhi, S. P., & Stevens, C. F. (2003). Three modes of synaptic vesicular recycling revealed by single-vesicle imaging. *Nature*, *423*(6940), 607-613.
- Giovedi, S., Corradi, A., Fassio, A., & Benfenati, F. (2014). Involvement of synaptic genes in the pathogenesis of autism spectrum disorders: the case of synapsins. *Front Pediatr*, *2*, 94.
- Grewe, B. F., & Helmchen, F. (2014). High-speed two-photon calcium imaging of neuronal population activity using acousto-optic deflectors. *Cold Spring Harb Protoc*, *2014*(6), 618-629. doi:10.1101/pdb.prot081778

- Grienberger, C., & Konnerth, A. (2012). Imaging calcium in neurons. *Neuron*, *73*(5), 862-885. doi:10.1016/j.neuron.2012.02.011
- Gross, O. P., & von Gersdorff, H. (2016). Recycling at synapses. *eLife*, *5*, e17692.
- Guo, J., Ge, J. L., Hao, M., Sun, Z. C., Wu, X. S., Zhu, J. B., . . . Xue, L. (2015). A three-pool model dissecting readily releasable pool replenishment at the calyx of held. *Sci Rep*, *5*, 9517.
- Hahnloser, R. H., Kozhevnikov, A. A., & Fee, M. S. (2002). An ultra-sparse code underlies the generation of neural sequences in a songbird. *Nature*, *419*(6902), 65-70. doi:10.1038/nature00974
- Hallermann, S., & Silver, R. A. (2013). Sustaining rapid vesicular release at active zones: potential roles for vesicle tethering. *Trends Neurosci*, *36*(3), 185-194. doi:10.1016/j.tins.2012.10.001
- Harata, N., Pyle, J. L., Aravanis, A. M., Mozhayeva, M., Kavalali, E. T., & Tsien, R. W. (2001). Limited numbers of recycling vesicles in small CNS nerve terminals: implications for neural signaling and vesicular cycling. *Trends Neurosci*, *24*(11), 637-643.
- Harata, N. C., Aravanis, A. M., & Tsien, R. W. (2006). Kiss-and-run and full-collapse fusion as modes of exo-endocytosis in neurosecretion. *J Neurochem*, *97*(6), 1546-1570.
- Hardie, J., & Lee, A. (2016). Decalmodulation of Cav1 channels by CaBPs. *Channels (Austin)*, *10*(1), 33-37. doi:10.1080/19336950.2015.1051273
- Hochberg, L. R., Serruya, M. D., Friebs, G. M., Mukand, J. A., Saleh, M., Caplan, A. H., . . . Donoghue, J. P. (2006). Neuronal ensemble control of prosthetic devices by a human with tetraplegia. *Nature*, *442*(7099), 164-171. doi:10.1038/nature04970
- Hosoi, N., Holt, M., & Sakaba, T. (2009). Calcium dependence of exo- and endocytotic coupling at a glutamatergic synapse. *Neuron*, *63*(2), 216-229.
- Hosoi, N., Sakaba, T., & Neher, E. (2007). Quantitative analysis of calcium-dependent vesicle recruitment and its functional role at the calyx of Held synapse. *J Neurosci*, *27*(52), 14286-14298.
- Imig, C., Min, S.-W., Krinner, S., Arancillo, M., Rosenmund, C., Südhof, T. C., . . . Cooper, B. H. (2014). The Morphological and Molecular Nature of Synaptic Vesicle Priming at Presynaptic Active Zones. *Neuron*, *84*, 416-431. doi:10.1016/j.neuron.2014.10.009
- Jockusch, W. J., Praefcke, G. J., McMahon, H. T., & Lagnado, L. (2005). Clathrin-dependent and clathrin-independent retrieval of synaptic vesicles in retinal bipolar cells. *Neuron*, *46*(6), 869-878. doi:10.1016/j.neuron.2005.05.004
- Kaesler, P. S., & Regehr, W. G. (2014). Molecular mechanisms for synchronous, asynchronous, and spontaneous neurotransmitter release. *Annu Rev Physiol*, *76*, 333-363. doi:10.1146/annurev-physiol-021113-170338

- Kandaswamy, U., Deng, P. Y., Stevens, C. F., & Klyachko, V. A. (2010). The role of presynaptic dynamics in processing of natural spike trains in hippocampal synapses. *J Neurosci*, *30*(47), 15904-15914. doi:10.1523/JNEUROSCI.4050-10.2010
- Kato, K., Sekino, Y., Takahashi, H., Yasuda, H., & Shirao, T. (2007). Increase in AMPA receptor-mediated miniature EPSC amplitude after chronic NMDA receptor blockade in cultured hippocampal neurons. *Neurosci Lett*, *418*(1), 4-8. doi:10.1016/j.neulet.2007.02.058
- Kerr, R. A., Bartol, T. M., Kaminsky, B., Dittrich, M., Chang, J.-C. J., Baden, S. B., . . . Stiles, J. R. (2008). FAST MONTE CARLO SIMULATION METHODS FOR BIOLOGICAL REACTION-DIFFUSION SYSTEMS IN SOLUTION AND ON SURFACES. *SIAM J Sci Comput*, *30*(6), 3126.
- Kerr, R. A., Bartol, T. M., Kaminsky, B., Dittrich, M., Chang, J. C., Baden, S. B., . . . Stiles, J. R. (2008). FAST MONTE CARLO SIMULATION METHODS FOR BIOLOGICAL REACTION-DIFFUSION SYSTEMS IN SOLUTION AND ON SURFACES. *SIAM J Sci Comput*, *30*(6), 3126. doi:10.1137/070692017
- Kitamura, K., Judkewitz, B., Kano, M., Denk, W., & Häusser, M. (2008). Targeted patch-clamp recordings and single-cell electroporation of unlabeled neurons in vivo. *Nat Methods*, *5*(1), 61-67. doi:10.1038/nmeth1150
- Klaes, C., Shi, Y., Kellis, S., Minxha, J., Revechki, B., & Andersen, R. A. (2014). A cognitive neuroprosthetic that uses cortical stimulation for somatosensory feedback. *J Neural Eng*, *11*(5), 056024. doi:10.1088/1741-2560/11/5/056024
- Knöpfel, T. (2012). Genetically encoded optical indicators for the analysis of neuronal circuits. *Nat Rev Neurosci*, *13*(10), 687-700. doi:10.1038/nrn3293
- Kochubey, O., Lou, X., & Schneggenburger, R. (2011). Regulation of transmitter release by Ca(2+) and synaptotagmin: insights from a large CNS synapse. *Trends Neurosci*, *34*(5), 237-246. doi:10.1016/j.tins.2011.02.006
- Kononenko, N. L., & Haucke, V. (2015). Molecular mechanisms of presynaptic membrane retrieval and synaptic vesicle reformation. *Neuron*, *85*(3), 484-496. doi:10.1016/j.neuron.2014.12.016
- Körber, C., & Künér, T. (2016). Molecular Machines Regulating the Release Probability of Synaptic Vesicles at the Active Zone. *Front Synaptic Neurosci*, *8*, 5. doi:10.3389/fnsyn.2016.00005
- Lanner, J. T., Georgiou, D. K., Joshi, A. D., & Hamilton, S. L. (2010). Ryanodine receptors: structure, expression, molecular details, and function in calcium release. *Cold Spring Harb Perspect Biol*, *2*(11), a003996. doi:10.1101/cshperspect.a003996
- Lee, A., Westenbroek, R. E., Haeseleer, F., Palczewski, K., Scheuer, T., & Catterall, W. A. (2002). Differential modulation of Ca(v)2.1 channels by calmodulin and Ca2+-binding protein 1. *Nat Neurosci*, *5*(3), 210-217. doi:10.1038/nn805

- Lee, C. C., Anton, M., Poon, C. S., & McRae, G. J. (2009). A kinetic model unifying presynaptic short-term facilitation and depression. *J Comput Neurosci*, 26(3), 459-473. doi:10.1007/s10827-008-0122-6
- Lee, J. S., Ho, W. K., & Lee, S. H. (2012). Actin-dependent rapid recruitment of reluctant synaptic vesicles into a fast-releasing vesicle pool. *Proc Natl Acad Sci U S A*, 109(13), E765-774. doi:10.1073/pnas.1114072109
- Lee, J. S., Ho, W. K., Neher, E., & Lee, S. H. (2013). Superpriming of synaptic vesicles after their recruitment to the readily releasable pool. *Proc Natl Acad Sci U S A*, 110(37), 15079-15084. doi:10.1073/pnas.1314427110
- Li, F., Kümmel, D., Coleman, J., Reinisch, K. M., Rothman, J. E., & Pincet, F. (2014). A half-zipped SNARE complex represents a functional intermediate in membrane fusion. *J Am Chem Soc*, 136(9), 3456-3464. doi:10.1021/ja410690m
- Li, F., Pincet, F., Perez, E., Eng, W. S., Melia, T. J., Rothman, J. E., & Tareste, D. (2007). Energetics and dynamics of SNAREpin folding across lipid bilayers. *Nat Struct Mol Biol*, 14(10), 890-896. doi:10.1038/nsmb1310
- Li, Z., Burrone, J., Tyler, W. J., Hartman, K. N., Albeanu, D. F., & Murthy, V. N. (2005). Synaptic vesicle recycling studied in transgenic mice expressing synaptophluorin. *Proc Natl Acad Sci U S A*, 102(17), 6131-6136. doi:10.1073/pnas.0501145102
- Luo, F., Bacaj, T., & Südhof, T. C. (2015). Synaptotagmin-7 Is Essential for Ca<sup>2+</sup>-Triggered Delayed Asynchronous Release But Not for Ca<sup>2+</sup>-Dependent Vesicle Priming in Retinal Ribbon Synapses. *J Neurosci*, 35(31), 11024-11033. doi:10.1523/JNEUROSCI.0759-15.2015
- Maass, W., & Zador, A. M. (1999). Dynamic stochastic synapses as computational units. *Neural Comput*, 11(4), 903-917.
- Malgaroli, A., & Tsien, R. W. (1992). Glutamate-induced long-term potentiation of the frequency of miniature synaptic currents in cultured hippocampal neurons. *Nature*, 357(6374), 134-139. doi:10.1038/357134a0
- Maximov, A., Lao, Y., Li, H., Chen, X., Rizo, J., Sørensen, J. B., & Südhof, T. C. (2008). Genetic analysis of synaptotagmin-7 function in synaptic vesicle exocytosis. *Proc Natl Acad Sci U S A*, 105(10), 3986-3991. doi:10.1073/pnas.0712372105
- McKinnon, K. I. M. (1998). Convergence of the Nelder--Mead Simplex Method to a Nonstationary Point. *SIAM J. Optim.*, 9(1), 148-158. doi:10.1137/S1052623496303482
- Mikoshiba, K. (2007). The IP<sub>3</sub> receptor/Ca<sup>2+</sup> channel and its cellular function. *Biochem Soc Symp*(74), 9-22. doi:10.1042/BSS0740009
- Mohrmann, R., de Wit, H., Verhage, M., Neher, E., & Sørensen, J. B. (2010). Fast vesicle fusion in living cells requires at least three SNARE complexes. *Science*, 330(6003), 502-505. doi:10.1126/science.1193134

- Morrison, A., Straube, S., Plesser, H. E., & Diesmann, M. (2007). Exact subthreshold integration with continuous spike times in discrete-time neural network simulations. *Neural Comput*, 19(1), 47-79. doi:10.1162/neco.2007.19.1.47
- Moulder, K. L., & Mennerick, S. (2005). Reluctant vesicles contribute to the total readily releasable pool in glutamatergic hippocampal neurons. *J Neurosci*, 25(15), 3842-3850. doi:10.1523/JNEUROSCI.5231-04.2005
- Murthy, V. N., Schikorski, T., Stevens, C. F., & Zhu, Y. (2001). Inactivity produces increases in neurotransmitter release and synapse size. *Neuron*, 32(4), 673-682.
- Murthy, V. N., & Stevens, C. F. (1999). Reversal of synaptic vesicle docking at central synapses. *Nat Neurosci*, 2(6), 503-507. doi:10.1038/9149
- Nadkarni, S., Bartol, T. M., Sejnowski, T. J., & Levine, H. (2010). Modelling vesicular release at hippocampal synapses. *PLoS Comput Biol*, 6(11), e1000983. doi:10.1371/journal.pcbi.1000983
- Nanou, E., Sullivan, J. M., Scheuer, T., & Catterall, W. A. (2016). Calcium sensor regulation of the CaV2.1 Ca<sup>2+</sup> channel contributes to short-term synaptic plasticity in hippocampal neurons. *Proc Natl Acad Sci U S A*, 113(4), 1062-1067. doi:10.1073/pnas.1524636113
- Neher, E. (2010). What is Rate-Limiting during Sustained Synaptic Activity: Vesicle Supply or the Availability of Release Sites. *Front Synaptic Neurosci*, 2, 144. doi:10.3389/fnsyn.2010.00144
- Neher, E. (2015). Merits and Limitations of Vesicle Pool Models in View of Heterogeneous Populations of Synaptic Vesicles. *Neuron*, 87(6), 1131-1142. doi:10.1016/j.neuron.2015.08.038
- Neher, E., & Sakaba, T. (2008). Multiple roles of calcium ions in the regulation of neurotransmitter release. *Neuron*, 59(6), 861-872. doi:10.1016/j.neuron.2008.08.019
- Nelder, J. A., & Mead, R. (1965). A Simplex Method for Function Minimization. *Comput J*, 7(4), 308-313. doi:10.1093/comjnl/7.4.308
- Nixon, G. F., Mignery, G. A., & Somlyo, A. V. (1994). Immunogold localization of inositol 1,4,5-trisphosphate receptors and characterization of ultrastructural features of the sarcoplasmic reticulum in phasic and tonic smooth muscle. *J Muscle Res Cell Motil*, 15(6), 682-700.
- Novak, I. L., Kraikivski, P., & Slepchenko, B. M. (2009). Diffusion in cytoplasm: effects of excluded volume due to internal membranes and cytoskeletal structures. *Biophys J*, 97(3), 758-767. doi:10.1016/j.bpj.2009.05.036
- Nägerl, U. V., Novo, D., Mody, I., & Vergara, J. L. (2000). Binding kinetics of calbindin-D(28k) determined by flash photolysis of caged Ca(2+). *Biophys J*, 79(6), 3009-3018. doi:10.1016/S0006-3495(00)76537-4

- O'Keefe, J., & Burgess, N. (2005). Dual phase and rate coding in hippocampal place cells: theoretical significance and relationship to entorhinal grid cells. *Hippocampus*, *15*(7), 853-866. doi:10.1002/hipo.20115
- Okamoto, Y., Lipstein, N., Hua, Y., Lin, K. H., Brose, N., Sakaba, T., & Midorikawa, M. (2016). Distinct modes of endocytotic presynaptic membrane and protein uptake at the calyx of Held terminal of rats and mice. *Elife*, *5*. doi:10.7554/eLife.14643
- Otmakhov, N., Shirke, A. M., & Malinow, R. (1993). Measuring the impact of probabilistic transmission on neuronal output. *Neuron*, *10*(6), 1101-1111.
- Otsu, K., Willard, H. F., Khanna, V. K., Zorzato, F., Green, N. M., & MacLennan, D. H. (1990). Molecular cloning of cDNA encoding the Ca<sup>2+</sup> release channel (ryanodine receptor) of rabbit cardiac muscle sarcoplasmic reticulum. *J Biol Chem*, *265*(23), 13472-13483.
- Pabst, S., Margittai, M., Vainius, D., Langen, R., Jahn, R., & Fasshauer, D. (2002). Rapid and selective binding to the synaptic SNARE complex suggests a modulatory role of complexins in neuroexocytosis. *J Biol Chem*, *277*(10), 7838-7848. doi:10.1074/jbc.M109507200
- Park, H., Li, Y., & Tsien, R. W. (2012). Influence of synaptic vesicle position on release probability and exocytotic fusion mode. *Science*, *335*(6074), 1362-1366. doi:10.1126/science.1216937
- Pobbati, A. V., Stein, A., & Fasshauer, D. (2006). N- to C-terminal SNARE complex assembly promotes rapid membrane fusion. *Science*, *313*(5787), 673-676. doi:10.1126/science.1129486
- Prescott, S. A., & Sejnowski, T. J. (2008). Spike-rate coding and spike-time coding are affected oppositely by different adaptation mechanisms. *J Neurosci*, *28*(50), 13649-13661. doi:10.1523/JNEUROSCI.1792-08.2008
- Qiu, X., Zhu, Q., & Sun, J. (2015). Quantitative analysis of vesicle recycling at the calyx of Held synapse. *Proc Natl Acad Sci U S A*, *112*(15), 4779-4784. doi:10.1073/pnas.1424597112
- Renden, R., & von Gersdorff, H. (2007). Synaptic vesicle endocytosis at a CNS nerve terminal: faster kinetics at physiological temperatures and increased endocytotic capacity during maturation. *J Neurophysiol*, *98*(6), 3349-3359. doi:10.1152/jn.00898.2007
- Rizzoli, S. O., & Jahn, R. (2007). Kiss-and-run, collapse and 'readily retrievable' vesicles. *Traffic*, *8*(9), 1137-1144. doi:10.1111/j.1600-0854.2007.00614.x
- Rizzoli, S. O., & Tabares, L. (2016). Editorial: Molecular Nanomachines of the Presynaptic Terminal. *Front Synaptic Neurosci*, *8*, 27. doi:10.3389/fnsyn.2016.00027
- Ros, E., Carrillo, R., Ortigosa, E. M., Barbour, B., & Agís, R. (2006). Event-driven simulation scheme for spiking neural networks using lookup tables to characterize neuronal dynamics. *Neural Comput*, *18*(12), 2959-2993. doi:10.1162/neco.2006.18.12.2959

- Rosahl, T. W., Geppert, M., Spillane, D., Herz, J., Hammer, R. E., Malenka, R. C., & Südhof, T. C. (1993). Short-term synaptic plasticity is altered in mice lacking synapsin I. *Cell*, *75*(4), 661-670.
- Rosenbaum, R., Rubin, J., & Doiron, B. (2012). Short term synaptic depression imposes a frequency dependent filter on synaptic information transfer. *PLoS Comput Biol*, *8*(6), e1002557. doi:10.1371/journal.pcbi.1002557
- Rosenmund, C., & Stevens, C. F. (1996). Definition of the readily releasable pool of vesicles at hippocampal synapses. *Neuron*, *16*(6), 1197-1207.
- Rotman, Z., Deng, P. Y., & Klyachko, V. A. (2011). Short-term plasticity optimizes synaptic information transmission. *J Neurosci*, *31*(41), 14800-14809. doi:10.1523/JNEUROSCI.3231-11.2011
- Sabatini, B. L., & Regehr, W. G. (1996). Timing of neurotransmission at fast synapses in the mammalian brain. *Nature*, *384*(6605), 170-172. doi:10.1038/384170a0
- Sakaba, T. (2006). Roles of the fast-releasing and the slowly releasing vesicles in synaptic transmission at the calyx of Held. *J Neurosci*, *26*(22), 5863-5871. doi:10.1523/JNEUROSCI.0182-06.2006
- Sakaba, T., & Neher, E. (2001). Calmodulin mediates rapid recruitment of fast-releasing synaptic vesicles at a calyx-type synapse. *Neuron*, *32*(6), 1119-1131.
- Salmasi, M., Stemmler, M., Glasauer, S., & Loebel, A. (2017). Information Rate Analysis of a Synaptic Release Site Using a Two-State Model of Short-Term Depression. *Neural Comput*, *29*(6), 1528-1560. doi:10.1162/NECO\_a\_00962
- Sara, Y., Mozhayeva, M. G., Liu, X., & Kavalali, E. T. (2002). Fast vesicle recycling supports neurotransmission during sustained stimulation at hippocampal synapses. *J Neurosci*, *22*(5), 1608-1617.
- Scanziani, M., & Häusser, M. (2009). Electrophysiology in the age of light. *Nature*, *461*(7266), 930-939. doi:10.1038/nature08540
- Schiavo, G., Stenbeck, G., Rothman, J. E., & Söllner, T. H. (1997). Binding of the synaptic vesicle v-SNARE, synaptotagmin, to the plasma membrane t-SNARE, SNAP-25, can explain docked vesicles at neurotoxin-treated synapses. *Proc Natl Acad Sci U S A*, *94*(3), 997-1001.
- Schikorski, T. (2014). Readily releasable vesicles recycle at the active zone of hippocampal synapses. *Proc Natl Acad Sci U S A*, *111*(14), 5415-5420. doi:10.1073/pnas.1321541111
- Schmidhuber, J. (2015). Deep learning in neural networks: an overview. *Neural Netw*, *61*, 85-117. doi:10.1016/j.neunet.2014.09.003
- Schneggenburger, R., & Neher, E. (2000). Intracellular calcium dependence of transmitter release rates at a fast central synapse. *Nature*, *406*(6798), 889-893. doi:10.1038/35022702

- Schonn, J. S., Maximov, A., Lao, Y., Südhof, T. C., & Sørensen, J. B. (2008). Synaptotagmin-1 and -7 are functionally overlapping Ca<sup>2+</sup> sensors for exocytosis in adrenal chromaffin cells. *Proc Natl Acad Sci U S A*, *105*(10), 3998-4003. doi:10.1073/pnas.0712373105
- Schwaller, B. (2010). Cytosolic Ca<sup>2+</sup> buffers. *Cold Spring Harb Perspect Biol*, *2*(11), a004051. doi:10.1101/cshperspect.a004051
- Scott, P., Cowan, A. I., & Stricker, C. (2012). Quantifying impacts of short-term plasticity on neuronal information transfer. *Phys Rev E Stat Nonlin Soft Matter Phys*, *85*(4 Pt 1), 041921. doi:10.1103/PhysRevE.85.041921
- Seung, H. S. (2003). Learning in spiking neural networks by reinforcement of stochastic synaptic transmission. *Neuron*, *40*(6), 1063-1073.
- Shew, W. L., Bellay, T., & Plenz, D. (2010). Simultaneous multi-electrode array recording and two-photon calcium imaging of neural activity. *J Neurosci Methods*, *192*(1), 75-82. doi:10.1016/j.jneumeth.2010.07.023
- Simons, T. J. (1988). Calcium and neuronal function. *Neurosurg Rev*, *11*(2), 119-129.
- Sneyd, J., Tsaneva-Atanasova, K., Bruce, J. I., Straub, S. V., Giovannucci, D. R., & Yule, D. I. (2003). A model of calcium waves in pancreatic and parotid acinar cells. *Biophys J*, *85*(3), 1392-1405. doi:10.1016/S0006-3495(03)74572-X
- Spira, M. E., & Hai, A. (2013). Multi-electrode array technologies for neuroscience and cardiology. *Nat Nanotechnol*, *8*(2), 83-94. doi:10.1038/nnano.2012.265
- Staras, K., Branco, T., Burden, J. J., Pozo, K., Darcy, K., Marra, V., . . . Goda, Y. (2010). A vesicle superpool spans multiple presynaptic terminals in hippocampal neurons. *Neuron*, *66*(1), 37-44. doi:10.1016/j.neuron.2010.03.020
- Stevens, C. F., & Wang, Y. (1995). Facilitation and depression at single central synapses. *Neuron*, *14*(4), 795-802.
- Stiles, J. R., & Bartol, T. M. (2001). Monte Carlo methods for simulating realistic synaptic microphysiology using MCell. In E. De Schutter (Ed.), *Computational Neuroscience: Realistic Modeling for Experimentalists* (pp. 87-127). Boca Raton: CRC Press.
- Stiles, J. R., van Helden, D., Bartol, T. M., Salpeter, E. E., & Salpeter, M. M. (1996). Miniature endplate current rise times <100 ms from improved dual recordings can be modeled with passive acetylcholine diffusion from a synaptic vesicle. *Proc Natl Acad Sci U S A*, *93*, 5747-5752.
- Südhof, T. C. (2004). The synaptic vesicle cycle. *Annu Rev Neurosci*, *27*, 509-547. doi:10.1146/annurev.neuro.26.041002.131412
- Sugita, S., Han, W., Butz, S., Liu, X., Fernández-Chacón, R., Lao, Y., & Südhof, T. C. (2001). Synaptotagmin VII as a plasma membrane Ca(2+) sensor in exocytosis. *Neuron*, *30*(2), 459-473.

- Sun, J., Pang, Z. P., Qin, D., Fahim, A. T., Adachi, R., & Südhof, T. C. (2007). A dual-Ca<sup>2+</sup>-sensor model for neurotransmitter release in a central synapse. *Nature*, *450*(7170), 676-682. doi:10.1038/nature06308
- Sun, J. Y., & Wu, L. G. (2001). Fast kinetics of exocytosis revealed by simultaneous measurements of presynaptic capacitance and postsynaptic currents at a central synapse. *Neuron*, *30*(1), 171-182.
- Sutton, R. B., Fasshauer, D., Jahn, R., & Brunger, A. T. (1998). Crystal structure of a SNARE complex involved in synaptic exocytosis at 2.4 Å resolution. *Nature*, *395*(6700), 347-353. doi:10.1038/26412
- Südhof, T. C. (2013a). A molecular machine for neurotransmitter release: synaptotagmin and beyond. *Nat Med*, *19*(10), 1227-1231. doi:10.1038/nm.3338
- Südhof, T. C. (2013b). Neurotransmitter release: the last millisecond in the life of a synaptic vesicle. *Neuron*, *80*(3), 675-690. doi:10.1016/j.neuron.2013.10.022
- Südhof, T. C., & Rothman, J. E. (2009). Membrane fusion: grappling with SNARE and SM proteins. *Science*, *323*(5913), 474-477. doi:10.1126/science.1161748
- Tang, J., Maximov, A., Shin, O. H., Dai, H., Rizo, J., & Südhof, T. C. (2006). A complexin/synaptotagmin 1 switch controls fast synaptic vesicle exocytosis. *Cell*, *126*(6), 1175-1187. doi:10.1016/j.cell.2006.08.030
- Tateno, T., & Robinson, H. P. (2006). Rate coding and spike-time variability in cortical neurons with two types of threshold dynamics. *J Neurophysiol*, *95*(4), 2650-2663. doi:10.1152/jn.00683.2005
- Thomson, A. M., & Bannister, A. P. (1999). Release-independent depression at pyramidal inputs onto specific cell targets: dual recordings in slices of rat cortex. *J Physiol*, *519 Pt 1*, 57-70.
- Thomson, A. M., & Deuchars, J. (1994). Temporal and spatial properties of local circuits in neocortex. *Trends Neurosci*, *17*(3), 119-126.
- Timofeeva, Y., & Volynski, K. E. (2015). Calmodulin as a major calcium buffer shaping vesicular release and short-term synaptic plasticity: facilitation through buffer dislocation. *Front Cell Neurosci*, *9*, 239. doi:10.3389/fncel.2015.00239
- Tsodyks, M., Pawelzik, K., & Markram, H. (1998). Neural networks with dynamic synapses. *Neural Comput*, *10*(4), 821-835.
- Tsodyks, M. V., & Markram, H. (1997). The neural code between neocortical pyramidal neurons depends on neurotransmitter release probability. *Proc Natl Acad Sci U S A*, *94*(2), 719-723.
- Ubach, J., Lao, Y., Fernandez, I., Arac, D., Südhof, T. C., & Rizo, J. (2001). The C2B domain of synaptotagmin I is a Ca<sup>2+</sup>-binding module. *Biochemistry*, *40*(20), 5854-5860.

- Ubach, J., Zhang, X., Shao, X., Südhof, T. C., & Rizo, J. (1998). Ca<sup>2+</sup> binding to synaptotagmin: how many Ca<sup>2+</sup> ions bind to the tip of a C2-domain? *EMBO J*, *17*(14), 3921-3930. doi:10.1093/emboj/17.14.3921
- van den Bogaart, G., Holt, M. G., Bunt, G., Riedel, D., Wouters, F. S., & Jahn, R. (2010). One SNARE complex is sufficient for membrane fusion. *Nat Struct Mol Biol*, *17*(3), 358-364. doi:10.1038/nsmb.1748
- Van Rullen, R., Guyonneau, R., & Thorpe, S. J. (2005). Spike times make sense. *Trends Neurosci*, *28*(1), 1-4. doi:10.1016/j.tins.2004.10.010
- Van Rullen, R., & Thorpe, S. J. (2001). Rate coding versus temporal order coding: what the retinal ganglion cells tell the visual cortex. *Neural Comput*, *13*(6), 1255-1283.
- Varela, J. A., Sen, K., Gibson, J., Fost, J., Abbott, L. F., & Nelson, S. B. (1997). A quantitative description of short-term plasticity at excitatory synapses in layer 2/3 of rat primary visual cortex. *J Neurosci*, *17*(20), 7926-7940.
- Varoqueaux, F., Sigler, A., Rhee, J. S., Brose, N., Enk, C., Reim, K., & Rosenmund, C. (2002). Total arrest of spontaneous and evoked synaptic transmission but normal synaptogenesis in the absence of Munc13-mediated vesicle priming. *Proc Natl Acad Sci U S A*, *99*(13), 9037-9042. doi:10.1073/pnas.122623799
- Vawter, M. P., Thatcher, L., Usen, N., Hyde, T. M., Kleinman, J. E., & Freed, W. J. (2002). Reduction of synapsin in the hippocampus of patients with bipolar disorder and schizophrenia. *Mol Psychiatry*, *7*(6), 571-578. doi:10.1038/sj.mp.4001158
- Veletić, M., Floor, P. A., Chahibi, Y., & Balasingham, I. (2016). On the Upper Bound of the Information Capacity in Neuronal Synapses. *IEEE Transactions on Communications*, *64*(12), 5205-5036. doi:10.1109/TCOMM.2016.2613970
- Verkhatsky, A. (2002). The endoplasmic reticulum and neuronal calcium signalling. *Cell Calcium*, *32*(5-6), 393-404.
- Wadel, K., Neher, E., & Sakaba, T. (2007). The coupling between synaptic vesicles and Ca<sup>2+</sup> channels determines fast neurotransmitter release. *Neuron*, *53*(4), 563-575. doi:10.1016/j.neuron.2007.01.021
- Warren, C. S., Mackay, D., Webster, E., & Arnot, J. A. (2009). A cautionary note on implications of the well-mixed compartment assumption as applied to mass balance models of chemical fate in flowing systems. *Environ Toxicol Chem*, *28*(9), 1858-1865. doi:10.1897/08-569.1
- Watanabe, S., Rost, B. R., Camacho-Pérez, M., Davis, M. W., Söhl-Kielczynski, B., Rosenmund, C., & Jorgensen, E. M. (2013). Ultrafast endocytosis at mouse hippocampal synapses. *Nature*, *504*(7479), 242-247. doi:10.1038/nature12809
- Watanabe, S., Trimbuch, T., Camacho-Pérez, M., Rost, B. R., Brokowski, B., Söhl-Kielczynski, B., . . . Jorgensen, E. M. (2014). Clathrin regenerates synaptic vesicles from endosomes. *Nature*, *515*(7526), 228-233. doi:10.1038/nature13846

- Wu, L. G., Hamid, E., Shin, W., & Chiang, H. C. (2014). Exocytosis and endocytosis: modes, functions, and coupling mechanisms. *Annu Rev Physiol*, 76, 301-331. doi:10.1146/annurev-physiol-021113-170305
- Wu, X. S., McNeil, B. D., Xu, J., Fan, J., Xue, L., Melicoff, E., . . . Wu, L. G. (2009). Ca<sup>2+</sup> and calmodulin initiate all forms of endocytosis during depolarization at a nerve terminal. *Nat Neurosci*, 12(8), 1003-1010. doi:10.1038/nn.2355
- Wu, X. S., & Wu, L. G. (2009). Rapid endocytosis does not recycle vesicles within the readily releasable pool. *J Neurosci*, 29(35), 11038-11042. doi:10.1523/JNEUROSCI.2367-09.2009
- Wu, X. S., Zhang, Z., Zhao, W. D., Wang, D., Luo, F., & Wu, L. G. (2014). Calcineurin is universally involved in vesicle endocytosis at neuronal and nonneuronal secretory cells. *Cell Rep*, 7(4), 982-988. doi:10.1016/j.celrep.2014.04.020
- Wu, Y., O'Toole, E. T., Girard, M., Ritter, B., Messa, M., Liu, X., . . . De Camilli, P. (2014). A dynamin 1-, dynamin 3- and clathrin-independent pathway of synaptic vesicle recycling mediated by bulk endocytosis. *Elife*, 3, e01621. doi:10.7554/eLife.01621
- Wölfel, M., Lou, X., & Schneggenburger, R. (2007). A mechanism intrinsic to the vesicle fusion machinery determines fast and slow transmitter release at a large CNS synapse. *J Neurosci*, 27(12), 3198-3210. doi:10.1523/JNEUROSCI.4471-06.2007
- Xu, J., Luo, F., Zhang, Z., Xue, L., Wu, X. S., Chiang, H. C., . . . Wu, L. G. (2013). SNARE proteins synaptobrevin, SNAP-25, and syntaxin are involved in rapid and slow endocytosis at synapses. *Cell Rep*, 3(5), 1414-1421. doi:10.1016/j.celrep.2013.03.010
- Xu, J., Pang, Z. P., Shin, O. H., & Südhof, T. C. (2009). Synaptotagmin-1 functions as a Ca<sup>2+</sup> sensor for spontaneous release. *Nat Neurosci*, 12(6), 759-766. doi:10.1038/nn.2320
- Xue, J., Graham, M. E., Novelle, A. E., Sue, N., Gray, N., McNiven, M. A., . . . Robinson, P. J. (2011). Calcineurin selectively docks with the dynamin lxb splice variant to regulate activity-dependent bulk endocytosis. *J Biol Chem*, 286(35), 30295-30303. doi:10.1074/jbc.M111.273110
- Xue, L., McNeil, B. D., Wu, X. S., Luo, F., He, L., & Wu, L. G. (2012). A membrane pool retrieved via endocytosis overshoot at nerve terminals: a study of its retrieval mechanism and role. *J Neurosci*, 32(10), 3398-3404. doi:10.1523/JNEUROSCI.5943-11.2012
- Yamashita, T., Eguchi, K., Saitoh, N., von Gersdorff, H., & Takahashi, T. (2010). Developmental shift to a mechanism of synaptic vesicle endocytosis requiring nanodomain Ca<sup>2+</sup>. *Nat Neurosci*, 13(7), 838-844. doi:10.1038/nn.2576
- Yang, Y., & Calakos, N. (2013). Presynaptic long-term plasticity. *Front Synaptic Neurosci*, 5, 8. doi:10.3389/fnsyn.2013.00008
- Yao, L., & Sakaba, T. (2012). Activity-dependent modulation of endocytosis by calmodulin at a large central synapse. *Proc Natl Acad Sci U S A*, 109(1), 291-296. doi:10.1073/pnas.1100608109

- Yao, L. H., Rao, Y., Varga, K., Wang, C. Y., Xiao, P., Lindau, M., & Gong, L. W. (2012). Synaptotagmin 1 is necessary for the Ca<sup>2+</sup> dependence of clathrin-mediated endocytosis. *J Neurosci*, *32*(11), 3778-3785. doi:10.1523/JNEUROSCI.3540-11.2012
- Yue, H. Y., & Xu, J. (2014). Myosin light chain kinase accelerates vesicle endocytosis at the calyx of Held synapse. *J Neurosci*, *34*(1), 295-304. doi:10.1523/JNEUROSCI.3744-13.2014
- Zhang, Q., Cao, Y. Q., & Tsien, R. W. (2007). Quantum dots provide an optical signal specific to full collapse fusion of synaptic vesicles. *Proc Natl Acad Sci U S A*, *104*(45), 17843-17848. doi:10.1073/pnas.0706906104
- Zhang, Q., Li, Y., & Tsien, R. W. (2009). The dynamic control of kiss-and-run and vesicular reuse probed with single nanoparticles. *Science*, *323*(5920), 1448-1453. doi:10.1126/science.1167373
- Zhu, Y., & Stevens, C. F. (2008). Probing synaptic vesicle fusion by altering mechanical properties of the neuronal surface membrane. *Proc Natl Acad Sci U S A*, *105*(46), 18018-18022. doi:10.1073/pnas.0809714105
- Zhu, Y., Xu, J., & Heinemann, S. F. (2009a). Synaptic vesicle exocytosis-endocytosis at central synapses: Fine-tuning at differential patterns of neuronal activity. *Commun Integr Biol*, *2*(5), 418-419.
- Zhu, Y., Xu, J., & Heinemann, S. F. (2009b). Two pathways of synaptic vesicle retrieval revealed by single-vesicle imaging. *Neuron*, *61*(3), 397-411. doi:10.1016/j.neuron.2008.12.024
- Zucker, R. S., & Regehr, W. G. (2002). Short-term synaptic plasticity. *Annu Rev Physiol*, *64*, 355-405. doi:10.1146/annurev.physiol.64.092501.114547